



UNIVERSITY OF BERGEN

**Textural and geochemical characteristics of hematitic
chert deposits in SW Norway:
Implications for formation settings and processes**

Submitted by

HENRIKE WILBORN

To the

CENTRE FOR GEOBIOLOGY,
DEPARTMENT OF EARTH SCIENCES,
FACULTY OF MATHEMATICS AND NATURAL SCIENCES

In partial fulfilment of the requirements
for achieving the Degree of

MASTER OF SCIENCE IN EARTH SCIENCE

With a specialisation in
GEOCHEMISTRY AND GEOBIOLOGY

NOVEMBER 2017

Bergen, Norway

Supervisor:

INGUNN HINDENES THORSETH

Department of Earth Science

University of Bergen, Norway

Co-Supervisor:

ROLF BIRGER PEDERSEN

Department of Earth Science

University of Bergen, Norway

Abstract

Jasper, a specific type of hematitic chert, is often interpreted as an ancient analogue to modern seafloor hydrothermal deposits. Modern low-temperature seafloor hydrothermal Fe-deposits are mainly produced by Fe(II)-oxidising chemolithoautotrophs, which produce characteristic filamentous microstructures. Hematitic cherts from the SW Norwegian ophiolitic terrain exposed on the islands Stord and Bømlo have not been examined within the scope of this potential formation process. In this study, 10 hematitic chert samples were investigated to clarify the processes leading to their formation and if they all formed analogously to modern seafloor hydrothermal Fe-deposits. Additionally it was examined how the presence of hematitic cherts within the ophiolitic terrain can help to improve the understanding of the areas' geological history. Geochemical, textural, and mineralogical analyses were conducted by applying inductively coupled plasma optical emission spectrometry, inductively coupled plasma mass spectrometry, optical microscopy, scanning electron microscopy, and Raman spectroscopy. Pronounced geochemical and textural differences were found, and four subtypes of hematitic chert were defined. Bedded hematitic radiolarian cherts (Lower/Middle Ordovician, Langevåg on Bømlo and Sagvåg on Stord) consist of SiO_2 ($\sim 77 - 87 \text{ wt}\%$), Al_2O_3 ($\sim 6 - 10 \text{ wt}\%$), and Fe_2O_3 ($\sim 3 - 6 \text{ wt}\%$), and they have relatively high trace and rare earth element (REE) concentrations ($\sum\text{REE} \sim 30 - 66 \text{ ppm}$). Radiolarian shell remnants and distinct

layering are present. A sampled hematitic radiolarian chert band (late Cambrian, Geitung by Bømlo) closely resembles the bedded cherts, but exhibits a much lower Al_2O_3 content, and significantly lower trace element contents and REE sum (2.8 ppm). Jasper (late Cambrian) differs vastly, no layering is present and Fe_2O_3 and SiO_2 ($\sim 3 - 23 \text{ wt}\%$ and $\sim 75 - 92 \text{ wt}\%$, respectively) dominate, while Al_2O_3 is negligibly low. Trace element and REE concentrations are very low ($\sum\text{REE} \sim 1.1 - 3.0 \text{ ppm}$). Two types of jasper can be distinguished. Abiogenic jasper (Geitung by Bømlo) is characterised by the absence of filaments, but contains hematite crystals occurring in concentrated clusters of polygonal patches, indicating a gel precursor undergoing syneresis. Microbially induced jasper (Finnås on Bømlo) contains a high abundance of hematite crystals comprising filamentous structures interpreted to be of microbial origin. This study demonstrates that the hematitic cherts on Stord and Bømlo have different formation processes. The hematitic radiolarian cherts are interpreted to have formed mainly from radiolarian ooze and terrigenous/volcaniclastic input. They clearly cannot be seen as analogues to modern Fe-deposits in seafloor hydrothermal systems. The abiogenic and microbially induced jaspers very likely originate from low-temperature hydrothermal fluids, emanating from the seafloor. The abiogenic jasper formation can be explained by diffusely venting fluids forming Fe-Si-oxyhydroxide gels, in which abiogenic precipitation took place. Temperatures were potentially too high for Fe(II)-oxidising chemolithoautotrophs to thrive, explaining the absence of filamentous structures. The microbially induced jasper is interpreted as having formed by diffuse venting leading to mound formation in which redox conditions and temperatures were favourable for Fe(II)-oxidisers, causing filament formation. This can potentially serve as an ancient analogue to modern hydrothermal Fe-deposits found in the Jan Mayen Vent Fields and several other vent fields. The bedded hematitic radiolarian cherts formed during the Lower/Middle Ordovician within a widening back-arc basin with

suboxic seafloor conditions. Landmasses nearby provided terrigenous volcaniclastic input. The jaspers, both abiogenic and microbially induced, formed in the deep sea during the early stages of an immature island arc in the late Cambrian. The late Cambrian radiolarian chert band formed coevally, but during a quiescent phase and was potentially unaffected by hydrothermal fluids.

Acknowledgements

First of all, I am very grateful for Ingunn H. Thorseth having introduced me to geomicrobiology during my exchange year in 2015-2016. Her devotion to the research field led me to wanting to stay at the University of Bergen and explore it more in depth myself. Constructive discussions with and valuable suggestions by her were greatly appreciated, and having been given a lot of freedom in carrying out this study was a new and very exciting experience I genuinely enjoyed. Special thanks are given to Rolf B. Pedersen for his support during field work and for discussing the geological background of the study area with me, not having been exposed to the geological history of Norway until a year ago. My grateful thanks are also extended to Karen C. Johannessen, Leif-Erik R. Pedersen, and Anders Bjerga for always being helpful and providing important tips. Ole Tumyr, Irina M. Dumitru, Martina S. Hamre, and Yuval Ronen are thanked for their support during the sample preparation process, Hildegunn Almelid and Siv H. Dundas for carrying out the geochemical analyses. Irene Heggstad and Trygve Knag have been a great help in refreshing my knowledge on operating the Scanning Electron Microscope. I would also like to thank Håvard H. Stubseid and Andreas L. Viken for discussing the regional geology of our common study area. Furthermore I want to thank my family for support from abroad. Last but not least, my special thanks go to Andrew, for being amazing and always believing in me even when I am in doubt.

Contents

Abstract	i
Acknowledgements	iv
List of Figures	x
List of Tables	xi
Acronyms	xii
1 Introduction	1
1.1 Geobiological background	3
1.1.1 Modern seafloor hydrothermal systems and associated deposits	3
1.1.2 Ancient seafloor hydrothermal system deposits	9
1.2 Geological background	11
1.2.1 Regional geology: The Scandinavian Caledonides	11
1.2.2 Region of interest: Bømlo and Stord	15
2 Materials & Methods	21
2.1 Sampling locations	21
2.1.1 Bømlo	21
2.1.2 Stord	27

2.2	Sample preparation & applied analytical methods	30
2.2.1	Microscopy	30
2.2.2	Bulk geochemistry	31
3	Results	34
3.1	Mineralogy and textures	34
3.1.1	Group A	34
3.1.2	Group B	44
3.2	Bulk geochemistry	58
3.2.1	Group A	58
3.2.2	Group B	63
4	Discussion	72
4.1	Bulk geochemistry - element relationships and their implications	72
4.1.1	Purely hydrothermal origin?	72
4.1.2	Depositional environment	90
4.2	Mineralogy and texture contributions	99
4.2.1	Group-specific traits and their implications	99
4.2.2	Group-overlapping traits and their implications	103
4.3	Formation models	105
4.3.1	Bedded radiolarian chert (Group A)	105
4.3.2	Radiolarian chert band (B-G-1, Group B)	106
4.3.3	Abiogenic jasper (B-G-3a, -3b, and -4, Group B)	107
4.3.4	Microbially induced jasper (B-F-1, Group B)	110
4.4	Contributions of findings to the regional geology	111
5	Conclusions & Outlook	114
	Bibliography	118
	Appendices	136

A	GPS coordinates	137
B	Sampling location photographs	138
C	Sample overview and applied methods	142
D	Correlations major and trace elements Groups A and B	143
E	Correlation REE patterns	144
F	Element and oxide ratios	146

List of Figures

1.1	Seafloor hydrothermal system model	4
1.2	Overview of Scandinavian Caledonides	13
1.3	Geological map of southern Bømlo and southern Stord	16
1.4	Stratigraphy of Bømlo	17
2.1	Sampling location 1: Langevåg	22
2.2	Radiolarian chert, Langevåg	22
2.3	Sampling location 2: Geitung	23
2.4	Hematitic chert band and jasper clast, Geitung	24
2.5	Sampling location 3: Finnås	25
2.6	Jasper clast, Finnås	26
2.7	Sampling location 4: Sagvåg gruve	27
2.8	Chert, Sagvåg gruve	28
2.9	Sampling location 5: Sagvåg, on the coast	29
2.10	Chert, Sagvåg coast	29
3.1	Thin section scans of Group A samples	35
3.2	Quartz in Group A	36
3.3	Hematite in Group A	37
3.4	Hematite, filament-resembling structures in Group A	38
3.5	Mica in Group A	40

3.6	Quartz spheres in Group A	41
3.7	Quartz grain in B-L-1, Group A	42
3.8	Carbonate crystals in Group A	43
3.9	Thin section scans of Group B samples	45
3.10	Magnetite in Group B	46
3.11	Hematite in Group B	48
3.12	More hematite in Group B	50
3.13	Raman spectra magnetite and hematite	51
3.14	Carbonate crystals in Group B	52
3.15	Chlorite in Group B	53
3.16	Raman spectrum chlorite	54
3.17	Various minerals and textures in B-G-1, Group B	56
3.18	Major and trace element correlations Group A	59
3.19	REE normalisations Group A	62
3.20	Major and trace element correlations Group B	65
3.21	Mn and Co correlated for Group A and B samples combined .	66
3.22	REE normalisations Group B	68
4.1	(Ni+Co+Cu)*10-Fe-Mn diagram	73
4.2	Al-Fe-Mn diagram	76
4.3	Correlation SiO ₂ content and \sum REE Groups A and B	77
4.4	Correlation Fe content and REE sum Group A and B	78
4.5	Normalisation of NASC and PAAS over chondrite	81
4.6	REE normalisations Group A and B	82
4.7	Comparison REE patterns samples and potential source fluids	84
4.8	Al ₂ O ₃ /(Al ₂ O ₃ +Fe ₂ O ₃)-(La/Ce) _N diagram	93
4.9	Th-V/100-Sc/10 diagram	98
4.10	Formation model for bedded radiolarian cherts	107
4.11	Formation model for radiolarian chert band	108

4.12	Formation model for abiogenic jasper	109
4.13	Formation model for microbially induced jasper	111
B.1	Location 1: Langevåg, outcrop overview	138
B.2	Location 1: Langevåg, Close-up of bedded radiolarian chert, B-L-3	139
B.3	Location 2: Geitung, Close-up of hematitic radiolarian chert band, B-G-1	139
B.4	Location 2: Geitung, Jasper clast, B-G-4	140
B.5	Hematitic chert, Sagvåg coast	141
D.1	Major and trace element correlations Groups A and B	143

List of Tables

3.1	Summary of mineralogical and textural traits	57
3.2	(La/Yb) _N ratios, Ce/Ce*, and Eu/Eu* Group A	61
3.3	(La/Yb) _N ratios, Ce/Ce*, and Eu/Eu* Group B	67
3.4	Major element concentrations	69
3.5	Trace element concentrations Group A and B	70
3.6	REE concentrations	71
A.1	GPS coordinates sampling locations	137
C.1	Sample list and used analytical methods	142
E.1	Correlations of REE patterns, Chondrite-normalised	144
E.2	Correlations of REE patterns, NASC-normalised	145
E.3	Correlations of REE patterns, PAAS-normalised	145
F.1	Element and oxide ratios	146

Acronyms

BSE Back-Scattered Electron

EDS Energy-Dispersive X-ray Spectroscopy

HFSE High Field Strength Elements

HREE Heavy Rare Earth Element

ICP-MS Inductively Coupled Plasma Mass Spectrometry

ICP-OES Inductively Coupled Plasma Optical Emission Spectrometry

LOI Loss of ignition

LREE Light Rare Earth Element

NASC North American Shale Composite

PAAS Post-Archean Average Shale

REE Rare Earth Element

SE Secondary Electron

SEM Scanning Electron Microscope

1 Introduction

On the islands Bømlo and Stord in southwestern Norway, different types of hematitic cherts are present in the rock record. The generic term “hematitic chert” is used here to describe both radiolarian chert containing hematite and a special subtype rich in iron commonly known as jasper. In general, chert can form in various environments, but hematitic chert is typically believed to be tied to hydrothermal activity on the seafloor in vicinity of volcanogenic massive sulphide deposit formation (e.g. Grenne and Slack, 2003*a*). The investigation of samples from Bømlo and Stord is motivated by the aspiration to better understand the formation processes leading to the deposition of the hematitic cherts and to what extent this improves the understanding of the regional geology.

The samples are of late Cambrian and Lower/Middle Ordovician age, and the lithostratigraphical units they belong to are part of the ophiolitic terrain within the Scandinavian Caledonides in SW Norway (Furnes et al., 1983, Brekke et al., 1984, Sivertsen, 1992, Pedersen and Dunning, 1997).

Hematitic chert, and jaspers in particular, are regarded as an ancient analogue of modern hydrothermal deposits consisting of Fe-oxyhydroxides (e.g. Little and Thorseth, 2002, Little et al., 2004). Microbial activity is involved in the formation of these modern deposits: Fe(II)-oxidising chemolithoautotrophs are responsible for the production of distinct structures like filaments and tubes consisting of iron oxides. These structures, if present

within jasper samples, are considered biosignatures, constituting the base of the ancient analogue theory (e.g. Little et al., 2004). Geochemistry, and Rare Earth Element (REE) concentrations in particular, can be used to trace hydrothermal processes and to distinguish between redox conditions (Johannessen et al., 2017), supported by microscopical investigations.

Examination of mineralogy, structures, and textures of the samples is conducted by employing optical microscopy, scanning electron microscopy, and Raman spectroscopy. Inductively Coupled Plasma Optical Emission Spectrometry (ICP-OES) and Inductively Coupled Plasma Mass Spectrometry (ICP-MS) are used to study the geochemistry with a focus on trace element and REE concentrations. Results are compared to both modern Fe-oxyhydroxide hydrothermal deposits, and ancient hematitic chert deposits interpreted to have formed in seafloor hydrothermal settings.

This study aims to find answers to the following questions:

1. What are the conditions and processes leading to the formation of the different types of hematitic cherts?
2. Can they be used as ancient analogue to modern Fe-deposits formed in seafloor hydrothermal systems?
3. Do these findings help improve the understanding of the geological history of the ophiolitic terrain in SW Norway?

1.1 Geobiological background

1.1.1 Modern seafloor hydrothermal systems and associated deposits

In the early 1970s, the first hydrothermal deposits were discovered on the sea floor (Corliss, 1971). Hydrothermal plumes – modified seawater being discharged from cracks within newly formed oceanic crust – were identified and chemically analysed for the first time several years later by Weiss et al. (1977). And shortly after that, in 1977, active fields of hydrothermal springs at the Galápagos rift were identified and explored (Corliss, 1979). Communities of animals and bacteria were not expected to be found there, but were nevertheless observed, thriving in this environment, due to chemosynthesis conducted by H₂S-oxidising bacteria (Corliss, 1979). One year later, massive sulphide deposits were located along the East Pacific Rise in the Gulf of California (CYAMEX Scientific Team, 1979), indicating that high-temperature hydrothermal discharge must occur on the sea floor (Lowell et al., 1995). Supporting this claim, hydrothermal vent chimneys exhaling metalliferous sulphide particles within the hydrothermal fluids were found in the vicinity of these massive sulphide deposits, and they were termed “black smokers”. The temperatures of these hydrothermal fluids reached 350 to 400 °C (Macdonald et al., 1980, Spiess et al., 1980). Decades of extensive research on hydrothermal vent fields followed, and new vent fields have been discovered along both fast and slow spreading mid-oceanic spreading ridges, arc volcanoes, back-arc spreading centres and intra-plate hotspot volcanoes (InterRidge, 2017). This ongoing research improves the understanding of processes leading to the formation of seafloor hydrothermal systems and their characteristics (Figure 1.1).

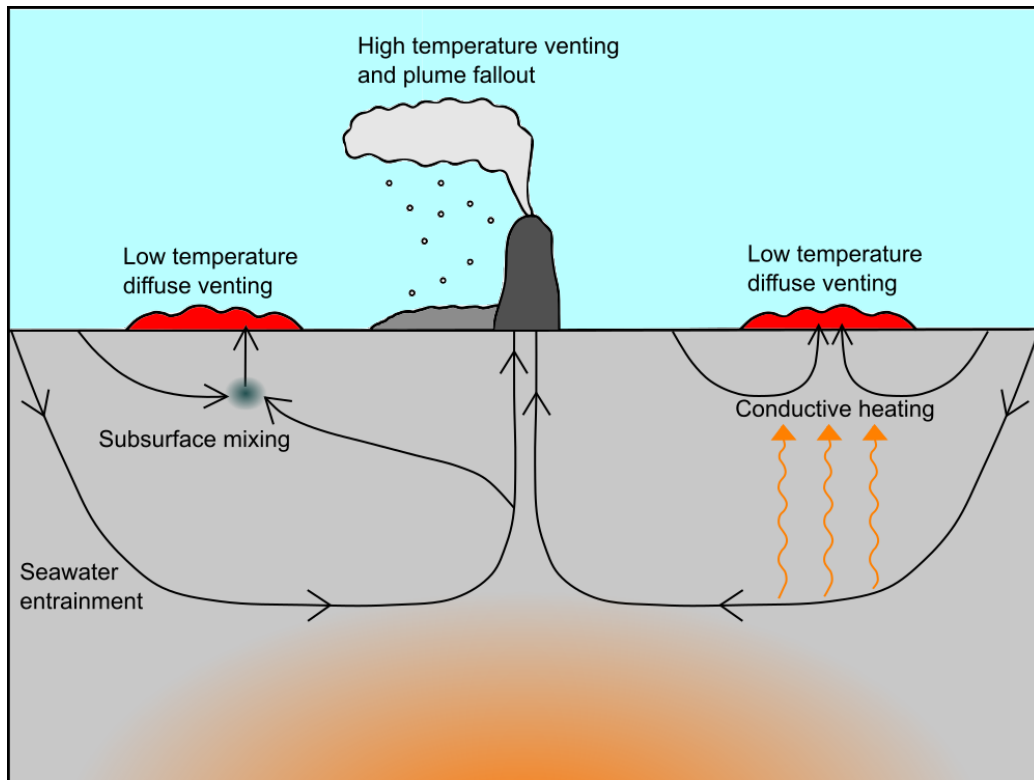


Figure 1.1: Model of seafloor hydrothermal system based on the theories by Alt (1988) and Cooper et al. (2000)

Hydrothermal vents occur in tectonic settings, where upwelling magma underneath the oceanic crust enables seawater to penetrate the oceanic crust downwards through fissures due to percolation (Fisher, 1998). Caused by high temperatures and pressures, the seawater heats up, which leads to recycling through the oceanic crust back to the surface, with the total ocean mass circulating through sea floor hydrothermal systems once every one million years (Wolery and Sleep, 1976). Both on its way down and up again, the heating seawater alters the oceanic crust chemically and leaches certain elements, leading to their dissolution in the seawater. Buoyancy-induced transport upwards causes various hydrothermal deposits to form in the vicinity

of the discharge location (Lowell et al., 1995). The occurring reactions when seawater enters oceanic crust are the following (Alt, 1995, Tivey, 2007):

1. Mg is removed from the fluid, whereas Ca^{2+} , H^+ , and Na^+ become enriched in the fluid, due to smectite and chlorite precipitation.
2. Ca^{2+} and SO_4^{2-} precipitate from the fluid at temperatures above 150°C , and form anhydrite.
3. During albitisation occurring deeper in the oceanic crust, Na^+ and Si are removed from the fluid, in exchange for Ca^{2+} from the anorthite. The hydrothermal fluid at this point is acidic, anoxic, rich in alkalis and depleted in Mg compared to seawater.
4. Leaching of S and metals (Cu, Fe, Mn, Zn, etc.) from the crust by the fluid takes place.
5. Volatiles (^3He , CO_2 , CH_4 , H_2) stemming from the magma below the ridge potentially join the fluid as well (Alt, 1995, Tivey, 2007).

When the hydrothermal fluids discharge through cracks in the sea floor, a rapid temperature loss occurs through mixing with cold seawater, leading to mineral precipitation around the discharge location (Tivey, 2007). Thus, the oceanic crust composition is modified, the chemistry of the ocean is influenced, and – depending on the fluid composition and temperature, oceanic crust composition and structure, and tectonic geometry – different types of hydrothermal deposits are formed (Tivey, 2007).

A very common type of hydrothermal vent is a black smoker chimney. These chimneys exhale high temperature hydrothermal fluids containing dissolved sulphide, leading to the formation of massive sulphide deposits very close to the vents (e.g. CYAMEX Scientific Team, 1979, Macdonald et al., 1980, Spiess et al., 1980). Chimneys exhaling white instead of black clouds of mineral precipitates, show lower temperatures of 100 to 350°C (Macdonald et al., 1980) and are termed “white smokers” due to white precipitates

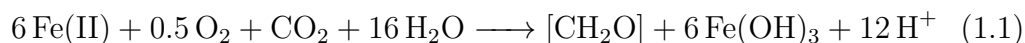
(mainly barite and silica) constituting the chimney and nearby mineral deposits (Macdonald et al., 1980, Spiess et al., 1980). Even though chimney structures with focused hydrothermal fluid flow and their related deposits dominate the sea floor hydrothermal systems, other fluid paths and associated deposits have been discovered since the 1970's. Alt (1988) describes a process of high temperature hydrothermal fluids moving upwards inside the oceanic crust and subsequently mixing with seawater in the subsurface, leading to low-temperature hydrothermal fluids enriched in Si, Mn, and Fe, leading to Fe- and Mn-oxide deposition. This is the classical formation process thought to lead to low-temperature hydrothermal fluid formation. A different formation process for low-temperature hydrothermal fluids has been suggested since (e.g. Cooper et al., 2000). Chemical analyses of diffuse hydrothermal fluids presented by Cooper et al. (2000) provide evidence for seawater entering brecciated oceanic crust material covered with white smoker mineral precipitates along cracks (Langmuir et al., 1997). The cold seawater is penetrating the oceanic crust shallowly and does not get directly heated by the magma chamber at depth, but only conductively by the high-temperature fluids from underneath (Cooper et al., 2000). Very localised mixing of both conductively heated diffuse hydrothermal fluid and high-temperature fluid from below can occur, but is not necessary (Cooper et al., 2000). This type of system exhibits temperatures between $<0.2\text{ }^{\circ}\text{C}$ to $100\text{ }^{\circ}\text{C}$ (Bemis et al., 2012), hence the term "low-temperature hydrothermal system". Low-temperature hydrothermal systems can produce Fe(III)-oxyhydroxide deposits containing layers of Mn-oxides and amorphous silica directly precipitated from the hydrothermal fluids discharged (Alt, 1988). The deposition of Fe- and Mn-deposits depends on the ratio between Fe and H_2S in the hydrothermal fluid before mixing with seawater after discharge: $\text{Fe}/\text{H}_2\text{S} < 1 \rightarrow$ sulphides form and Mn-rich deposits are formed; $\text{Fe}/\text{H}_2\text{S} > 1 \rightarrow$ sulphides form and Fe is still present after all H_2S is used up, leading to Fe- and Fe-Mn-deposits forma-

tion on the sea floor (Alt, 1988). The low-temperature hydrothermal fluids usually display a ratio of Fe/H₂S greater than 1, leading to Fe-oxyhydroxide and Mn-precipitate deposition (Karl et al., 1988). Research has been ongoing over the decades (e.g. Hekinian et al., 1993, Boyd and Scott, 2001, Sun et al., 2015, Johannessen et al., 2017), improving the understanding of these deposits.

The importance of microbial activity

Not only abiotic precipitation from the hydrothermal fluids leads to the formation of hydrothermal deposits, as biological processes take part in it as well (e.g. Boyd and Scott, 2001). Corliss (1979) noted the surprising presence of H₂S-oxidising bacteria conducting chemolithoautotrophy for energy production. This is in accordance with the fact that life in seafloor hydrothermal systems cannot be based on photosynthesis for gaining energy due to the total absence of light. More types of chemolithoautotrophic microbes present in hydrothermal systems have been discovered since, such as aerobic methanotrophs, H₂S-oxidisers, and Fe(II)-oxidisers (Konhauser, 2007a). Oxidation of inorganic components is conducted by these organisms, leading to the release of chemical energy, which is used for carbon fixation by reducing inorganic carbon to organic matter, providing the basis for life in seafloor hydrothermal systems (Falkowski, 2012, Wallmann and Aloisi, 2012). Which process is prevailing over the others is determined by several factors, mainly the hydrothermal fluid composition. Low-temperature hydrothermal fluids usually show a ratio of Fe/H₂S > 1, leading to Fe(II)-oxidation dominating, in contrast to high-temperature hydrothermal fluids with ratios of Fe/H₂S < 1, where H₂S- and CH₄-oxidation predominate (Emerson and Moyer, 2002). Based on morphology, typical representatives of the microaerophilic Fe(II)-oxidising bacteria found at low-temperature hydrothermal vents during early studies are *Gallionella ferruginea* (e.g. Alt, 1988, Juniper and Fouquet, 1988,

Hallbeck and Pedersen, 1991, Emerson and Moyer, 2002) and *Leptothrix ochracea* (e.g. Emerson and Revsbech, 1994, Emerson and Moyer, 2002). *Mariprofundus ferrooxydans* (e.g. Emerson and Moyer, 2002, Emerson et al., 2007, Singer et al., 2011) was later found by 16S rRNA sequencing. By conducting chemosynthesis for energy gain, these organisms generate Fe-oxyhydroxides ($\text{Fe}(\text{OH})_3$) as by-product in the carbon fixation process, see Equation 1.1 (Bekker et al., 2010):



Thus, biomineralisation of Fe-oxyhydroxides can be performed under low oxygen conditions where abiotic precipitation iron oxidation of Fe-oxyhydroxides is 50 times slower than microbial oxidation (e.g. Bekker et al., 2010, Sogaard et al., 2000). These Fe-oxyhydroxides undergo chemical changes during diagenesis (Chan et al., 2011), but keep their specific morphologies, dependent on the Fe-oxidiser: The freshwater genus *L. ochracea* mainly forms rod-like sheaths and tubes (e.g. Emerson and Revsbech, 1994, Emerson and Moyer, 2002, Sun et al., 2012). *G. ferruginea*, also a freshwater genus, produces ribbon-like twisted stalks and branching tubes (e.g. Boyd and Scott, 2001, Emerson and Moyer, 2002, Li et al., 2012). *M. ferrooxydans*, a marine occurring genus belonging to the Zetaproteobacteria, shows very similar twisted stalk and branching morphologies (e.g. Sun et al., 2015, Johannessen et al., 2017) and have actually proven to be much more prevalent in seafloor hydrothermal systems than the freshwater genera *G. ferruginea* and *L. ochracea* (Emerson and Moyer, 2002, Emerson et al., 2007). The morphology of stalks and filaments produced by Fe-oxidising bacteria is caused by its function. Stalks are interpreted to hold the bacterium in place between gradients of O_2 and $\text{Fe}(\text{II})$, which are favourable for the cells' needs, and also to allow the bacterium to escape encrustation by abiotic precipitates (Chan et al., 2011, 2016). Furthermore, the stalk serves as a mineralisation site for the deposi-

tion of products of the bacterium's metabolism (Chan et al., 2011). These specific morphologies of the Fe-oxyhydroxide deposits produced by biomineralisation can be used to better understand the formation processes and prevailing conditions during formation (e.g. Johannessen et al., 2017). Johannessen et al. (2017) investigated Fe-mound deposits from the Jan Mayen Vent Fields located at the Mohns Ridge spreading zone between the Greenland Sea and Norwegian Sea. Their findings imply a low-temperature hydrothermal source fluid instead of high-temperature venting fluids, and substantial contribution of microbial Fe-oxidation to the formation of the deposits. Filaments, fibres, and stalks, encrusted with Fe-precipitates very much resembling the extracellular stalks produced by Fe-oxidising bacteria were found, constituting most of the deposit material. Performed gene sequence analyses prove the abundance of *Mariprofundus ferroxidans* and possibly members of the *Gallionella* genus within the deposits, who are thus responsible for the majority of Fe precipitation, besides abiotic precipitation.

1.1.2 Ancient seafloor hydrothermal system deposits

The Fe-oxyhydroxide deposits can not only be used to investigate formation processes and the ambient conditions in modern seafloor hydrothermal systems. They can also serve as biosignatures in the investigation of ancient hydrothermal deposits such as banded iron formations and jaspers in order to examine the early evolution of life, along with formation processes and environmental constraints for Fe-oxyhydroxide deposition (Johannessen et al., 2017). Comparing structures within jasper deposits with the morphologies of modern hydrothermal Fe-oxyhydroxide deposits has showed strong similarities, indicating that the same microbial communities were actively contributing to the jasper formation (e.g. Juniper and Fouquet, 1988, Duhig, Davidson and Stolz, 1992, Hofmann and Farmer, 2000, Little and Thorseth, 2002, Little

et al., 2004). Fe-oxyhydroxides are relatively unstable phases that undergo change during diagenesis (Konhauser, 2007*b*); dehydration and internal rearrangement of Fe–O–Fe bonds lead to hematite formation (e.g. Schwertmann and Fitzpatrick, 1992, Banfield et al., 2000). These internal rearrangements are believed to not affect the distinct morphologies, as the original structures are preserved as hematite microfossils (Picard et al., 2015), enabling the comparison of modern and ancient hydrothermal vent deposits (e.g. Little et al., 2004). Using morphology as evidence for likeness can turn out to be problematic, as seen in the intensely discussed article by Dodd et al. (2017): It is claimed that the oldest evidence for early life on Earth are preserved in hydrothermal vent precipitates older than 3.77 Gyr, due to – amongst other reasons – the morphological similarities between the precipitates, Ordovician jasper from the Løkken ophiolite (Norway) (Grenne and Slack, 2003*a*), and modern Fe-oxyhydroxide microbial precipitates. Their biogenicity is disputable, it cannot be proven that the investigated structures (hematite tubes and filaments) were exclusively formed by biogenic processes, and evidence from carbon isotopes signatures is not a strong enough indicator to rule out an abiogenic formation. Other lines of evidence are not fully compelling either, leading to their claims being problematic.

Not all fossil hydrothermal systems show evidence for direct microbial activity associated with low-temperature hydrothermal venting, contributing to the Fe-oxyhydroxide precipitation. Some are believed to be regional fallout of Si-Fe-colloids from non-buoyant plumes produced by high-temperature hydrothermal venting (Grenne and Slack, 2003*b*, Slack et al., 2007). Evidence for Fe-oxidation conducted by microbes within hydrothermal plumes today has not been found (Sylvan et al., 2012, Dick et al., 2013), making it necessary to define in which manner Fe-oxyhydroxides constituting ancient Fe-deposits formed. Along with the difficulties morphological comparisons bring along, other methods are necessary to carefully identify the setting and

conditions for Fe-oxyhydroxide formation within seafloor hydrothermal systems (Johannessen et al., 2017). The use of REE patterns and trace element concentration characteristics are robust methods that are on hand and are used in this study. They have proven to be effective over a long period of time and have continually improved (e.g. German et al., 1990, Duhig, Davidson and Stolz, 1992, Duhig, Stolz, Davidson and Large, 1992, Hekinian et al., 1993, Murray, 1994, Leistel et al., 1998, Davidson et al., 2001, Bolhar et al., 2005, Grenne and Slack, 2005, Slack et al., 2007, Johannessen et al., 2017).

1.2 Geological background

1.2.1 Regional geology: The Scandinavian Caledonides

As part of the North Atlantic Caledonides, the Scandinavian Caledonides are the predominant orogen in Northern Europe (Gee, 1975). In western Scandinavia, the orogen is exposed over a length of approximately 1500 km (Corfu et al., 2014) with a general N-S-orientation and a width of up to 300 km (Roberts and Gee, 1985). Stord and Bømlø as regions of interest are located within the southernmost end of the Scandinavian Caledonides. A generalised and, according to Corfu et al. (2014), oversimplified model of the formation of the Scandinavian Caledonides has been introduced by Gee (1975), who pursued an old theory by Törnebohm (1888). During the so-called Caledonian orogenesis, thrust nappes of different origin were emplaced on top of the Baltoscandian/Fennoscandian Precambrian crystalline basement, due to collisional forces in west to east orientation (Gee, 1975, Roberts and Gee, 1985).

The evolution of this thrust nappe-dominated orogen began during the Ediacaran Period at the end of the Neoproterozoic, with a developing seafloor spreading zone between the palaeo-continent Laurentia and Baltica

(Gee, 1975, Roberts and Gee, 1985). As a result, the Iapetus Ocean formed and it continued to widen during the Cambrian (Gee, 1975). During the Ordovician, a reversal of tectonic processes occurred, and Laurentia and Baltica started converging, leading to the gradual closing of the Iapetus Ocean (Gee, 1975). Other, exotic terranes and outboard oceanic domains (e.g. ophiolite complexes and island arc complexes) are presumed to have been involved (Roberts and Gee, 1985, Corfu et al., 2007), leading to a complication of the relatively simple model presented by Gee (1975). During the Silurian, oblique convergence between Laurentia and Baltica continued, and ophiolite complexes and island arc complexes that formed in the Iapetus Ocean either close to the Baltic margin, as suggested by Brekke et al. (1984) and Roberts et al. (1985), or in vicinity to the Laurentian margin (Pedersen et al., 1992, Pedersen and Dunning, 1997), were accreted to either of the margins prior to the collision of the palaeo-continent. Towards the end of the Silurian, the Scandian collisional phase began and endured until the early Devonian (Gee, 1975, Stephens and Gee, 1985, Roberts, 2003). In this phase, the continental margin of Baltica became partly subducted beneath Laurentia (Stephens and Gee, 1985, 1989, Roberts, 2003) and parts of the Caldeonian rocks were exposed to high/ultra-high pressures (Hacker and Gans, 2005). Later on during the collision, material from both Laurentia and the subducted margin of Baltica were thrust onto the Precambrian crystalline basement of Baltica and formed an orogenic wedge of thrust nappes (Gee, 1975, Stephens and Gee, 1989). The displacement of the nappes was enabled by a layer of phyllites within the sediments on top of the Precambrian crystalline basement of Baltica (Fossen, 1992). Within the phyllites, a basal detachment fault developed and the forming thrust nappes were able to glide along this plane on top of the Baltoscandian/Fennoscandian shield (Fossen, 1992).

The tectonostratigraphic division of the Caledonian belt suggested by Roberts et al. (1985) separates the thrust nappes in four units, respective to

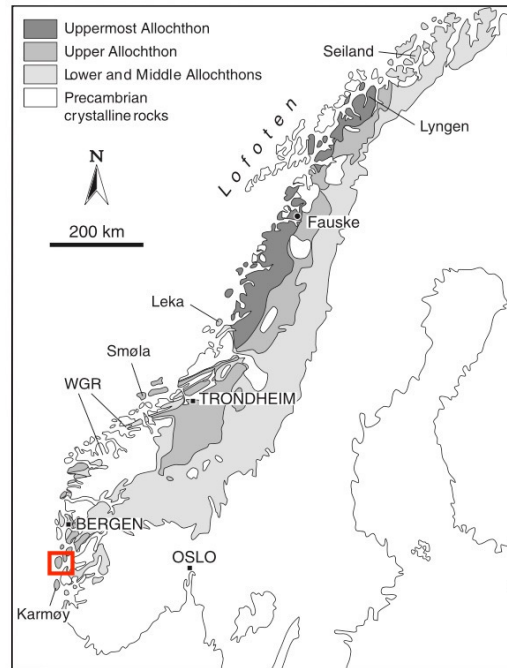


Figure 1.2: Overview of the Scandinavian Caledonides after the scheme introduced by Roberts and Gee (1985), map from Roberts (2003). Roberts (2003) grouped the Lower and Middle Allochthon together for better visibility and due to the fact that both the Lower and Middle Allochthon have the same origin. Region of interest marked in red.

origin: the Lower, the Middle, the Upper, and the Uppermost Allochthon. Figure 1.2 shows a sketch of these units and their location in Scandinavia. The Lower Allochthon is constituted of sediments from the late Proterozoic up to the early Paleozoic that were strongly affected by tectonic activity (Roberts and Gee, 1985). They were identified to stem from the margin of Baltica prior to the Caledonian orogenesis (Stephens and Gee, 1985).

The Middle Allochthon partly overlies the latter, and Precambrian crystalline rocks (mainly highly deformed gneisses) and late Precambrian fossil-free sediments are established as one thrust nappe unit (Roberts and Gee,

1985). It also derives from the margin of Baltica (Stephens and Gee, 1989).

The Upper Allochthon includes a more heterogeneous unit that is regarded as not being endemic to Baltica (Bingen and Solli, 2009). Oceanic volcanosedimentary successions with different origins are grouped together as outboard, exotic terranes, that are presumed to have formed within or in close vicinity to the Iapetus Ocean (Roberts and Gee, 1985, Stephens and Gee, 1989). Part of these outboard terranes are ophiolite complexes that have been obducted, fragmented, and deformed during the late Cambrian and Lower Ordovician, up until the Scandian collisional phase (Roberts and Gee, 1985).

The Uppermost Allochthon consists of several metamorphic rock types, only present in the northernmost exposed part of the Scandinavian Caledonides (Roberts and Gee, 1985). It is interpreted to display the remains of the continental margin of Laurentia (Stephens and Gee, 1985, 1989).

Subsequent to the Scandian collisional phase, the Scandinavian Caledonides were shaped by extensional processes during the Lower and Middle Devonian (Fossen, 2010). The consistent southeast-oriented collision was followed by a material transport in the opposite direction, to the west and northwest, mainly visible in SW Norway (Fossen, 2010). This back-sliding of the orogenic wedge occurred along the basal detachment fault zone responsible for the thrusting of the nappe units onto the Precambrian shield, due to the reverse reactivation of these thrusts (Fossen, 1992). The reason for this is thought to be crustal extension processes, later also having lead to the formation of extensional shear zones dipping west- and northwest, cutting through the thrust nappes and continuing into the Precambrian basement (Fossen, 1992). In southwestern Norway, the Hardangerfjord Shear Zone is a prominent example with a length of up to 500 km, showing evidence for even reaching into the lower crust of the Precambrian basement, also affecting Stord and Bømlo (Fossen and Hurich, 2005).

1.2.2 Region of interest: Bømlo and Stord

The islands Bømlo and Stord (to the east of Bømlo) consist of rocks attributed to the Upper Allochthon and Brekke et al. (1984) interpreted the ophiolitic terrain and remnants of island arc complexes to have formed near the continental margin of Baltica. A different formation origin is supported by Pedersen et al. (1992) and Pedersen and Dunning (1997). Ordovician faunal data found in remnants of the outboard and exotic terranes resemble the Ordovician Laurentian fauna more than the fauna found within Baltica (Pedersen et al., 1992) More evidence for a formation in the proximity of the Laurentian margin are zircons of Archean age with Laurentia as very likely source since Baltica's Precambrian shield does not contain rocks that old (Pedersen and Dunning, 1997). Also, the Baltic margin is believed to mainly having been passive until the Scandian collision (McKerrow et al., 1991, Scotese and McKerrow, 1991, Roberts, 2003). In contrast, the Laurentian margin is found to have been more active, having had accretional processes occurring between the late Cambrian until the Middle Ordovician (Zagorevski et al., 2006). Andersen and Andresen (1994) endorse the theory of the outboard terranes having formed closer to the Laurentian margin. The material has then later been thrust onto the Baltic shield during the Scandian collision (Andersen and Andresen, 1994, Roberts, 2003), constituting the Upper Allochthon.

Bømlo Brekke et al. (1984) and Nordås et al. (1985) investigated the southern and central part of Bømlo. The North is dominated by rocks from the Sunnhordland Batholith (Andersen and Andresen, 1994) that intruded after formation of the Caledonian rocks on Bømlo and is not of interest here. In Figure 1.3, a geological map of Bømlo and Stord is shown. Figure 1.4 presents the stratigraphy of major units on Bømlo.

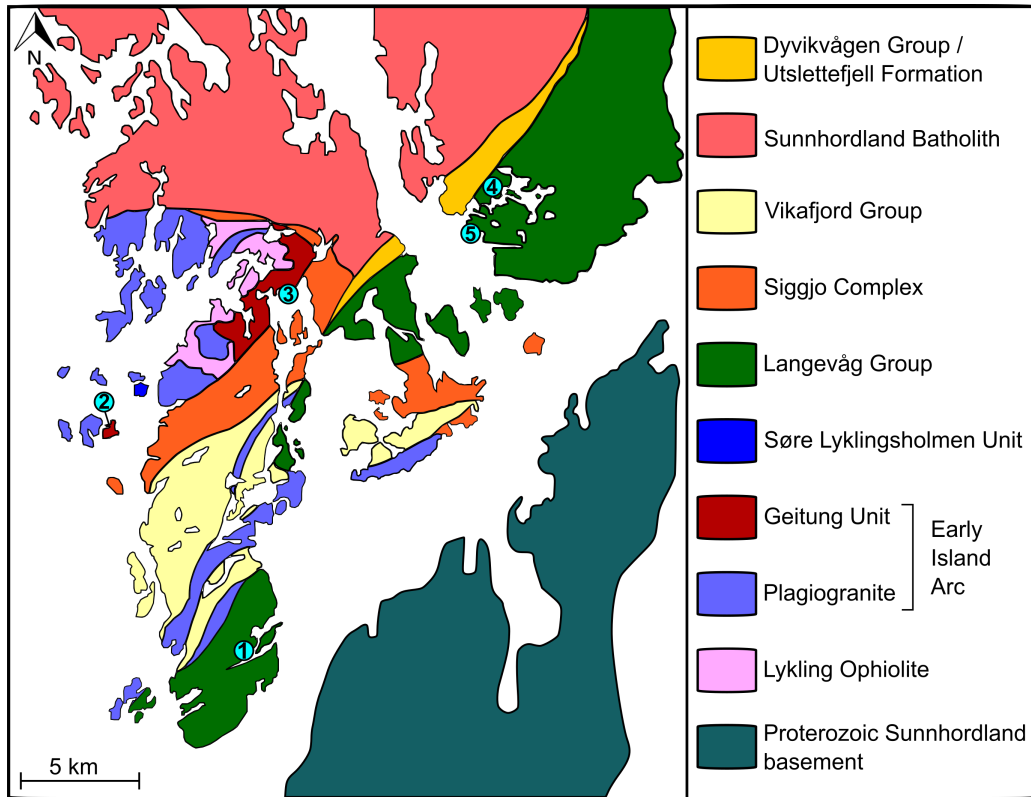


Figure 1.3: Simplified geological map of southern Bømlo and southern Stord modified after Brekke et al. (1984), Færseth (1982), Andersen and Andresen (1994), and Sivertsen (1992). Sampling locations are indicated with blue numbered dots. The chronological order of lithostratigraphic units is discussed in the text.

The oldest rock unit present on southern and central Bømlo is the Lykling Ophiolite (Brekke et al., 1984). Its absolute age is still undefined, but structural evidence strengthens the theory of it being older than the other units in the area (Brekke et al., 1984). It is presumed that it was formed by sea floor spreading above a subduction zone (Pedersen and Dunning, 1997).

Unconformably overlying the Lykling Ophiolite, the Geitung Unit con-

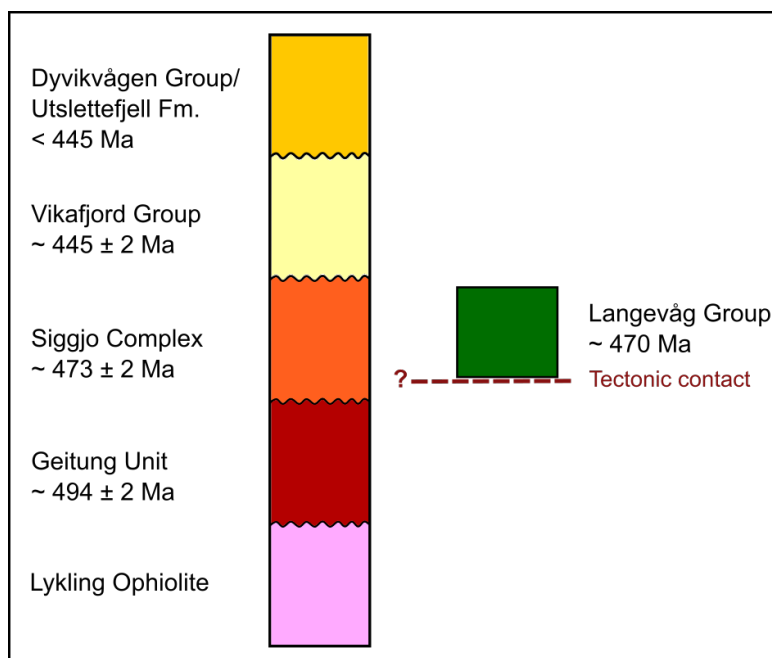


Figure 1.4: Overview of relevant lithostratigraphical units on Bømlo after Brekke et al. (1984), Færseth (1982), Pedersen and Dunning (1997), and Stubseid (2017)

sists of extrusive volcanics and sedimentary rocks (Brekke et al., 1984, Nordås et al., 1985). Trace element patterns of metabasalts indicate strong similarities with ensimatic, immature tholeiitic island arc basalts, leading to the assumption that the Geitung Unit was formed during an early stage of an island arc developing (Brekke et al., 1984, Pedersen and Dunning, 1997). Dating the unit, Furnes et al. (1983) determined a Rb/Sr whole rock age of 535 ± 46 Myr for the Geitung Unit. Later U-Pb dating of zircons within basaltic-andesites gave a crystallisation age of 494 ± 2 Myr (Pedersen and Dunning, 1997), placing its formation in the Furongian (late Cambrian). Zircons from a siltstone yield the same age, strengthening the formation theory of the Geitung Unit during the late Cambrian, and indicating that the im-

mature island arc itself was the source for the siltstones (Viken, 2017).

Both the Lykling Ophiolite and the Geitung Unit underwent folding and erosion prior to the deposition of the next unit unconformably overlying them, the Siggjo Complex (Pedersen and Dunning, 1997). The Siggjo Complex consists of subaerial volcanics and sedimentary rocks (Brekke et al., 1984, Nordås et al., 1985). Their geochemistry identifies the unit as a calc-alkaline, mature island arc sequence (Brekke et al., 1984, Furnes et al., 1986, Pedersen and Dunning, 1997). Pedersen and Dunning (1997) dated zircons from this unit, using U-Pb dating, to be 473 ± 2 Myr old, defining the formation period to be Lower to Middle Ordovician and giving the unit a more exact age than Brekke et al. (1984).

The Siggjo Complex is unconformably overlain by the Vikafjord Group unit (Brekke et al., 1984). This unit mainly consists of sedimentary rocks and mafic volcanic rocks (Figure 1.4), which are interpreted to have been shaped by alluvial and shallow-marine depositional processes, followed by marine transgressions and later by subaerial, mafic volcanism (Brekke et al., 1984). Stubseid (2017) correlates the Vikafjord Group with the Mundheim Group (present northeast of Stord), which has been radiometrically dated at approximately 445 Ma (Rb-Sr).

The Dyvikvågen Group/Utslettefjell Formation unconformably overlies the Vikafjord Group and is assumed to be of Lower Silurian age and thus younger than the Vikafjord Group (Færseth, 1982).

The last main unit defined by Brekke et al. (1984) is the Langevåg Group, which has been interpreted in several ways. Volcanics and marine sediments, including radiolarian cherts, characterise it and are interpreted to depict the formation and deepening of a marine basin (Brekke et al., 1984). Færseth (1982) understands this group as a part of the Hardangerfjord Group believed to contain the oldest rocks of Caledonian age in the area. Brekke et al. (1984) on the other hand interpreted the Langevåg Group to be the

youngest unit in the area. In Sivertsen (1992), a different view is presented: The Langevåg Group correlates to a member of the Velle Formation belonging to the Torvastad Group associated with the Karmøy Ophiolite Complex (south of Bømlo). According to this, the Langevåg Group is assumed to have developed in a widening back-arc basin setting (Sivertsen, 1992), during the Lower to Middle Ordovician, approximately 470 Ma (Pedersen and Dunning, 1997, Viken, 2017). This interpretation of the Langevåg Group is adopted in this study. The Langevåg Group exhibits a tectonic contact with the Siggjo Complex (R.B. Pedersen, personal communication, November 2017). Sivertsen (1992) also presumes the mature island arc responsible for the Siggjo Complex to be the source of the volcanoclastic material deposited within the back-arc basin, leading to the deposition of volcanoclastic formations within the Langevåg Group.

Stord The lithostratigraphy on Stord is similar to Bømlo (Figure 1.3). Several studies on the region have been conducted with a focus on the lithostratigraphy, of which the most recent one is Andersen and Andresen (1994). According to their findings, the oldest rocks on Stord originate from ophiolites and island arcs, probably from the same geological setting as the Lykling Ophiolite and Geitung Unit on Bømlo, and are 495 to 470 Myr old. They are found in the centre and the north of Stord.

The subsequently younger unit, according to Andersen and Andresen (1994), is the Kattnakken Volcanics, which is believed to be of the same age and formation evolution as the Siggjo Complex on Bømlo, approximately 476 to 473 Myr. They are found on central Stord, southeast to the ophiolite/island arc rocks.

The southern and southwestern areas of Stord are dominated by deep-marine and volcanic metasediments (Andersen and Jansen, 1987, Andersen and Andresen, 1994). Andersen and Jansen (1987) deemed this unit to be

the same as the Langevåg Group after Brekke et al. (1984) on Bømlo.

Just to the north of it, there is a conglomerate-dominated unit, the Dyvikvågen Group (Andersen and Jansen, 1987). It is believed to have formed at the end of the Upper Ordovician and the beginning of the Silurian (Færseth, 1982, Andersen and Jansen, 1987, Andersen and Andresen, 1994).

The geological unit dominating the north on Stord is the Sunnhordland Batholith (Andersen and Andresen, 1994). It intruded Caledonian rocks during the Middle/Upper Ordovician-early Silurian, prior to the Scandian collisional period due to ocean-continent convergence (Andersen and Jansen, 1987).

Lithostratigraphical units important in this study: Samples were taken from the Geitung Unit, with an age of 494 ± 2 Myr (Pedersen and Dunning, 1997), and thus having formed during the late Cambrian, and the younger Langevåg Group, being approximately 470 Myr old (Pedersen and Dunning, 1997) from the Lower to Middle Ordovician. The geological settings responsible for their formation are an immature island arc (Brekke et al., 1984, Pedersen and Dunning, 1997), and a widening back-arc basin (Sivertsen, 1992, Pedersen and Dunning, 1997), respectively.

2 Materials & Methods

2.1 Sampling locations

2.1.1 Bømlo

Three locations on the island group of Bømlo were sampled on 15.10.2016. GPS coordinates for all sampling locations are provided in Table A.1 in the appendix, as well as additional photographs.

Location 1: Langevåg On southern Bømlo, by the village of Langevåg, three samples were obtained (Figure 2.1). The outcrop sampled is roughly 100 m long and consists of bedded radiolarian chert. Figure 2.2 shows the location where sample B-L-3 was taken. The interlayering of marine, formerly clay-rich sediments (grey) and radiolarian chert (purple-red) is easily visible. Grey layers have average thicknesses of 2 cm, and red layers are approximately 5 cm thick. Internal layering within the red layers can be observed macroscopically, distinguishable by slight colour variations. Secondary quartz veins cross-cut the ribbon chert layers, and wavy deformation of the chert can be observed. Only parts of the red layers were sampled. The lithostratigraphical unit the sampling location is part of, is deemed to be the Langevåg Group.

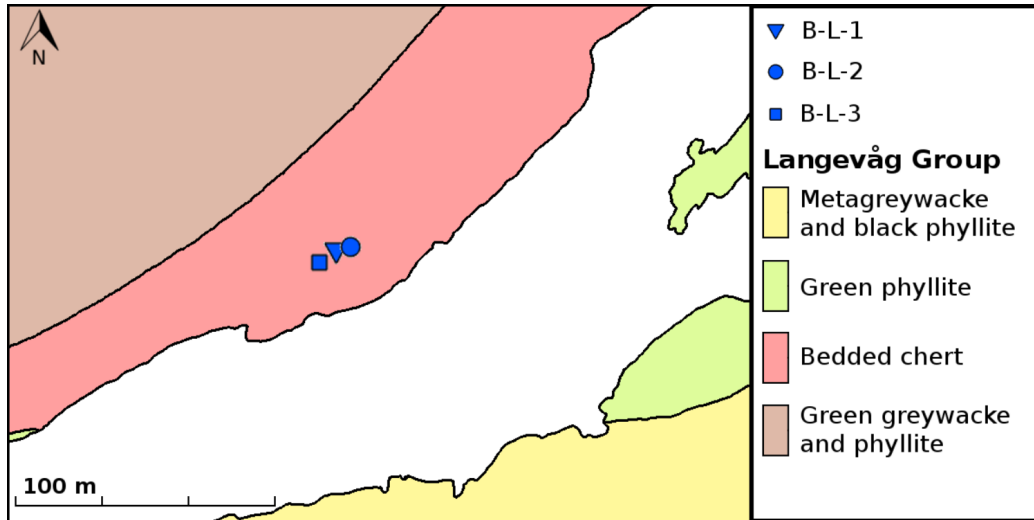


Figure 2.1: Sampling location 1: Langevåg on southern Bømlo



Figure 2.2: Bedded radiolarian chert, location of B-L-3

Location 2: Geitung 11 km northwest of Langevåg, six samples were taken at the small island Geitung (Figure 2.3). One sample stems from a hematitic chert band (Figure 2.4a), whereas four samples were taken from jasper clasts embedded in volcanoclastic breccia (Figure 2.4b, sampling location of B-G-3a shown). The hematitic chert band is about one meter long and has a maximum thickness of 6 cm, thinning out towards the sides. Its purple-red colour distinguishes it from the surrounding greyish metasandstone. Similarly to the samples from Location 1, colour variations can be seen within, indicating some sort of layering. The jasper clasts sampled, on the other hand, show different traits macroscopically. The clasts have variable diameters of 15 cm to 40 cm and exhibit spheroidal shapes. The colour is more red instead of purple-red, and no layering is visible. Zones of more intensive red colours are embedded in less red material. The rocks sampled at Location 2 belong to the Geitung Unit.

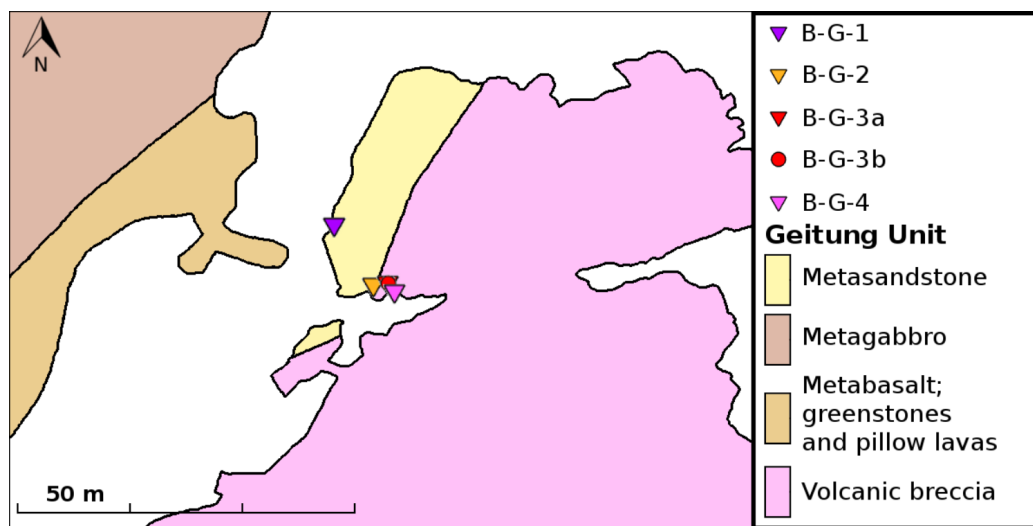


Figure 2.3: Sampling location 2: Geitung at the western coast of Bømlo



(a) Hematitic chert band, B-G-1



(b) Jasper clast, B-G-3a

Figure 2.4: Images of selected sampling locations on Geitung

Location 3: Finnås Approximately 9 km northeast of Geitung, in the Finnås area, one sample was obtained. The location is indicated on the map in Figure 2.5. The sample stems from a dark red jasper clast embedded within basal conglomerate, overlain by brecciated pillow lavas of the Geitung Unit, and underlain by volcanics of the Siggjo Complex. Photographs of the sampled clast are shown in Figure 2.6. Several clasts were present, but only one was sampled due to complicated sampling conditions right by the coast and extreme hardness of the material. The appearance of the jasper clast resembles the clasts sampled at Location 2, except for the more intense red colour. No distinct layering is observed and the deep red colour is macroscopically fairly homogeneous. The geological map by Brekke et al. (1984) (Figure 1.3) indicates that this sample is also part of the Geitung Unit.

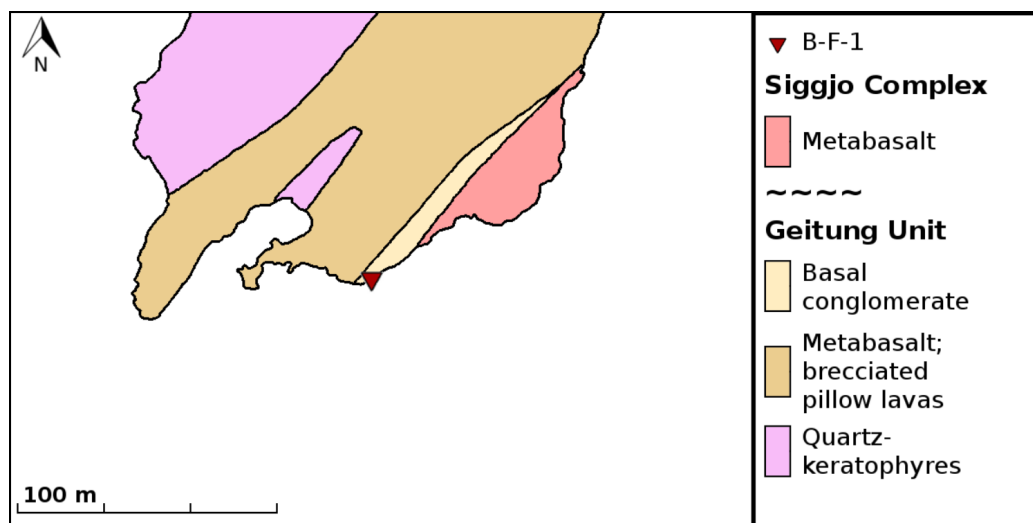


Figure 2.5: Sampling location 3: Finnås in the central area of Bømlo



(a) Jasper clasts, only the smaller one has been sampled

(b) A closer look at the smaller clast, sample B-F-1 was taken here



(c) Jasper clast embedded in basal conglomerate

Figure 2.6: Images of the sampling location for B-F-1

2.1.2 Stord

Two locations on Stord were sampled prior to 15.10.2016, during field work for a different project. Both are in the vicinity of the village of Sagvåg.

Location 4: Sagvåg gruve Adjacent to the abandoned pyrite mine by Litlabø (Sagvåg), one sample was obtained (Figure 2.7). It was taken from a layer/lens of slightly deformed chert, exhibiting a light grey-purple colour and leached white layers that were not sampled (figure 2.8). It is embedded in altered basaltic greenschist, tuff, and lava (Norges Geologiske Undersøkelse, 2017) and appears as several “lenses” (100 to 1500 m length, 40 m average width) over an area of a few square kilometres. The lithostratigraphical unit the chert layer belongs to, shares similarities with both the Torvastad Group on Karmøy (Sivertsen, 1992) and the Langevåg Group on Bømlo (Brekke et al., 1984) and is believed to have formed at the same time, under the same conditions (Andersen and Jansen, 1987).

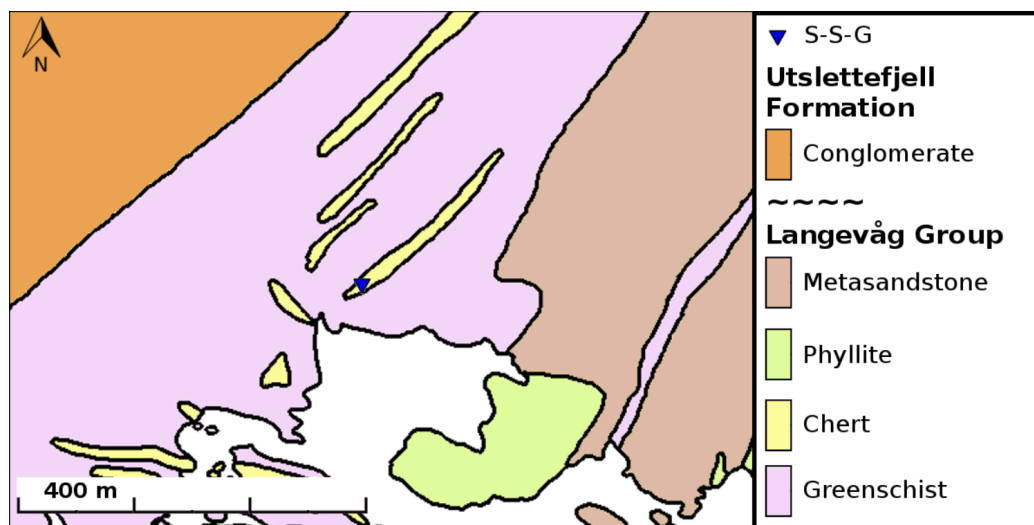


Figure 2.7: Sampling location 4: Sagvåg gruve



Figure 2.8: Hematitic chert by Sagvåg gruve, photo courtesy of Rolf B. Pedersen

Location 5: Sagvåg, on the coast Three kilometres to the southwest of Location 4, another layer/lens of chert was sampled, on the coast of Stord (Figure 2.9). Only one sample was collected at this location from a slightly bleached light grey-red chert layer exhibiting similar layering between clay-rich sediments (grey) and chert units (purple-red, Figure 2.10). The lithostratigraphical setting is identical with Location 4, and macroscopically the sample resembles the one taken at Location 4, with the only difference that it exhibits stronger deformation structures.

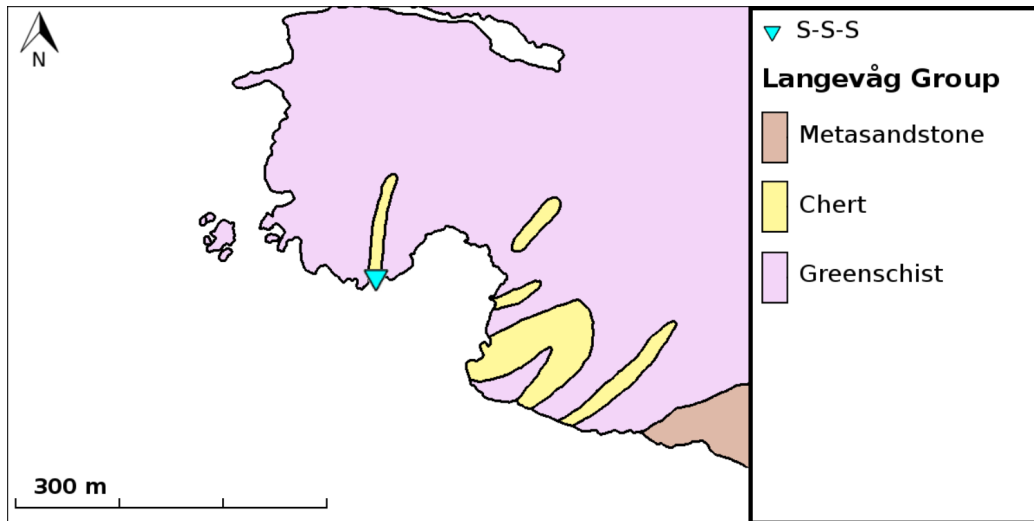


Figure 2.9: Sampling location 5: Sagvåg, on the coast



Figure 2.10: Hematitic chert on the coast of Stord near Sagvåg, photo courtesy of Ingunn H. Thorseth

2.2 Sample preparation & applied analytical methods

11 samples were obtained with hammer and chisel in the field, of which not all underwent the same treatment. Table C.1 in the appendix provides an overview of sample preparation and analytical methods used. One sample, B-G-2, was omitted from the analysis and wholly unused due to an insufficient sample size. For the remaining 10 samples, thin sections were produced for optical microscopy, scanning electron microscopy, and Raman spectroscopy. 9 out of the 10 samples undergoing mineralogical and textural analysis were also additionally prepared for bulk geochemistry analysis with the application of ICP-OES and ICP-MS.

2.2.1 Microscopy

Thin section preparation In order to investigate both mineralogy and textures of the jasper and chert samples, 10 polished, petrographic thin sections with a thickness of 30 μm were produced. To enable working with both the Optical and the Scanning Electron Microscope (SEM), and the Raman spectrometer, the samples were not covered with a thin glass plate. For SEM work the thin sections were coated with carbon. An Agar Turbo carbon coater was used to minimise charging of the sample when acquiring images and implementing Energy-Dispersive X-ray Spectroscopy (EDS) for point geochemistry measurements.

Optical microscopy A Nikon Eclipse LV100POL microscope was used for conducting optical microscopy, including a DS-F1 Nikon digital sight camera and NIS-Elements imaging software for image acquisition. A magnification factor of up to 50 can be obtained with this type of microscope, without

making use of the oil lenses. For most of the mineralogical and textural analyses this was sufficient, but for several features the SEM was a helpful addition, enabling much higher magnification factors.

Scanning electron microscopy Images of textures on very small scales were acquired with a Zeiss Supra 55VP field emission SEM. To strengthen the insight into mineralogy gained with optical microscopy, indicative chemical point analyses were conducted by utilising an EDS system of the type Thermo NORAN System Six connected to the SEM. The operation parameters were a voltage of 15.0 kV and an average working distance of 9 mm, and Back-Scattered Electron (BSE) and Secondary Electron (SE) detectors were used for both imaging of textures and chemical analysis.

Raman spectroscopy A Raman spectrometer (type: Horiba Jobin Yvon LabRAM *HR*), using a 514 nm laser wavelength, was additionally applied to differentiate between specific mineral phases that are usually hard to distinguish by optical microscopy alone.

2.2.2 Bulk geochemistry

Sample preparation 9 samples were chosen for bulk geochemistry analysis, excluding sample S-S-G. The preparation of the samples for bulk geochemistry contained several steps. In order to only obtain rock material that has not been affected by weathering, samples of sufficient size were cut, using a rock saw with a diamond blade. A piece from the centre with no weathering surfaces was taken for each sample and was prepared further. This was only possible for three samples. The majority of the samples were too small, so they had to be pre-crushed using a hammer and then sorted for further crushing. For the jasper samples, only the rock fragments with the brightest red colour and without weathering surfaces were picked to maximise the amount

of iron phases for the analyses. For both the sawed and hand-sorted samples the procedure was the same: a hammer and a steel plate on a crushing block were used to crush the rock fragments to a grain size of <1 mm. The sample material was carefully wrapped in plastic foil, and paper around it was additionally used to minimise material loss and contamination. The hardness of the rocks made the crushing process quite difficult, but careful and very slow work made it possible to crush a sufficient amount. After crushing the samples, they were each washed three times with ethanol whilst standing in an ultrasonic bath. This was done to remove any fine metallic splinters or dust from the steel hammer and plate that could have contaminated the sample. In order to further prepare the sample material, it was dried for 24 hours in a drying cabinet at 50°C to expedite ethanol evaporation. After drying, the sample material was milled using a Retsch MM 200 vibratory mill. 2 g of milled material per sample were desired, but unfortunately some of the samples were too small and weathered to reach that amount (Table C.1 on page 142 in the appendix). 0.35 g were used for further sample preparation for ICP-OES and ICP-MS. Exactly 0.1 g of the milled sample material was weighed out and solubilised in 3 ml concentrated hydrofluoric acid at 135°C for 48 hours. After evaporation of the HF supernatant, nitrate salts were created by adding a weak solution of HNO_3 while keeping the samples heated. The residue was dissolved with 2 ml 2N HNO_3 in volumetric flasks and then diluted with 2% HNO_3 , filled up to 50 ml.

Inductively Coupled Plasma Optical Emission Spectrometry ICP-OES was implemented in order to detect major and trace elements, making use of the element-specific emission of electromagnetic radiation to identify their concentrations even on ppm level by igniting the dissolved sample material and ionizing elements. Due to dissolution with hydrofluoric acid, Si cannot be analysed with ICP-OES and the Si concentrations needed to be

calculated with the aid of the concentrations of detected major elements. A Thermo Scientific – iCAP ICP optical emission spectrometer was used. The implemented standard for quality control was BCR-2, a USGS-certified reference standard. Scandium was added as an internal standard. The accuracy achieved was better than 4.7 % for the major elements and better than 6.2 % for trace elements, with the exception of Cr and Ni (17.1 % and 10.3 %, respectively). Several ICP-OES trace element data either had larger accuracies than the ICP-MS data counterparts or were very close to/below the respective detection limits, resulting in the preference of ICP-MS data in such cases. BCR-2 measurements gave precisions better than 5.9 % for ICP-OES data used.

Inductively Coupled Plasma Mass Spectrometry The detection and quantification of trace elements and REEs at lower concentrations requires the application of ICP-MS. The quantification of elements is acquired by ion separation dependent on their mass-to-charge ratio. A higher precision can be obtained, even down to parts per quadrillion (ppq) levels for some elements. A Thermo Finnigan Element 2 high-resolution ICP mass spectrometer was used. For both trace element and REE measurements, BCR-2 was used as standard and was measured repeatedly as quality control. The obtained accuracy was better than 9.8 % for trace elements, with the exception of Cu (18.9 %). For the REEs, an accuracy better than 5.2 % was attained. The analytical precisions achieved by repeated measurements on BCR-2 for trace elements and REEs were better than 2.4 %.

3 Results

Affiliation to two distinct lithostratigraphical units – Langevåg Group and Geitung Unit – and macroscopic similarities allow grouping of the sampling locations into Group A (Location 1, 4, 5), **bedded radiolarian chert**, and Group B (Location 2, 3), **jasper**. Table 3.1 (page 57) gives an overview of sample traits.

3.1 Mineralogy and textures

3.1.1 Group A

The samples from Location 1 (Langevåg), 4 (Sagvåg, by the mine), and 5 (Sagvåg, on the coast) do not only belong to the same lithostratigraphical unit, but also show very similar traits regarding mineralogy and associated textures. Samples of Group A all consist of mostly microcrystalline quartz, whereas hematite, mica, and carbonate comprise minor mineral phases. Parallel layering can be observed both macroscopically and microscopically, although deformation led to folding of the layers, to a greater or lesser extent in different samples (Figure 3.1). Quartz veins cross-cut the layering. This is very obvious in Figures 3.1c and 3.1d. Reddish-grey layers of chert are interbedded with thinner, grey layers of sediments in the outcrop, but only the red chert layers were the focus in this study.

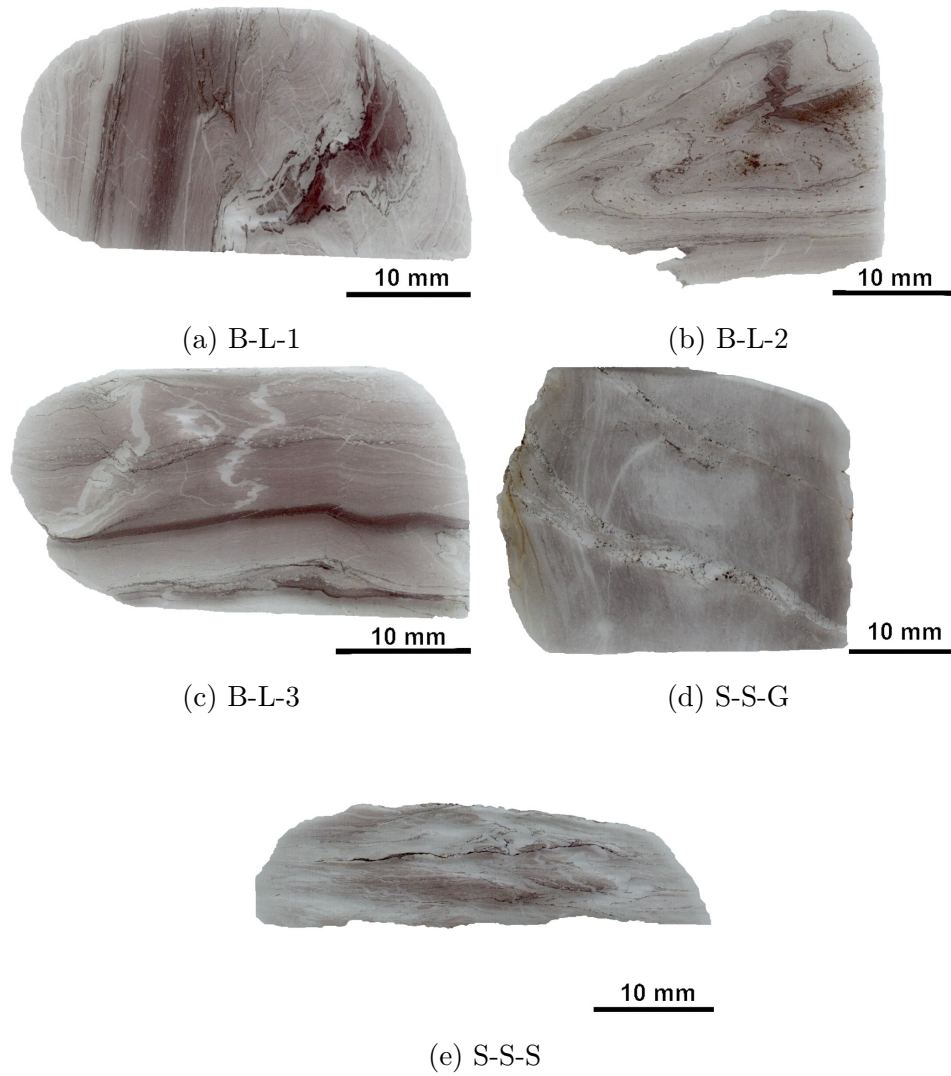
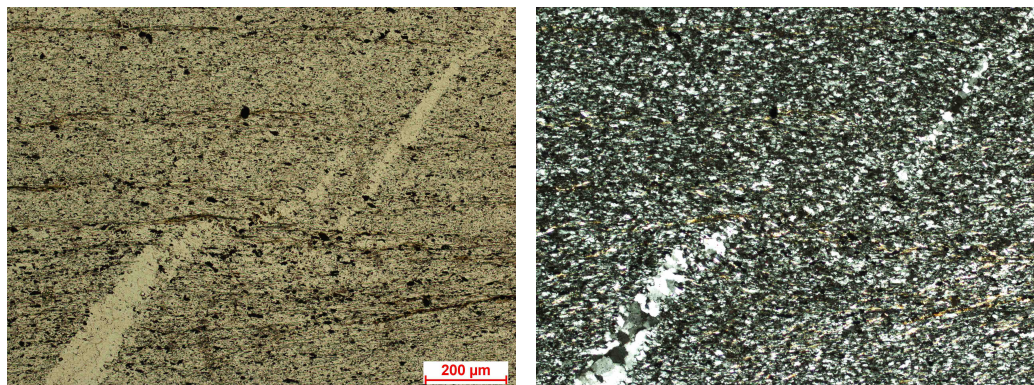


Figure 3.1: Scans of thin sections of samples belonging to Group A, using reflected light

Microcrystalline quartz constitutes the groundmass of the rock (Figure 3.2). Varying hematite crystal abundance is evident and occurs both gradually and abruptly. These concentration differences indicate the layering within the chert, with a variable layer thickness within samples.



(a) Transmitted light, B-L-2

(b) Polarised light, B-L-2

Figure 3.2: Layered microcrystalline quartz groundmass with cross-cutting quartz vein showing bigger quartz crystals than groundmass, Group A

Hematite occurs both as xenomorphic round and angular crystals. They show a reddish-brown colour in transmitted light and darker reddish-brown colour in cross-polarised light (Figure 3.3). In layers mostly consisting of microcrystalline quartz, mainly round, small hematite crystals ($<1\ \mu\text{m}$ to $3\ \mu\text{m}$) are present and are evenly spread, not creating any specific patterns, except for occasional wavy layers several hematite crystals thick (Figures 3.3a and 3.3b). This is also true for the quartz veins. They contain only a very small fraction of the hematite present in the samples. Layers comprising medium to high amounts of hematite show a slightly bigger crystal size of $1\ \mu\text{m}$ to $5\ \mu\text{m}$ (Figure 3.3c). In zones or layers with a very high abundance of hematite, a spotty, cloudy appearance of the latter can be observed, likely caused by the varying size of the hematite crystals ($<1\ \mu\text{m}$ to $10\ \mu\text{m}$) surrounded by microcrystalline quartz (Figure 3.3d). Within these layers, or zones, certain

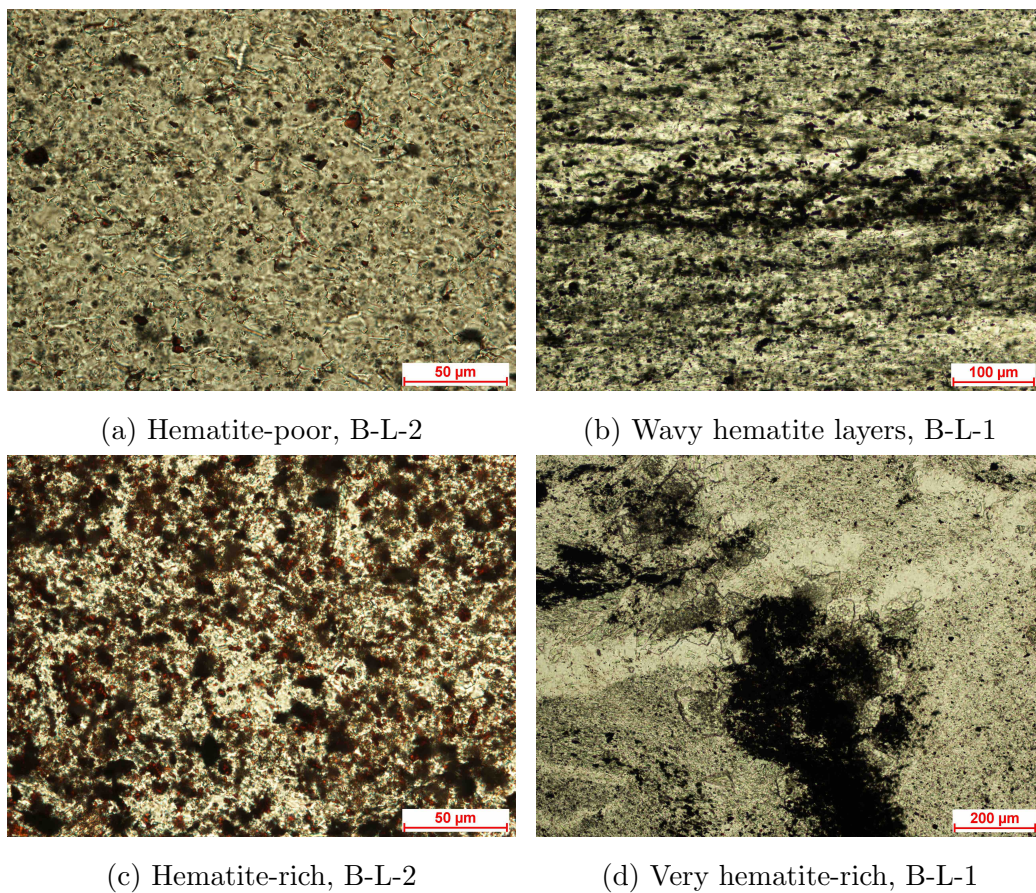


Figure 3.3: Different types of hematite abundances in Group A samples

structures are rare, but present. They exhibit both wavy and straight appearances and have an average length of up to $350\ \mu\text{m}$ and a thickness of $5\ \mu\text{m}$ to $20\ \mu\text{m}$ (Figures 3.4a and 3.4b). In most cases they follow the general layering, implicating that they constitute the layering itself as single crystals. But some can be seen in B-L-3, appearing to be angled in regard to the layering; they resemble filaments. Using optical microscopy, the small crystal size makes it difficult to see whether crystals constituting these structures are connected or separated from each other. The SEM was employed to investigate these structures further. Using BSE and SE detectors, single

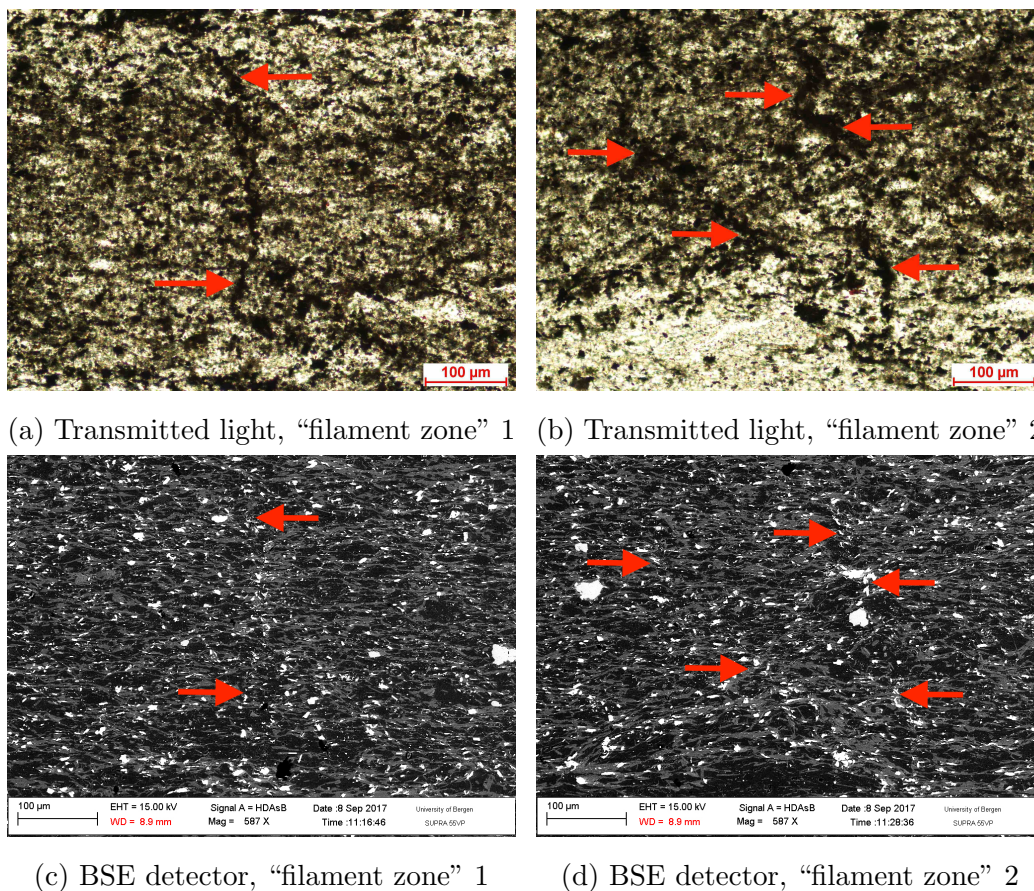


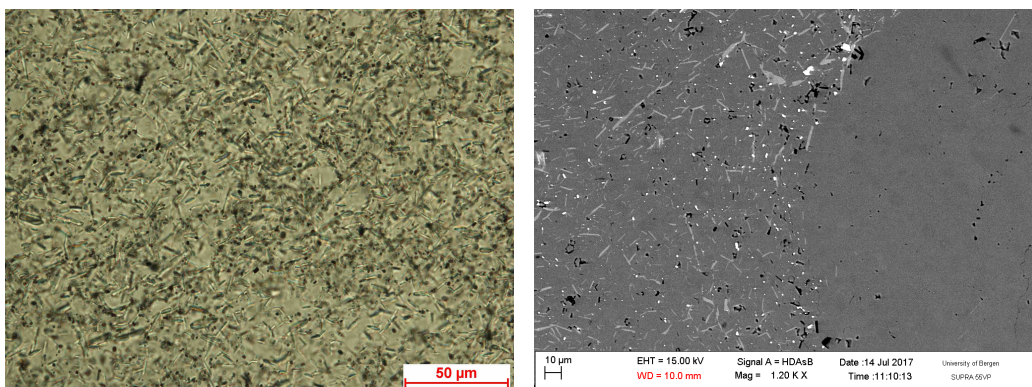
Figure 3.4: Filament-resembling structures in B-L-3

crystals loosely following wavy lines were found, exhibiting a higher density along these lines than around (Figures 3.4c and 3.4d).

Thin sections of Group A all contain small, needle-like mica crystals of $3\ \mu\text{m}$ to $15\ \mu\text{m}$ length and $0.5\ \mu\text{m}$ to $2\ \mu\text{m}$ thickness (Figures 3.5a and 3.5b). Under transmitted light, they appear transparent to slightly greenish. They are evenly distributed within the quartz-rich layers, less present but also evenly distributed within more hematite-rich layers, and non-existent in the quartz veins (Figure 3.5b). Their orientation only loosely follows the layering, and sometimes does not at all. Based on optical properties, the mica

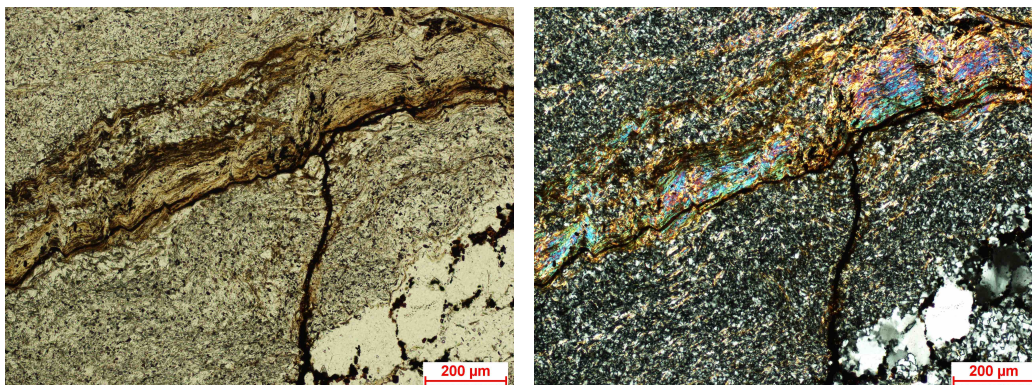
is assumed to be of muscovite composition. Mica also appears as bigger crystals in the thin sections, a good example being S-S-G (Figures 3.5c and 3.5d). Here, mica comprises a slightly folded layer within the microcrystalline quartz groundmass. Perfectly following the layering, a crack filled with dark brown iron oxides can be observed. Different shades of transparent to brown colours of the mica crystals are present, interpreted to having been caused by subsequent precipitation of iron oxides. Raman spectroscopy showed that the mica present in S-S-G is muscovite, supported by SEM/EDS analysis, providing information about incorporated traces of Mg and Fe as well. Locally in B-L-1, Na-rich mica crystals lacking K were identified with SEM/EDS analysis.

An important trait samples of Group A share, is the presence of quartz in round to elongated spheres, present in distinct layers and visible with the bare eye within the thin sections (Figure 3.1). They have diameters of 100 μm to 300 μm and are embedded in microcrystalline quartz layers with hematite crystals (Figures 3.6a to 3.6d). Occasionally they occur in mica-rich layers, where the mica crystals wrap around them, also indicating a secondary crystallisation of the mica (Figures 3.6e and 3.6f). The spheres contain very few hematite crystals with sizes of $<1 \mu\text{m}$, and significantly less mica needles than the surrounding microcrystalline quartz. The size of the quartz crystals comprising these spheres is bigger than of the microcrystalline quartz around, between 5 and 30 μm , compared to 1 μm to 5 μm (Figure 3.6d). In some samples, the spheres are elongated, likely reflecting the degree of deformation the samples were exposed to (compare Figures 3.6a and 3.6b). According to Brekke et al. (1984), samples from Location 1 (Langevåg) are bedded radiolarian chert. These quartz spheres are interpreted to stem from radiolaria, a silica-shell-producing organism present in the oceans since the Cambrian. They thrive under certain conditions and when dying en masse, lead to the deposition of a radiolarian “ooze”, which during diagenesis crys-



(a) Mica needles within microcrystalline quartz, evenly spread

(b) Mica needles within quartz (left), mica-free quartz vein (right)



(c) Mica crystals

(d) Mica crystals under polarised light

Figure 3.5: Mica in S-S-G, Group A

tallises from biogenic opal to quartz. Their spherical shells generally have diameters of 100 to 200 μm (Smalley, 1963), which corresponds with the sizes of the quartz spheres found in the samples. Samples from Location 4 and 5 (Sagvåg) are associated with the Langevåg Group and their mineralogical and textural appearance strongly resembles the Location 1 samples, leading to the assumption that all samples of Group A are bedded radiolarian chert, due to the omnipresent occurrence of the quartz spheres interpreted to be radiolarian shell remnants.

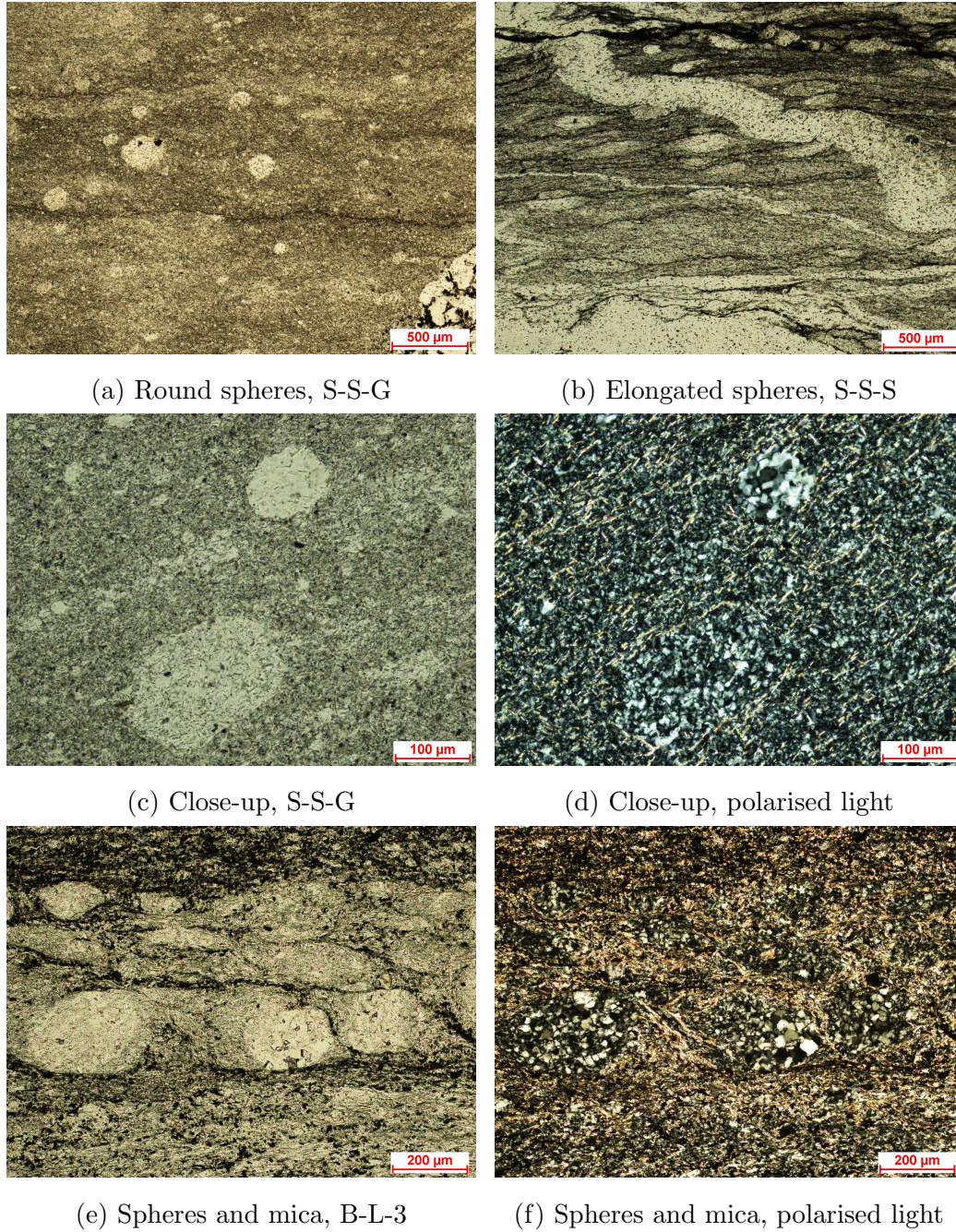
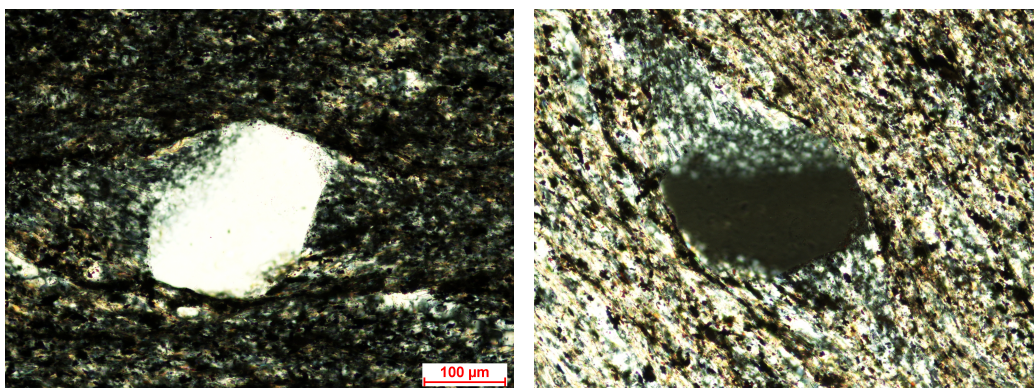


Figure 3.6: Quartz sphere abundances in various samples of Group A

Carbonate crystals with mostly idiomorphic shapes and sizes of 20 μm to 200 μm are present within the microcrystalline quartz groundmass in samples of Group A. They are not evenly spread within the samples (Figure 3.8a). The amount of carbonate between samples differs as well. In discordant quartz veins, xenomorphic and very small (2 μm to 10 μm) idiomorphic carbonate crystals are present, but not abundant (Figure 3.8b). All crystals show degrees of mineral replacement reactions taking place, to a lesser or greater extent in separate samples. Idiomorphic carbonate crystals in all samples, except for B-L-2, exhibit a slight, partial replacement of carbonate with quartz (Figures 3.8c and 3.8d) as well as Fe oxide precipitates in the vicinity of cracks. In contrast, B-L-2 shows idiomorphic carbonate habits featuring both holes within, rimmed with Fe oxide precipitates (Figures 3.8e and 3.8f), and crystals almost completely replaced with Fe oxides. Using EDS connected to the SEM, point analyses revealed that not only quartz and Fe oxides are present as replacement products, but also Mn oxides and fluorapatites with crystal sizes $<1 \mu\text{m}$.

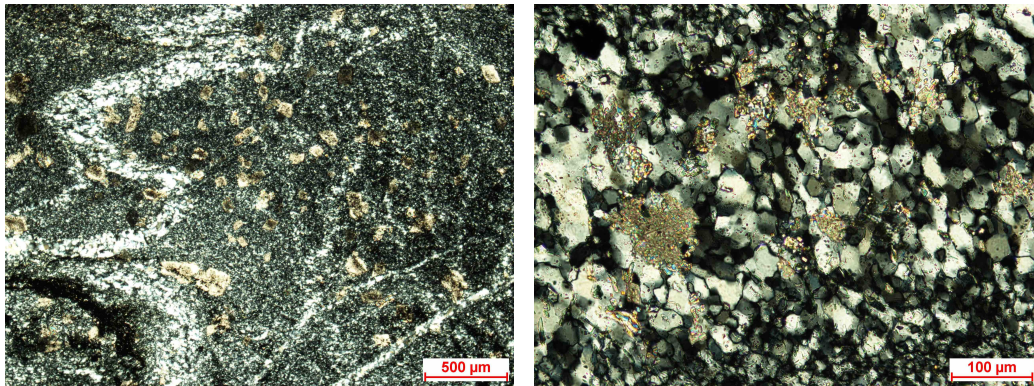
One last notable finding (in B-L-1) is a quartz grain, embedded in microcrystalline quartz (Figure 3.7), interpreted to be terrigenous detritus.



(a) Quartz grain, polarised light

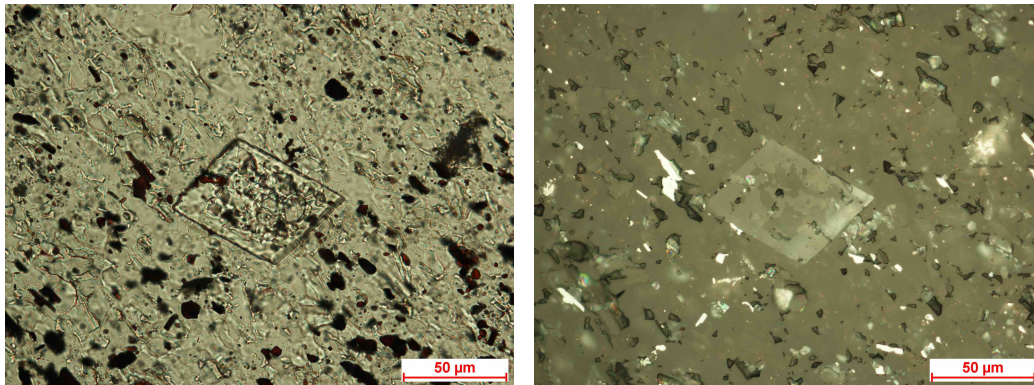
(b) Polarised light, different angle

Figure 3.7: Quartz grain in B-L-1, Group A



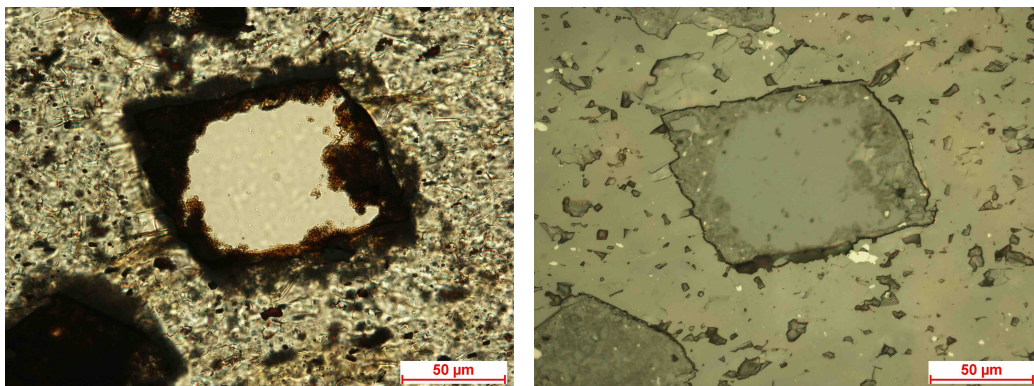
(a) Idiomorphic carbonate, B-L-1

(b) Xenomorphic carbonate, B-L-3



(c) Carbonate with quartz centre, B-L-1

(d) Carbonate, reflected light



(e) Partial Fe-oxide filling, B-L-2

(f) Partial filling, reflected light

Figure 3.8: Carbonate crystals in various samples of Group A

3.1.2 Group B

The samples from Location 2 (Geitung) and 3 (Finnås) both belong to the Geitung Unit, and – with one exception from Location 2 – exhibit identical traits regarding mineralogy and textures, see Figure 3.9. This exception is B-G-1 (Figure 3.9a), taken from a hematitic chert band. Due to similarities in mineralogy and affiliation with the same lithostratigraphical unit, B-G-1 is included here, but described separately.

Generally, samples from Group B consist mainly of microcrystalline quartz with sizes of 10 μm to 30 μm and locally bigger grains up to 100 μm ; magnetite, hematite, and carbonate (\pm chlorite, \pm mica) are the minor mineral phases present. No folding or clearly defined layering can be observed (Figures 3.9b to 3.9d), except for in B-G-1 (Figure 3.9a) and B-F-1 (Figure 3.9d). The layering in B-G-1 resembles Group A, whereas it is thicker in B-F-1.

Magnetite in Group B samples is present as idiomorphic to hypidiomorphic crystals with sizes of mainly between 10 μm to 50 μm . A few crystals are smaller and a small number of magnetites reaches sizes of up to 300 μm (Figure 3.10a). When using reflected light, it becomes obvious that some of the magnetite crystals contain quartz inclusions and nearly all are partly fractured internally (Figure 3.10b). Some magnetites close to fractures in the rock exhibit a recrystallisation from magnetite to another Fe oxide (Figure 3.10c), possibly due to fluids percolating into the rocks long after deposition and diagenesis. The distribution of magnetite throughout the thin sections is related to the abundance of hematite. Magnetite is present in the microcrystalline quartz-rich areas, containing nearly no hematite, and hematite is concentrated in zones containing next to no magnetite crystals (Figure 3.10d). Patches of magnetite-poor/hematite-rich and magnetite-rich/hematite-poor zones show both gradual and very abrupt boundaries, not exhibiting general symmetry in their occurrence.

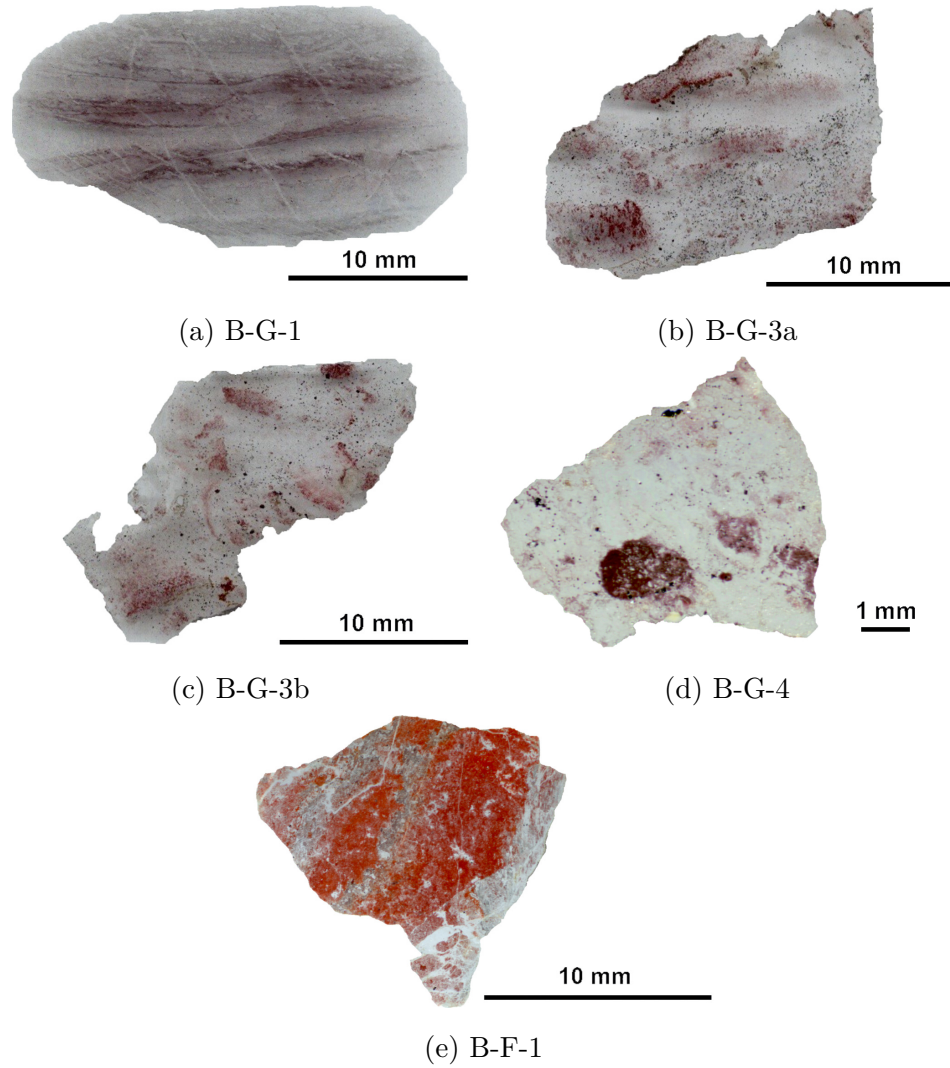
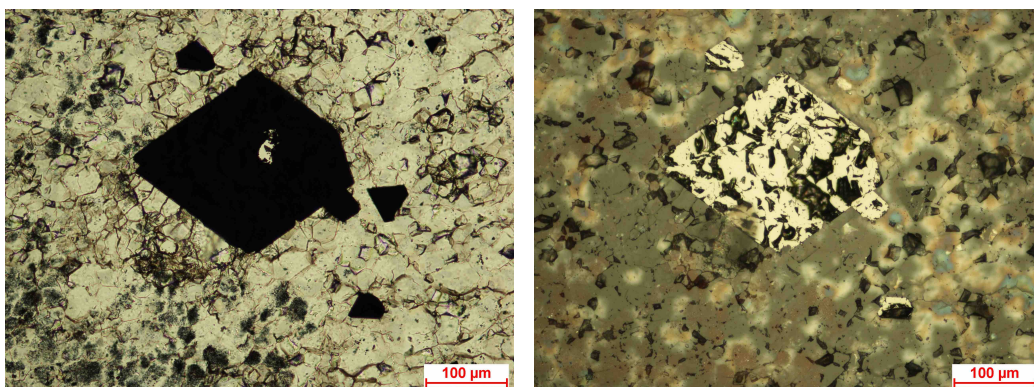
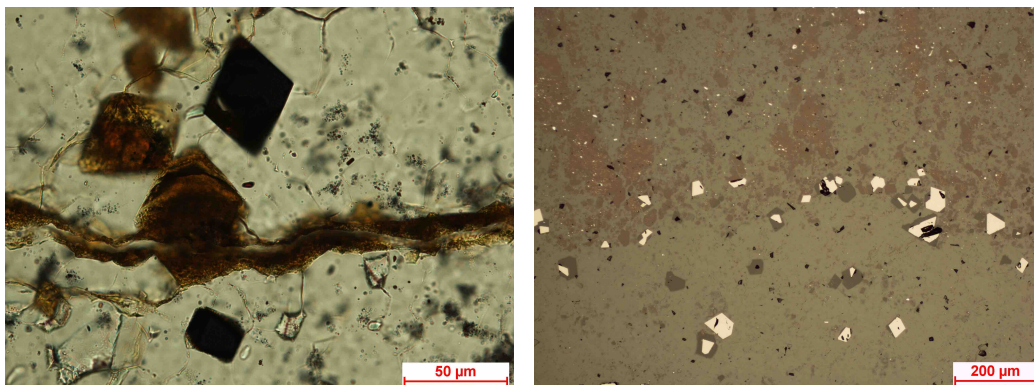


Figure 3.9: Scans of thin sections of samples belonging to Group B, using reflected light



(a) Idiomorphic crystal in between microcrystalline quartz

(b) Quartz inclusion and fractures, reflected light



(c) Recrystallised Fe oxide close to Fe-oxide filled crack

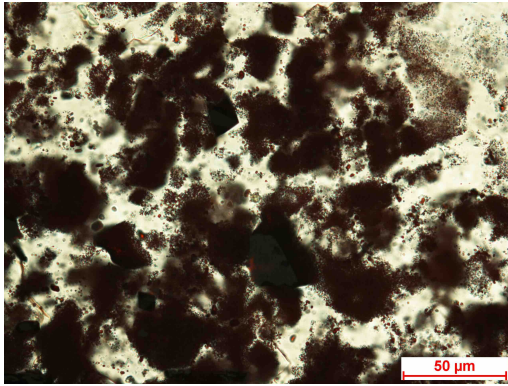
(d) Magnetite-poor (top), Magnetite-rich (bottom), reflected light

Figure 3.10: Magnetite crystals in various samples of Group B

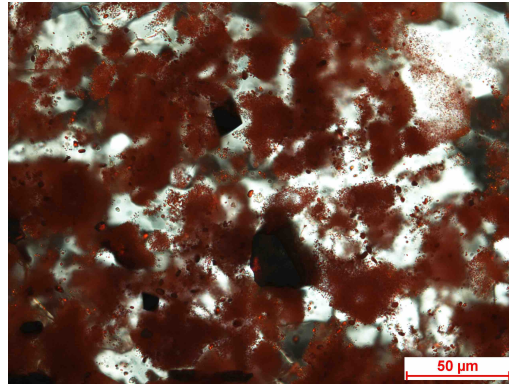
Hematite shows several different shapes in Group B samples (Figures 3.11 and 3.12). It is mainly present as round inclusions of sizes $<1\ \mu\text{m}$, leading to a type of hematite occurrence called “hematite microspherules” or “dusty hematite”, see Figures 3.11a and 3.11b. The microspherules are not evenly spread, but form clusters of polygonal patches creating a mosaic texture (Figures 3.11c and 3.11d). These polygonal patches consist of hematite mi-

rospherules embedded in quartz and have sizes of roughly 10 μm to 80 μm , with nearly hematite-free quartz rims surrounding them, showing a thickness of 5 μm to 20 μm . The internal texture of single clusters of polygonal patches varies with concentration of hematite, which seems to be related to the external shape of the cluster. Round and oval zones are present, exhibiting a near-concentric decrease from the hematite-rich outer areas to the hematite-poor inner areas (Figure 3.11c). Other shapes include angular clusters with an unidirectional change in hematite content (Figure 3.11d). Not all clusters featuring the polygonal texture display a directional variation in hematite microspherule abundance. Some show no clear pattern and vary in hematite abundance seemingly randomly, creating patches of high and low concentrations within clearly defined zones. In B-F-1, these clusters are present, but not nearly as distinctly expressed as in the other samples. Another form that the hematites display are round and angular crystals with sizes of 10 μm to 40 μm , occurring independently from the hematite microspherules and less frequently (Figure 3.11e). Generally, where single, bigger hematites are present, microspherules do not occur directly next to it, but appear within a little distance. Sometimes a zone of pure quartz as a “ring” is present around it, varying with the size of the hematite in the centre (Figure 3.11f). In other areas, the bigger hematites appear grouped together, independent of the microspherules.

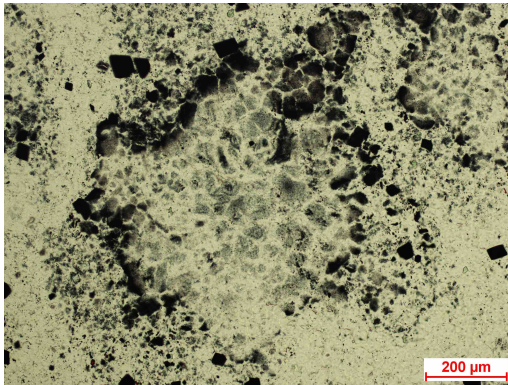
This is a trait B-F-1 exhibits the strongest; generally more hematite crystals with sizes of 2 μm to 5 μm are present in high concentrations and with less easily distinguishable shapes. This sample displays a higher amount of hematite than the other samples of both Group A and B, macroscopically seen. The appearance of zones containing hematite resembles the zones of high hematite abundance in Group A samples, creating a spotty, cloudy presence in the macroscopically dark red zones. It is difficult to distinguish grain boundaries between single hematite crystals. They appear intertwined



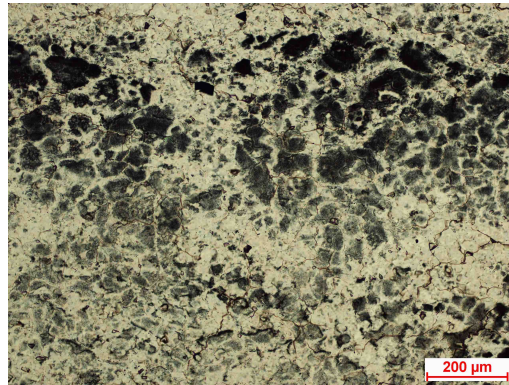
(a) Microspherules under transmitted light, B-G-3b



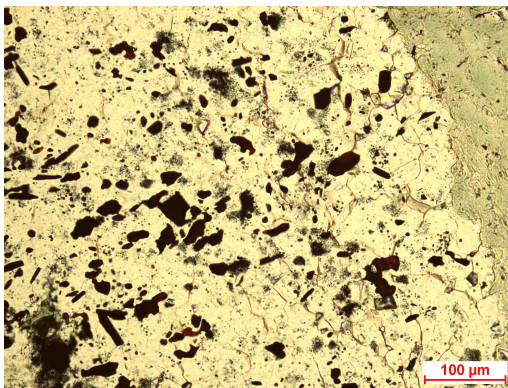
(b) Microspherules under reflected light, B-G-3b



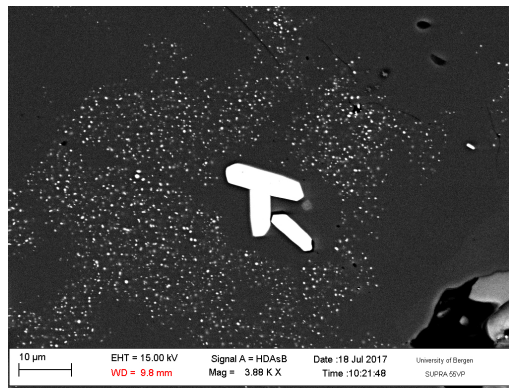
(c) Polygonal clusters, hematite concentration decreases inwards, B-G-3a



(d) Polygonal clusters, hematite concentration varies unidirectionally, B-G-3b



(e) Large, single round and angular crystals, B-G-3a



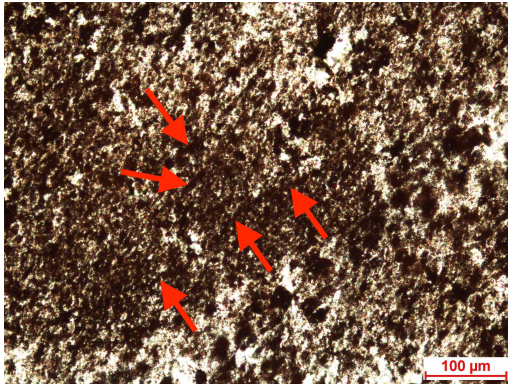
(f) Larger crystals surrounded by microspherules, B-G-3a

Figure 3.11: Hematite occurrence in various samples of Group B

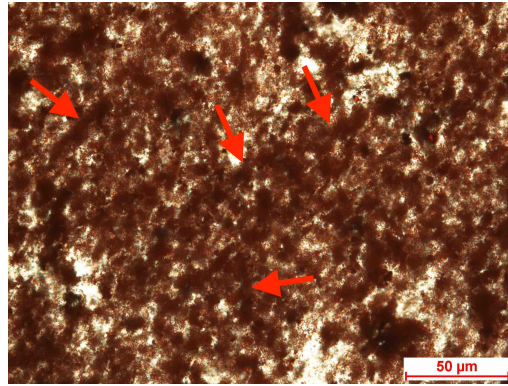
and and fuzzy. SEM imagery provides insight here and shows that for all Group B samples, the hematite grains show the same crystal habit. Within the intertwined, mesh-like crystal aggregates, certain structures can be found throughout the dark red zones in B-F-1 (Figure 3.12). They resemble the filament-like structures seen in a hematite-rich zone within B-L-3 (Group A). Their look is mainly straight, a weak undulating pattern can occasionally be observed (Figures 3.12a to 3.12c), although single structures with a stronger undulating appearance were detected (Figure 3.12d). The average length is 30 μm to 100 μm and the thickness varies between 5 μm to 10 μm . In some zones, slightly smaller and thinner strands can be seen, with lengths of 10 μm to 20 μm and thicknesses of 2 μm to 4 μm (Figure 3.12c, darker arrows). The SEM showed no connected, filament-representing structures, only single hematite crystals clustered together, and generally seemingly following a “line” (Figures 3.12e and 3.12f). This can be interpreted to depict the structures observed with optical microscopy (Figures 3.12a to 3.12d).

To distinguish between magnetite and hematite can be complicated in general, but due to the two very distinct mineral habits displayed in the samples of both Group A and B, the differentiation between magnetite and hematite is based on optical properties, including colour and crystal shape. Reinforcement for this distinction is provided by Raman spectroscopy. Different magnetite crystals and hematite crystals have been investigated and the Raman spectra are unambiguous: The black, anisotropic, hexoctahedral crystals present in Group B line up with the database entry for magnetite (Figure 3.13a), whereas the brown-reddish, xenomorphic crystals present in both Group A and B match the Raman spectrum for hematite in the database (Figure 3.13b).

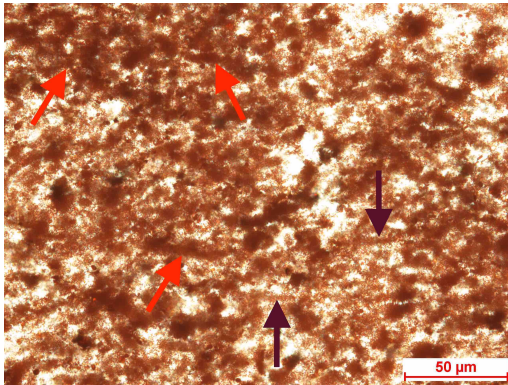
Carbonate crystals only comprise a minor component in Group B samples. They occur as idiomorphic to hypidiomorphic crystals with varying sizes and degrees of mineral replacement with quartz (Figure 3.14). SEM/EDS hints



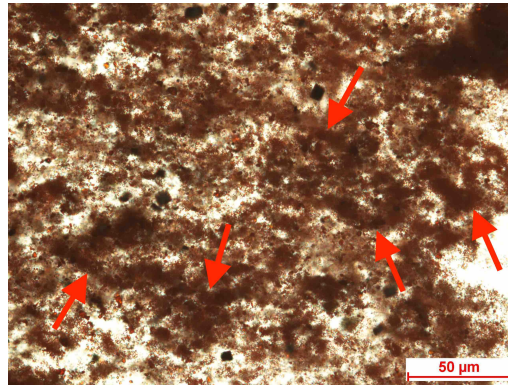
(a) Straight filamentous structures, position indicated with arrows



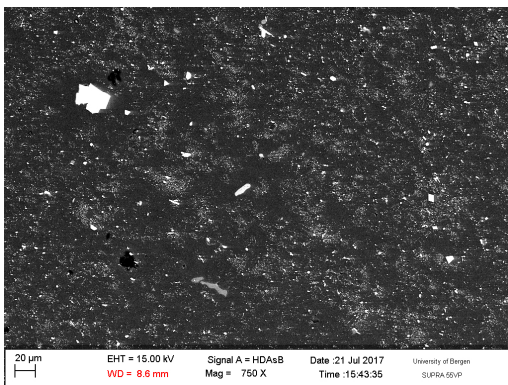
(b) Filamentous structures from (a) closer up



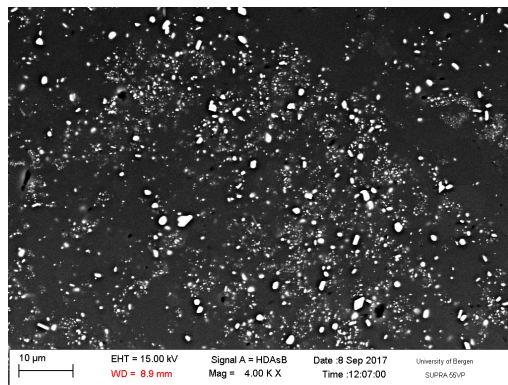
(c) Various thicknesses



(d) Undulating filamentous structures

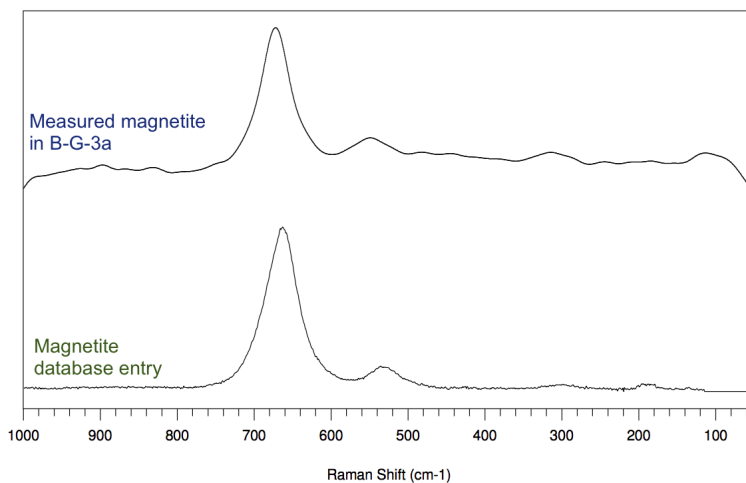


(e) BSE image, hematite-rich zone

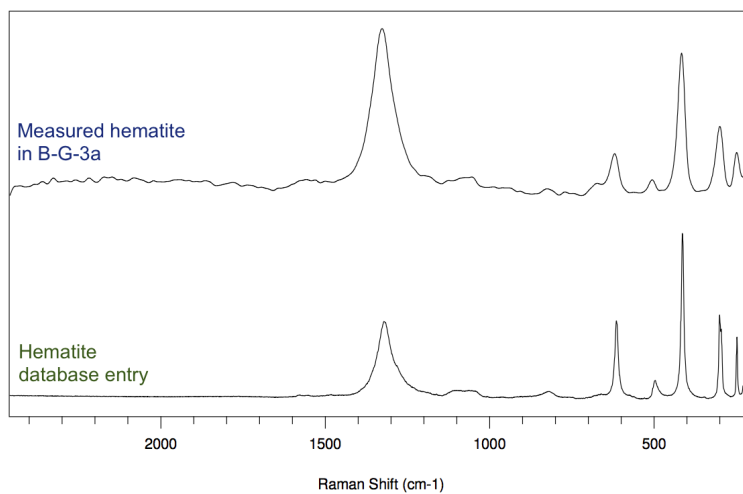


(f) BSE image, hematite-rich zone

Figure 3.12: Filament-shaped structures of hematite in B-F-1, Group B

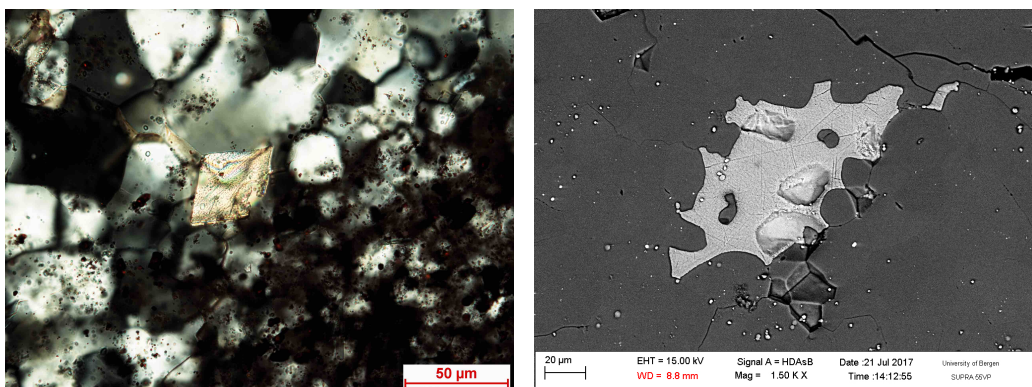


(a) Measured representative magnetite (top) and the matching database entry for magnetite (bottom)



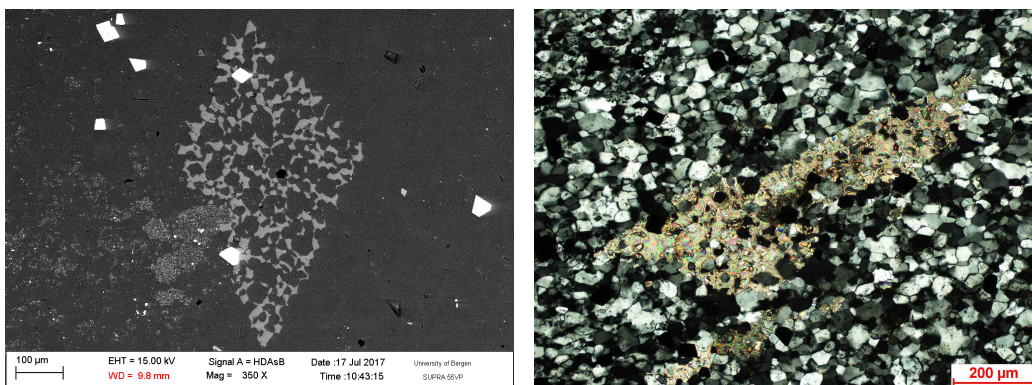
(b) Measured representative hematite (top) and the matching database entry for hematite (bottom)

Figure 3.13: Raman spectra of representative magnetite and hematite crystals in B-G-3a, compared to database entries for magnetite and hematite, Database library: minlabv5.lib



(a) Intact, idiomorphic carbonate, polarised light, B-G-4

(b) Holes and replacement by quartz, SEM, B-G-4



(c) Extensive replacement by quartz, idiomorphic shape preserved, B-G-3a

(d) Extensive replacement by quartz, polarised light, B-G-3b

Figure 3.14: Carbonate crystals in various samples of Group B

towards carbonates in Group B mainly being calcite, containing Mn traces.

Within the jasper clast samples from Location 2, hypidiomorphic to xenomorphic chlorite crystals occur (Figure 3.15). Sizes vary significantly (Figures 3.15a to 3.15d). They all show a very light green colour, occasionally pleochroism to light brown in transmitted light, and grey interference colours under polarised light. Implementing Raman spectroscopy to identify the chemistry yielded a weak match with clinocllore (Mg-rich chlorite),

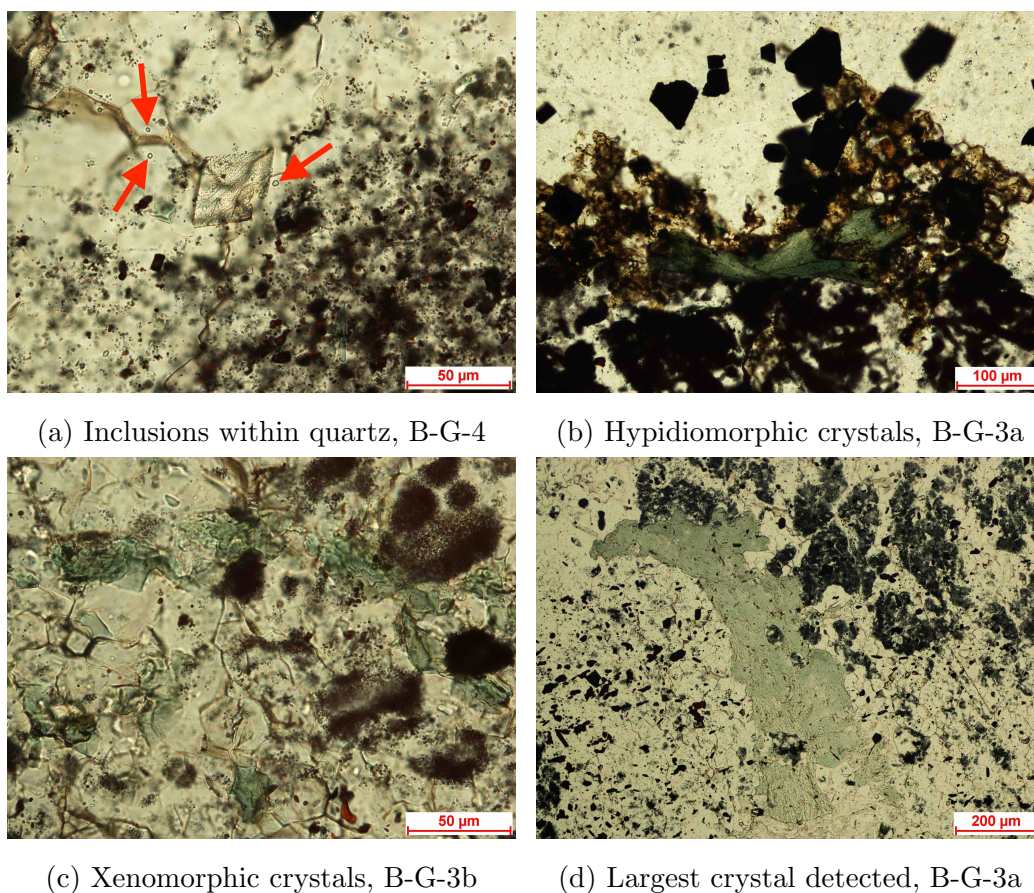
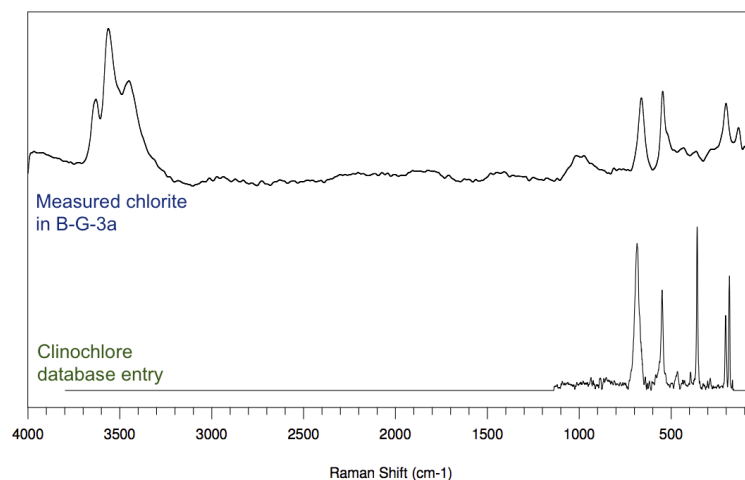


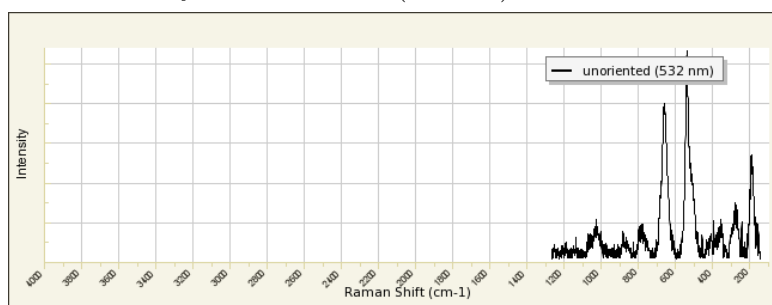
Figure 3.15: Chlorite in various samples of Group B

and a better match with chamosite (Fe^{2+} -rich chlorite, Figure 3.16). This is supported by SEM-EDS analyses. The chlorite crystals contain both Fe and traces of Mg, leading to the assumption that they are a solid solution between chamosite–clinochlore.

Mica needles, present in Group A, are absent in the Group B samples, with the exception of B-F-1, which contains only very small amounts. However, bigger mica crystals, while observed in Group A, are wholly absent within Group B.



(a) Measured representative chlorite (top) and the matching database entry for clinochlore (bottom)



(b) For comparison: RRUFF database entry for chamosite (R070728)

Figure 3.16: Raman spectrum of chlorite in B-G-3a, compared to database entries for clinochlore and chamosite, Database library: minlabv5.lib, and RRUFF (<http://rruff.info/Chamosite/R070728>)

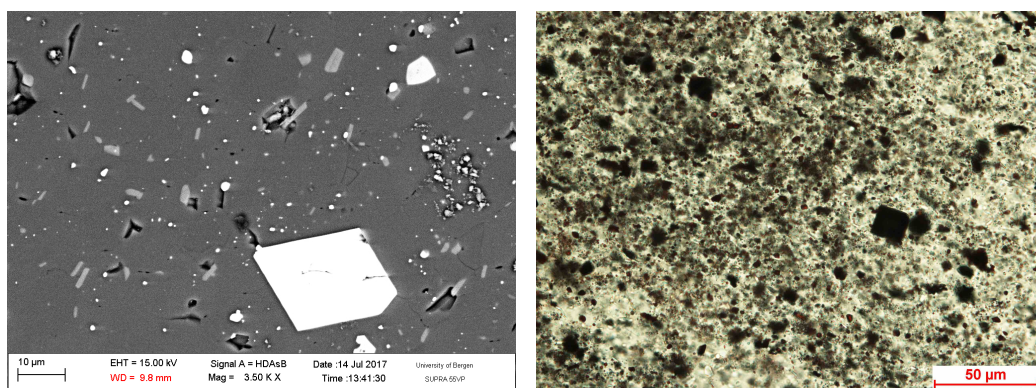
B-G-1

Both macroscopically and microscopically, B-G-1 more resembles the bedded radiolarian cherts comprising Group A, than it resembles Group B samples. However, the presence of magnetite distinguishes it from samples of Group

A, in addition to the affiliation with the same lithostratigraphical unit as the other samples of Group B. The magnetite in B-G-1 shows the same crystal habit as in other Group B samples with slightly smaller crystal sizes, between 2 μm to 30 μm (Figure 3.17a). Its appearance in the thin section, in relation to hematite abundance, corresponds with Group B, as magnetite is more abundant in hematite-poor zones. B-G-1 contains varying concentrations of round, xenomorphic hematite crystals (<1 μm to 10 μm) embedded in a microcrystalline quartz groundmass. Neither distinct polygonal mosaic patterns, nor filament structures can be found in the sample (Figure 3.17b). The hematite abundance resembles Group A in regard to varying concentrations constituting more or less distinct layering (Figure 3.17c). In B-G-1, however, the layering is related to both hematite and magnetite abundance. Where the concentration of magnetite is high, the concentration of hematite is low and vice versa. Macroscopically, the difference between these layers can be seen, the hematite-rich layers exhibit a red to purple colour, while the magnetite-rich layers are more grey. Whereas Group B samples generally do not exhibit mica, small needle-like mica crystals with a length of 3 μm to 5 μm and thickness of 0.5 μm to 1 μm are present in B-G-1 (Figure 3.17a), not following any orientation and resembling the mica needles in Group A samples. However, their abundance is significantly lower. Carbonate crystals in B-G-1 exhibit xenomorphic shapes and mainly act vein-filling (Figure 3.17d). The thickness of “carbonate accompanied by quartz”-veins lies between 25 μm to 100 μm and they are discordant to the general layering of the sample. Quartz-carbonate-filled veins are parallel to each other, implying one stage of vein filling. Carbonate crystals also occur within the rock outside the veins, possibly with an originally idiomorphic shape, but strong mineral replacement with quartz complicates validating this assumption. Some magnetite crystals are affiliated with those veins, exhibiting sizes of up to 50 μm , bigger than within the surrounding quartz groundmass. Besides the layering,

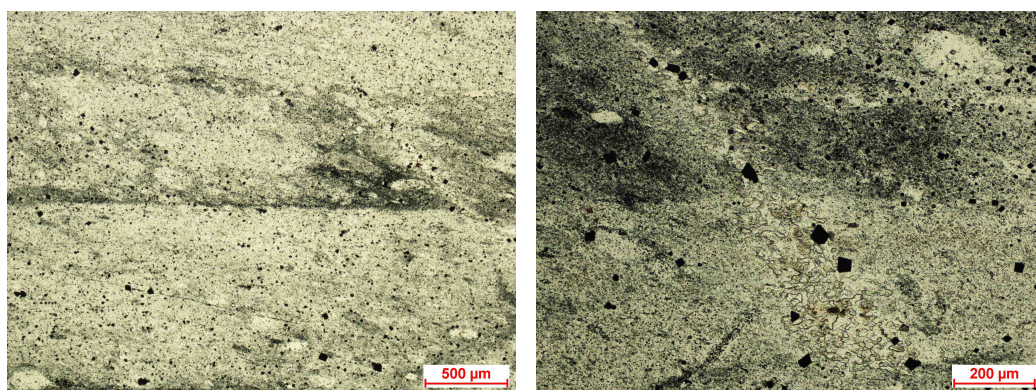
the most important characteristic B-G-1 shares with Group A are round to elongated quartz spheres found in distinct layers, with diameters and quartz grain sizes very much resembling features in Group A, interpreted to be radiolarian shell remnants.

Resemblance with both groups is given, texturally with Group A (layering and radiolarian shell remnants) and mineralogically and lithostratigraphically with Group B (magnetite abundance and Geitung Unit affiliation).



(a) Idiomorphic magnetite and mica needles

(b) Hematite grains constituting a darker layer



(c) Quartz spheres in distinct layers, (d) Cross-cutting carbonate vein associated with varying hematite concentration in layers associated with larger magnetite crystals

Figure 3.17: Various minerals and textures in B-G-1, Group B

Table 3.1: Mineralogical and textural traits of Group A and Group B samples

	B-L-1	B-L-2	B-L-3	S-S-G	S-S-S	B-G-1	B-G-3a	B-G-3b	B-G-4	B-F-1
Microcrystalline quartz, grain size	~10 μm					10 - 30 μm				
Hematite, xenomorphic, round	1 - 10 μm					<1 μm to 10 μm	10 - 40 μm , sparse			2 - 5 μm high concentrations
Hematite microspherules/ dusty hematite	No					No	<1 μm			<1 μm
Mica needles	Present mainly in quartz-rich layers, high abundance					Low abundance	No			Very low abundance
Muscovite	Sparse			Very abundant	Sparse	No				
Na-rich mica	Locally, very sparse	No				No				
Carbonate crystals	High concentrations in certain zones			Few crystals		Xenomorphic vein filling	50 - 200 μm , bigger crystals up to 1000 μm		Most intact, 50 - 200 μm	50 - 200 μm , up to 400 μm
Idiomorphic carbonates, partially replaced	Quartz and Fe oxides	Holes and Fe oxides	Quartz and Fe oxides			Strong replacement (Quartz)			Least replacement	Strong replacement (Quartz)
Idiomorphic magnetite	No					2 - 30 μm	10 to 50 μm			Up to 600 μm
Xenomorphic chlorite	No					No	<1 μm inclusions, and 20 - 1000 μm crystals			No
Clusters of polygonal patches	No					No	Typical hematite abundance			Very sparse
Hematite-rich layers	Defined	Clearly defined		No	Disrupted	Defined	No			
Hematite "filaments"	No		Layering-discordant, 10 μm thickness, up to 350 μm length	No		No				Very abundant, 5 - 10 μm thickness, 30 - 100 μm length
Effect of folding and deformation	Medium	High	Low		High	Low				
Layering affiliated with	Hematite abundance					Hematite and magnetite abundance	No			
Radiolarian shell remnants, diameters of 100 to 300 μm	Slightly elongated		Round to elongated	Most round	Most elongated	Slightly elongated	No			

3.2 Bulk geochemistry

3.2.1 Group A

Major elements

The major element analysis by ICP-OES does not include the measurement of Si, which makes it necessary to calculate the SiO_2 in wt% from the values given for the measured elements. Results of the calculations are depicted in Table 3.4 on page 69. In Group A, the oxides display similar values for all samples. The concentration of SiO_2 ranges between 77.52 to 86.75 wt%. The other relevant oxides are Al_2O_3 , ranging between 6.05 and 10.23 wt%, and Fe_2O_3 with concentrations of 3.42 to 5.78 wt%. Na_2O , MgO , and K_2O only comprise ~ 1 wt% each. Other oxides are present in concentrations lower than 1 wt%. Loss of ignition (LOI) values are very low in all samples, between 0.54 to 1.33 wt%.

Trace elements

Table 3.5 on page 70 provides an overview of the trace element concentrations. The alkali trace elements Li, Rb, and Cs show generally low, but variable concentrations of < 40 ppm for Li and Rb, and ~ 1 ppm for Cs. S concentrations are below the detection limit (130 ppm for a dilution factor of 130). The alkaline earth metal trace elements Sr and Ba are also present with low concentrations (< 40 ppm and < 150 ppm, respectively). The transition metals show a great variation. Ti can be considered both a trace element and a minor element due to differences in concentrations between samples (< 1300 ppm). Other transition metal trace elements are detected with concentrations < 40 ppm, such as V, Cr, Co, Ni, Zn, and Zr. Sc, Y, Nb, and Cu have concentrations below 10 ppm. Hf and Ta exhibit concentrations of

<1 ppm. The post-transition metal Pb displays low concentrations below 10 ppm.

Correlations between element concentrations (major and trace elements) provide important information to infer geochemical traits of samples. Al correlates strongly with Ti (Figure 3.18a), and Ti correlates very well with both Zr and Sc (Figures 3.18b and 3.18c). Mn and Co do not correlate very nicely (Figure 3.18d).

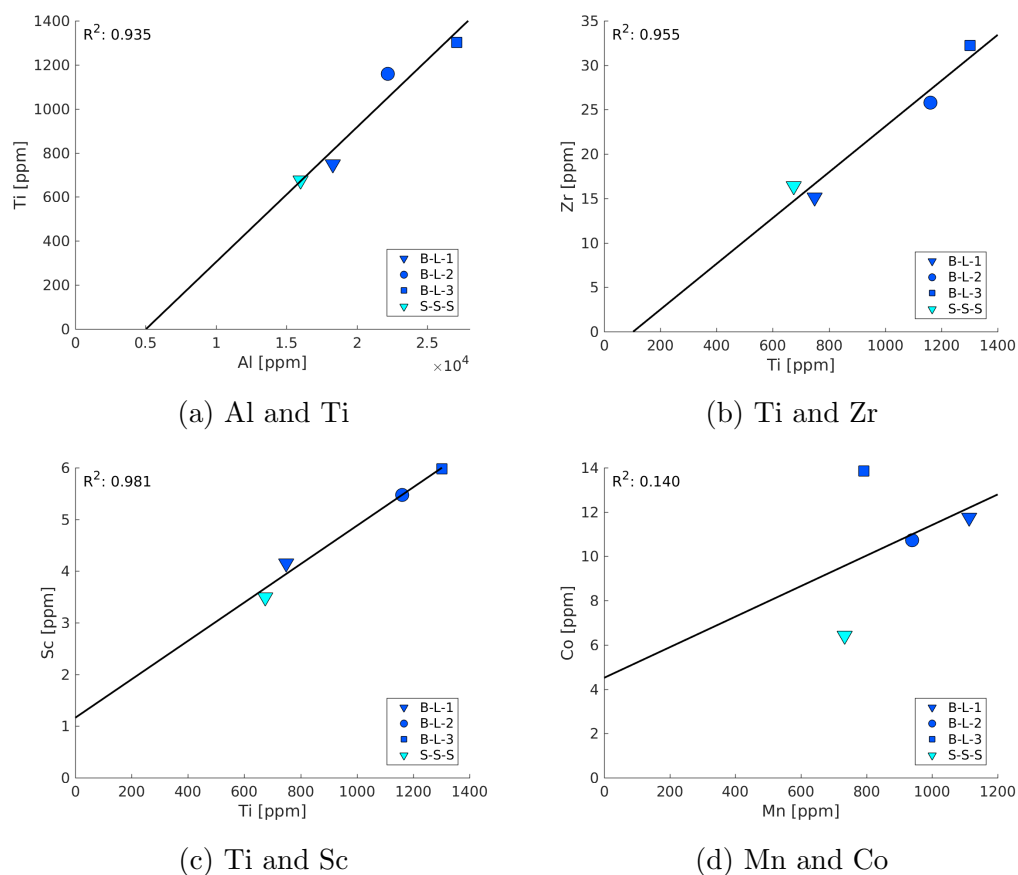


Figure 3.18: Correlations between various major and trace elements for Group A samples

Rare earth elements

Group A samples range in $\sum\text{REE}$ between 30.13 to 66.04 ppm (Table 3.6 on page 71). Three normalisations have been applied to enable comparisons with different sources and to discuss their applicability (see Chapter 4). Calculated $(\text{La}/\text{Yb})_N$ ratios, Ce anomalies, and Eu anomalies for Group A are presented in Table 3.2. The normalisation to chondrite is depicted in Figure 3.19a. The REE patterns are all nearly perfectly parallel to each other, indicating homogeneity in their bulk geochemistry, though the concentrations vary slightly between samples. The $(\text{La}/\text{Yb})_N$ ratio is a measure of Light Rare Earth Element (LREE) over Heavy Rare Earth Element (HREE) abundance and represents the grade of chemical fractionation between LREE and HREE. It is intermediate to high for all samples, varying between 7.4 and 10.4, which can be observed as a slight LREE-enrichment and a subsequent HREE-depletion. Visually, a very small positive Ce anomaly can be observed, backed up by calculated Ce/Ce^* values. The Eu anomaly is more pronounced in the REE-pattern, and calculations exhibit the negative character of it, very uniform at 0.72 - 0.73.

Normalising the REE concentrations to North American Shale Composite (NASC) gives a distinctly different distribution pattern, presented in Figure 3.19b. Regarding homogeneity, the samples all exhibit REE patterns with a high degree of parallelism. $(\text{La}/\text{Yb})_N$ ratios are low and vary in a very narrow range, showing no depletion or enrichment from LREEs to HREEs. Both the Ce and Eu anomalies are only barely visible, backed up by anomaly calculations. Thus, small positive Ce and Eu anomalies are present, Ce/Ce^* not differing vastly from the chondrite normalisation, while the Eu/Eu^* anomaly changes from negative to positive.

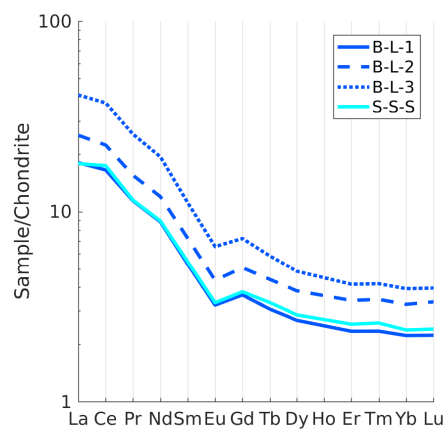
The normalisation to Post-Archean Average Shale (PAAS) is displayed in Figure 3.19c and exhibits similar traits as the NASC-normalisation. $(\text{La}/\text{Yb})_N$

ratios are very low, no depletion from LREEs to HREEs is present, and Ce and Eu anomalies are slightly positive for all samples.

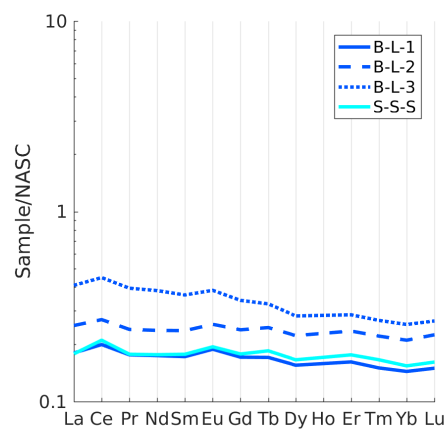
Table 3.2: $(La/Yb)_N$ ratios, Ce/Ce^* , and Eu/Eu^* Group A

Sample ID	$(La/Yb)_N$			Ce/Ce^*			Eu/Eu^*		
	<i>Chondrite</i>	<i>NASC</i>	<i>PAAS</i>	<i>Chondrite</i>	<i>NASC</i>	<i>PAAS</i>	<i>Chondrite</i>	<i>NASC</i>	<i>PAAS</i>
B-L-1	8.1	1.2	0.9	1.15	1.12	1.10	0.73	1.10	1.13
B-L-2	7.5	1.1	0.8	1.13	1.10	1.09	0.72	1.07	1.11
B-L-3	10.4	1.5	1.1	1.15	1.12	1.10	0.73	1.09	1.12
S-S-S	7.4	1.1	0.8	1.22	1.18	1.17	0.73	1.09	1.12

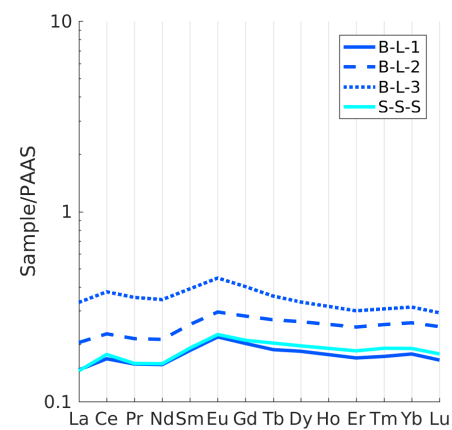
$Ce/Ce^* = Ce_N / (La_N * Pr_N)^{0.5}$, and $Eu/Eu^* = Eu_N / (Sm_N * Gd_N)^{0.5}$, Taylor and McLennan (1985)



(a) Chondrite-normalisation



(b) NASC-normalisation



(c) PAAS-normalisation

Figure 3.19: Different REE-normalisations of Group A samples

3.2.2 Group B

Major elements

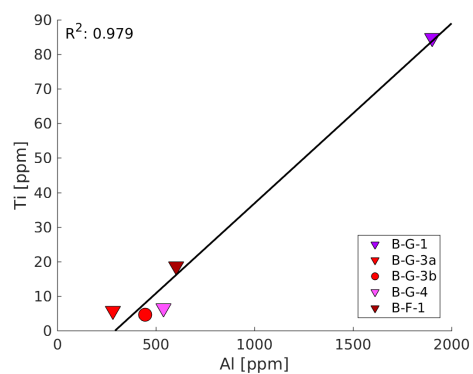
Group B samples feature slightly different and generally lower oxide concentrations compared to Group A (except for SiO_2), but are generally homogeneous for each oxide (Table 3.4 on page 69). The SiO_2 content varies between 75.12 and 93.16 wt%, by far the most abundant oxide in the samples. It is followed by Fe_2O_3 , present in concentrations between 3.49 and 23.38 wt%. B-F-1, the sample exhibiting the most intense red colour (see Section 3.1.2), surprisingly does not have the highest Fe_2O_3 content, but rather B-G-4 does. B-F-1 contains only 14.27 wt%, for comparison. All other oxides, including Al_2O_3 , show concentrations under 1 wt%, with some even below the element-specific detection limits of the ICP-OES. The LOI is very low, between 0.26 and 1.34 wt%.

Trace elements

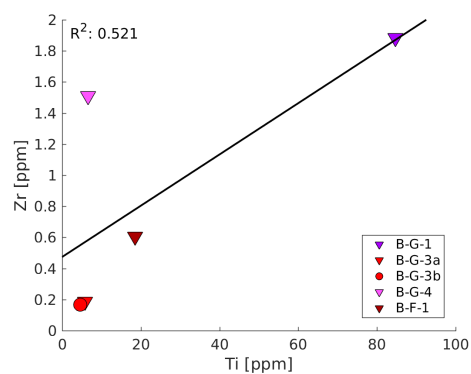
Generally, the concentration of trace elements is lower in Group B than Group A (Table 3.5 on page 70). Homogeneity in concentrations exists mostly between the samples from Location 2, Geitung, with the exception of B-G-1 exhibiting slightly deviating concentrations, along with B-F-1 from Finnås. The alkali trace elements vary somewhat: Cs is only present in concentrations below 0.1 ppm, and Li and Rb have concentrations under 1 ppm with B-G-1 being marginally enriched in both. S concentrations are below the detection limit (130 ppm for a dilution factor of 130). Sr has concentrations of ~ 10 ppm, similar to Ba, with the exception that Ba shows a light enrichment in B-G-1. Transition metal trace elements show a similar divergence as Group A samples regarding concentrations. Sc, Zr, Nb, Hf, and Ta show very low concentrations (< 0.1 ppm, all slightly elevated in B-G-1). Y and Co show somewhat higher concentrations of < 1 ppm, B-F-1 having higher values of

both. Ti, V, Cr, Ni, Cu, and Zn are more enriched in Group B samples (<10 ppm, marginally higher in B-F-1, Ti most enriched in B-G-1 at 85 ppm). The post transition metal Pb is present in lower concentrations than in Group A, with the ICP-MS data being more reliable than the ICP-OES values due to the very low concentrations and discrepancy between the methods. Al, another post-transition metal, is considered a major element in Group A samples, but in Group B the concentrations are considerably lower: B-G-1 is highest with just below 2000 ppm, whereas the rest of the samples contains less than 1000 ppm. The actinides Th and U have concentrations below 0.1 ppm and 0.3 ppm, respectively, with the exception of B-G-1 exhibiting the highest value for U across all samples of Group A and B with 1.53 ppm.

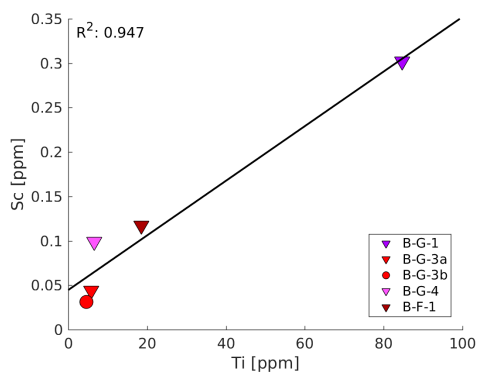
Correlations between major and trace elements show similar behaviour for Group B compared to Group A. Al and Ti correlate strongly (Figure 3.20a). Ti and Zr show a moderate correlation (Figure 3.20b) influenced by B-G-4 exhibiting a slightly higher Zr concentration in regards to Ti than the rest of the samples. And Ti and Sc show a strong correlation (Figure 3.20c). Mn and Co display no correlation (Figure 3.20d), similar to Group A. This is caused by very low concentrations for Co in Group B samples in comparison to Group A samples. Plotting concentrations for Groups A and B together (Figure 3.21) provides a different view: Mn and Co are strongly correlated in all samples, only B-G-1 shows a significant deviation from the trend due to Mn values correlating with Group A samples, but Co values correlating with Group B samples. In the appendix on page 143, correlations for the three remaining element pairs combining Group A and B samples are presented in Figure D.1, displaying strong correlations.



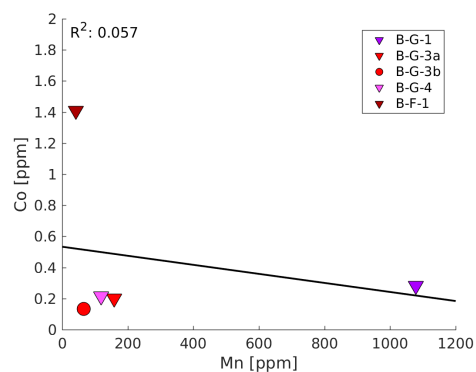
(a) Al and Ti



(b) Ti and Zr



(c) Ti and Sc



(d) Mn and Co

Figure 3.20: Correlations between various major and trace elements for Group B samples; Al, Mn: ICP-OES data; Ti, Zr, Sc, Co: ICP-MS data

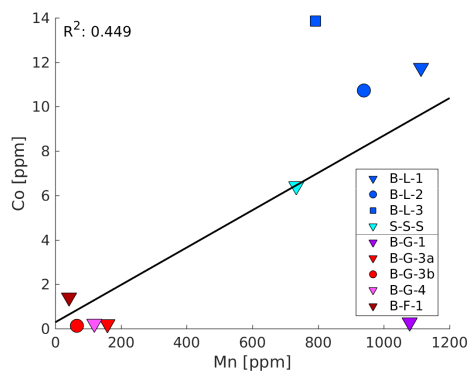


Figure 3.21: Mn and Co correlated for Group A and B samples combined

Rare earth elements

The range of $\sum\text{REE}$ is significantly lower than in Group A samples and is between 1.12 to 3.01 ppm (Table 3.6 on page 71). Figure 3.22 shows the three differently normalised diagrams for Group B samples. $(\text{La}/\text{Yb})_N$ ratios, Ce anomalies, and Eu anomalies for Group B are presented in Table 3.3. Generally, Group B samples show REE distribution trends less homogeneous than Group A, but the concentrations are within a narrow range.

In Figure 3.22a, the chondrite normalisation is displayed. $(\text{La}/\text{Yb})_N$ ratios are 0.6 - 4.5, a slight LREE enrichment and HREE depletion is visible for samples B-G-1 and B-G-3b, whereas B-G-4 exhibits the opposite. The Ce anomalies vary between samples: B-F-1 exhibits a negative anomaly, B-G-1 is only slightly negative, and the rest of Group B is positive. This is different for the Eu anomaly. All samples display a negative character. Another anomaly is visible in Figure 3.22a. The Pr concentration for B-G-4 is significantly lower than expected and yields a negative anomaly, affecting the positivity of the Ce anomaly for B-G-4.

The REE patterns are very different when normalised to NASC, see Figure 3.22b. The ratios of $(\text{La}/\text{Yb})_N$ are very low, presented as general trends

exhibiting HREE enrichment over LREE. Here, the trends for B-G-1 and B-G-3b also differ, due to slightly higher ratios, displaying no significant enrichment or depletion of LREE or HREE. The Ce anomalies exhibit very similar values as the chondrite-normalised values. The Eu anomalies on the other hand, differ vastly from the chondrite normalisation. Normalised to NASC, only three out of five samples exhibit a negative Eu anomaly (B-G-3a, B-G-3b, B-G-4), whereas B-G-1 and B-F-1 show positive Eu anomalies. The Pr anomaly in B-G-4 is negative and for the other samples less pronounced to non-existent.

The PAAS-normalisation yields similar results as the normalisation to NASC. $(La/Yb)_N$ ratios are low, a trend showing enrichment of HREE over LREE is present for three out of five samples, and B-G-1 and B-G-3b exhibit no significant enrichment or depletion trend again. The Ce anomalies are comparable as well, the most negative being evident in B-F-1. Eu displays negative anomalies for B-G-3a, B-G-3b, and B-G-4, but positive anomalies for B-F-1 and B-G-1. This is in accordance with the NASC normalised values. Also, the Pr anomaly resembles the NASC normalisation strongly.

Table 3.3: $(La/Yb)_N$ ratios, Ce/Ce^* , and Eu/Eu^* Group B

Sample ID	$(La/Yb)_N$			Ce/Ce^*			Eu/Eu^*		
	<i>Chondrite</i>	<i>NASC</i>	<i>PAAS</i>	<i>Chondrite</i>	<i>NASC</i>	<i>PAAS</i>	<i>Chondrite</i>	<i>NASC</i>	<i>PAAS</i>
B-G-1	4.2	0.6	0.5	0.98	0.95	0.94	0.76	1.14	1.17
B-G-3a	1.2	0.2	0.1	1.14	1.10	1.09	0.49	0.73	0.75
B-G-3b	4.5	0.7	0.5	1.04	1.02	1.00	0.46	0.68	0.70
B-G-4	0.6	0.1	0.1	1.26	1.22	1.21	0.46	0.68	0.70
B-F-1	2.1	0.3	0.2	0.75	0.73	0.72	0.68	1.02	1.04

$Ce/Ce^* = Ce_N / (La_N * Pr_N)^{0.5}$, and $Eu/Eu^* = Eu_N / (Sm_N * Gd_N)^{0.5}$, Taylor and McLennan (1985)

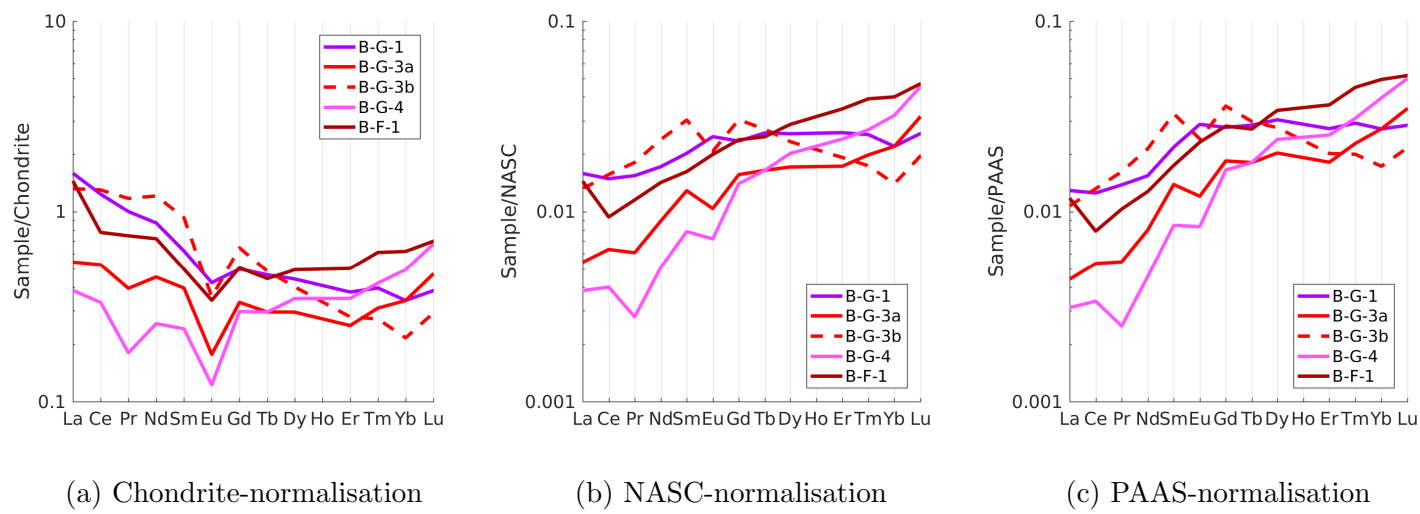


Figure 3.22: Different REE-normalisations of Group B samples

Table 3.4: Major element concentrations (in wt%), measured with ICP-OES

	B-L-1	B-L-2	B-L-3	S-S-S	B-G-1	B-G-3a	B-G-3b	B-G-4	B-F-1
LOI %	1.33	0.79	1.33	0.54	1.31	1.34	0.26	0.77	0.27
NaO ₂	1.14	1.56	1.92	1.09	bdl	bdl	bdl	bdl	bdl
MgO	1.12	0.78	1.02	0.52	bdl	bdl	bdl	bdl	0.07
Al ₂ O ₃	6.92	8.39	10.23	6.05	0.72	0.11	0.17	0.20	0.23
P ₂ O ₅	0.04	0.06	0.07	0.04	0.01	0.01	0.03	0.01	0.12
K ₂ O	0.98	1.44	1.68	1.19	0.25	bdl	bdl	0.05	bdl
CaO	0.16	0.17	0.14	0.20	0.91	1.05	0.38	0.46	0.44
TiO ₂ [†]	0.12	0.19	0.22	0.11	0.01	< 0.01	< 0.01	< 0.01	< 0.01
Fe ₂ O ₃	3.89	4.99	5.78	3.42	3.49	9.72	6.92	23.38	14.27
MnO	0.14	0.12	0.10	0.09	0.14	0.02	0.01	0.02	0.01
Σ	15.85	18.48	22.46	13.25	6.84	12.24	7.77	24.88	15.40
Calculated SiO ₂	84.15	81.51	77.52	86.75	93.16	87.76	92.23	75.12	84.60

bdl = below detection limit, [†] = ICP-MS data used

Table 3.5: Trace element concentrations of Group A and Group B samples (in ppm), measured with both ICP-OES and ICP-MS

	B-L-1	B-L-2	B-L-3	S-S-S	B-G-1	B-G-3a	B-G-3b	B-G-4	B-F-1
Li*	24.33	19.73	25.45	9.60	1.08	0.47	0.39	0.39	0.87
B*	7.02	10.52	13.06	bdl	bdl	bdl	bdl	bdl	8.12
S*	bdl	bdl	bdl	bdl	bdl	bdl	bdl	bdl	bdl
Sc [†]	4.15	5.47	5.98	3.49	0.302	0.044	0.031	0.099	0.117
Ti [†]	748.7	1160	1302	675.0	84.72	5.78	4.61	6.56	18.58
V [†]	16.74	20.80	25.85	9.09	8.36	8.20	4.45	2.91	13.32
Cr*	20.99	25.66	27.25	15.07	4.98	9.26	6.01	1.32	1.99
Co [†]	11.75	10.72	13.85	6.42	0.282	0.200	0.133	0.216	1.41
Ni*	19.87	19.59	23.44	9.29	2.26	4.75	3.32	1.35	10.07
Cu [†]	2.92	2.32	2.02	1.85	1.29	2.33	1.19	3.04	4.10
Zn [†]	35.89	28.33	31.22	18.41	2.36	2.83	3.55	2.41	5.28
Rb [†]	19.64	29.61	34.10	24.20	3.32	0.158	0.070	0.566	0.349
Sr*	21.92	25.81	27.57	36.76	15.1	11.53	4.43	4.99	6.41
Y*	4.36	6.38	6.81	4.72	0.75	0.55	0.54	0.69	1.39
Zr*	18.39	27.49	35.27	19.01	2.58	1.09	0.75	4.05	2.18
Nb [†]	2.31	3.41	4.01	1.99	0.272	0.037	0.030	0.078	0.065
Cs [†]	0.756	1.06	1.25	0.616	0.077	0.011	0.005	0.027	0.038
Ba*	84.28	128.24	142.73	127.64	68.77	1.75	1.12	4.18	1.44
Hf [†]	0.487	0.777	0.935	0.500	0.050	< 0.004	< 0.004	0.030	0.013
Ta [†]	0.159	0.235	0.268	0.147	0.018	< 0.004	< 0.004	< 0.004	0.005
Pb [†]	4.99	6.48	6.61	6.16	1.64	0.826	0.726	2.63	2.50
Th [†]	1.70	2.53	3.04	1.75	0.239	0.011	0.014	0.013	0.056
U [†]	0.325	0.504	0.543	0.499	1.53	0.038	0.035	0.239	0.145

* = ICP-OES data, [†] = ICP-MS data, bdl = below detection limit

Table 3.6: REE concentrations (in ppm), measured with ICP-MS

	B-L-1	B-L-2	B-L-3	S-S-S	B-G-1	B-G-3a	B-G-3b	B-G-4	B-F-1
La	5.60	7.80	12.68	5.54	0.493	0.168	0.409	0.119	0.449
Ce	13.36	18.06	30.01	14.08	0.997	0.424	1.05	0.268	0.628
Pr	1.39	1.89	3.11	1.40	0.122	0.048	0.143	0.022	0.091
Nd	5.30	7.19	11.63	5.36	0.523	0.271	0.725	0.154	0.432
Sm	1.03	1.41	2.17	1.06	0.121	0.077	0.181	0.047	0.097
Eu	0.236	0.319	0.481	0.243	0.031	0.013	0.026	0.009	0.025
Gd	0.941	1.31	1.87	0.978	0.129	0.086	0.167	0.077	0.131
Tb	0.145	0.208	0.277	0.157	0.022	0.014	0.023	0.014	0.021
Dy	0.860	1.23	1.56	0.918	0.142	0.095	0.129	0.112	0.159
Ho	0.168	0.244	0.297	0.183	0.027	0.018	0.020	0.025	0.036
Er	0.492	0.723	0.874	0.543	0.083	0.065	0.057	0.088	0.128
Tm	0.072	0.105	0.127	0.077	0.011	0.011	0.007	0.016	0.020
Yb	0.466	0.698	0.825	0.502	0.080	0.098	0.061	0.141	0.146
Lu	0.069	0.105	0.124	0.075	0.011	0.016	0.008	0.025	0.021
Σ	30.13	41.29	66.04	31.12	2.79	1.40	3.01	1.12	2.38

4 Discussion

4.1 Bulk geochemistry - element relationships and their implications

The bedded radiolarian chert and jasper samples are clearly marine sediments, but the different processes leading to their formation need to be evaluated, along with their depositional environments.

4.1.1 Purely hydrothermal origin?

The hypothesis of the cherts and jaspers being of purely hydrothermal origin, serving as analogues for modern Fe-deposits in seafloor hydrothermal systems, can be tested with strategies complementing each other, making use of geochemical, mineralogical, and textural analyses. A commonly used approach is the examination of major and trace element relationships.

Major and trace element relationships

(Ni+Co+Cu)*10-Fe-Mn diagram One ternary diagram to infer information on the formation process of seafloor deposits uses Fe, Mn, Co, Ni, and Cu concentrations, and was developed by Bonatti et al. (1972) and modified by Hein et al. (1992, 1994). Figure 4.1 shows Group A and B samples

plotted. Their concentrations are all very similar, placing them in the Fe-rich apex, leading to the assumption that the formation process was hydrothermal. This is in accordance with findings from modern Fe-deposits from the Jan Mayen vent fields; Haukelidsæter (2017) reports their samples having a very similar position in this diagram. Late Cretaceous ironstones from the central Pacific region show a similar placement (Hein et al., 1994). The fact that this type of diagram has been in use to investigate more recent seafloor deposits, and not ancient hematitic chert could indicate that it is not as compelling for ancient deposits compared to modern deposits.

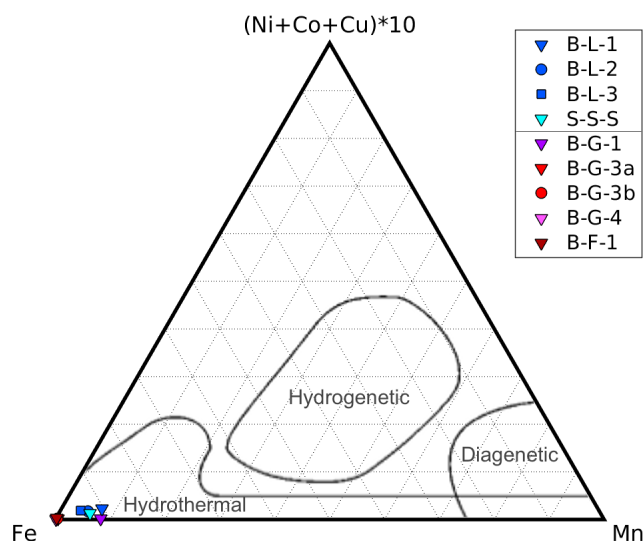


Figure 4.1: $(\text{Ni}+\text{Co}+\text{Cu})\cdot 10$ -Fe-Mn diagram after Bonatti et al. (1972)

Co/Zn ratios A different way to tackle the hydrothermal origin question is to use cobalt/zinc ratios. The transition metals cobalt and zinc can be used to gain information on whether hydrothermal mineralisation took place or whether minerals precipitated hydrogenetically from oxygenated sea water (Toth, 1980, Hein et al., 1994). In hydrothermal deposits, Co is depleted,

while Zn is enriched, resulting in low Co/Zn values. This is because Co is primarily derived from seawater, whereas Zn is present in hydrothermal fluids and readily gets incorporated into deposits (Toth, 1980). Absence of hydrothermal fluids thus leads to significantly higher Co/Zn ratios, indicating a hydrogenous source for the deposits. Typical values for hydrothermal deposits range from 0.07 to 0.15 (Hein et al., 1994), or around the mean of 0.15 (Toth, 1980), whereas hydrogenous deposits have a mean ratio of 2.5 (Toth, 1980). Co/Zn ratios for all samples are displayed in Table F.1 in the appendix on page 146. Group A samples range between 0.33 and 0.44, thus slightly above the mean of 0.15, while Group B samples exhibit values of 0.04 to 0.12, with B-F-1 at 0.27. Group B samples, with the exception of B-F-1, are within the range for hydrothermal deposits defined by Hein et al. (1994), Toth (1980), and the remaining samples, showing only slightly higher ratios, can be interpreted to be significantly closer to the mean for hydrothermal deposits than to the mean of hydrogenous deposits. This supports the hypothesis of a hydrothermal component for all samples, but it can be inferred that Group A samples are not likely to purely be of hydrothermal origin, so other factors strongly influenced their formation.

Al/(Al+Fe+Mn) ratios Another element ratio strengthens this idea. Dividing Al by (Al+Fe+Mn) is a measure of the hydrothermal input to the sediments, low ratios indicate dominating hydrothermal input, whereas high ratios hint towards a low hydrothermal contribution to the sediments during deposition (Yamamoto, 1987). Al is generally not enriched in hydrothermal deposits, since it is not contained within hydrothermal fluids, whereas Fe and Mn (in varying concentrations) are enriched in hydrothermal fluids and thus are present in hydrothermal deposits, leading to the differences in ratios described by Yamamoto (1987). Values described in literature for hydrothermal precipitates are around 0.01 (East Pacific Rise, Boström and Pederson,

1969), and bedded cherts exhibit ratios around 0.60 (Mine Terrane, Japan, Sugisaki et al., 1982, Yamamoto, 1983). Ratios for the samples are provided in Table F.1 in the appendix on page 146. Group A samples have ratios of 0.55 – 0.56, and Group B shows ratios of 0.01 – 0.02, with the exception of B-G-1 (0.13). The values of Group A are significantly higher than Group B, supporting the idea that Group B samples have a purely hydrothermal origin, and Group A samples were influenced by different processes besides hydrothermal activity.

Al-Fe-Mn diagram A different way to utilise and investigate Al, Fe, and Mn concentrations is another ternary diagram. Two fields within it have been identified by Adachi et al. (1986) and Yamamoto (1987), separating hydrothermal cherts from non-hydrothermal cherts. Group A samples plot within the non-hydrothermal field, whereas Group B samples plot within the hydrothermal field (Figure 4.2). Group B samples all plot in the Fe apex of the diagram, due to very low Al and Mn concentrations, but B-G-1 deviates slightly. Similar to the $\text{Al}/(\text{Al}+\text{Fe}+\text{Mn})$ ratios, Group B is clearly defined as a hydrothermal deposit here. But Group A consists of non-hydrothermal deposits, according to the diagram.

The discrepancy between different diagrams inferring either a hydrothermal or a non-hydrothermal origin for Group A samples is interesting and is investigated further through additional measures.

Relationship SiO_2 content and $\sum\text{REEs}$ Both Group A and Group B samples exhibit different trends when correlating SiO_2 content with the sum of REEs (Figure 4.3). The content of SiO_2 in Group A is strongly anti-correlated with the sum of REEs present ($R^2 = 0.88$), with increasing SiO_2 content, the sum of REEs decreases linearly. Sample B-G-1 correlates well with Group A in this regard, including it gives an even stronger correlation

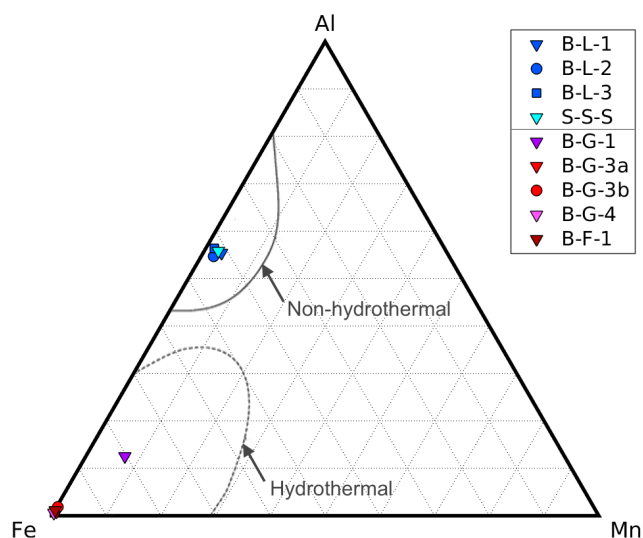


Figure 4.2: Al-Fe-Mn diagram after Adachi et al. (1986)

($R^2 = 0.95$, Figure 4.3 upper right). The same trend cannot be observed for all Group B samples. The sums of REEs are at much lower concentrations in Group B, but they show a positive correlation ($R^2 = 0.64$) with increasing SiO_2 content (Figure 4.3 lower right). The very low concentrations within Group B lead to single samples having a strong impact on the correlation. The strong anti-correlation within Group A (both including and excluding B-G-1) indicates that REEs in the radiolarian cherts have a different source than the SiO_2 , a dilution by SiO_2 input can be inferred from a source not providing significant REE input. The positive correlation within Group B (in- and excluding B-G-1) on the other hand can be taken as indication for SiO_2 and REEs originating from the same source in the jaspers. It has to be noted though, that with such low concentrations for REEs, a correlation can be problematic and is not as significant as for higher concentrations (such as seen in Group A). The fact that B-G-1 correlates well with both groups indicates it could have been affected by both processes leading to chert and

jasper formation. These processes can potentially be linked to mineralogical and textural features and will be discussed later in Section 4.2.

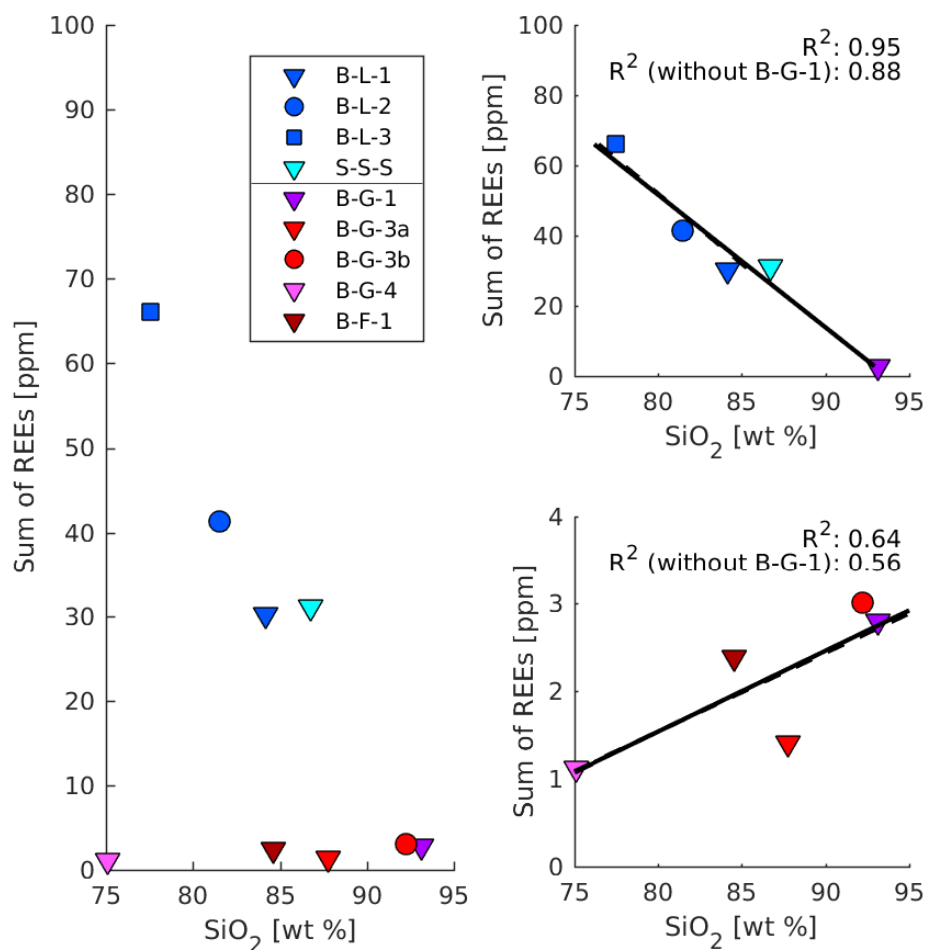


Figure 4.3: Correlation of SiO₂ content and \sum REE for both Group A and B

Relationship Fe and \sum REEs Fe and REE content are correlated to a different extent for both groups (Figure 4.4). Group A shows a strong positive correlation ($R^2 = 0.85$) without including B-G-1, and a less strong,

but still significant correlation with B-G-1 included ($R^2 = 0.76$, Figure 4.4 upper right). With increasing Fe content, the sum of REEs increases. Group B samples anti-correlate ($R^2 = 0.56$) when including B-G-1, and a little less when excluding it ($R^2 = 0.46$, Figure 4.4 lower right).

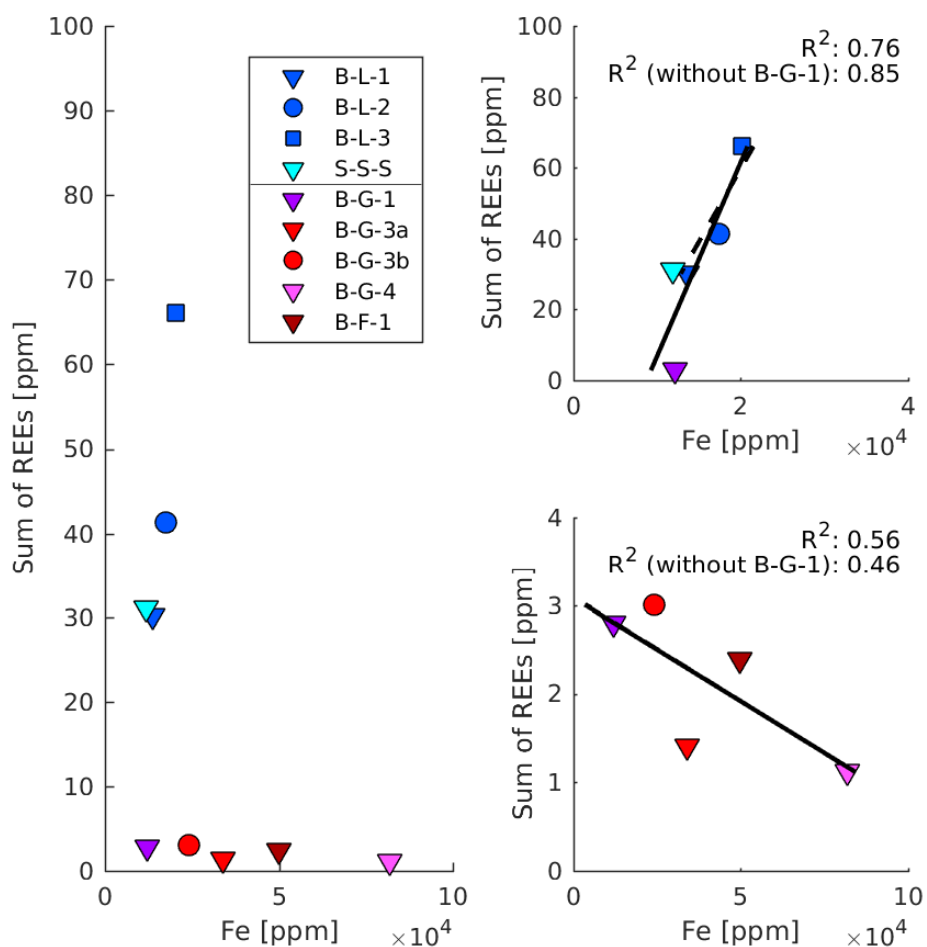


Figure 4.4: Correlation of Fe content and REE sum for both Group A and B

For Group A it can be inferred that both Fe and REEs have the same source. It is likely that this source is mainly terrigenous material and to a

lesser extent seawater and/or a hydrothermal component. The even stronger correlation when excluding B-G-1 indicates that B-G-1 has an additional source for Fe, increasing the Fe content slightly without increasing the REEs. This is very likely a hydrothermal component, stronger in B-G-1 than in Group A radiolarian cherts. The anti-correlation exhibited by Group B samples hints towards two different sources for Fe and REEs. Again, this need to be taken with care, since the REEs are present in such low concentrations. The anti-correlation is not very significant, and combined with the fact that the sum of REEs are so low, it can be assumed that the trend is not representative. It can also indicate that the Fe and REEs potentially have the same source (hydrothermal fluid), but an additional component contributes to the REE content, possibly seawater.

REE patterns

An additional approach of great importance to investigate a possible hydrothermal origin of chert samples is the analysis of concentrations and relative abundances of rare earth elements. They remain immobile during diagenesis (Murray, 1994), and thus preserve initial concentrations, providing a helpful tool for determining processes involved in the formation of cherts. Especially $(La/Yb)_N$ ratios, Ce/Ce* anomalies, and Eu/Eu* anomalies contribute crucially to the analysis.

Group A and B samples display distinctly different REE patterns, leading to the assumption that they each have been formed by different processes. The comparison between both groups is depicted in Figure 4.6. Group A exhibits much higher concentrations than Group B. The differences in LREE and HREE concentrations between the groups are visible, although depending on the normalisation values, they show different behaviour.

Resemblances between REE patterns In all three diagrams, Group A samples all show a very good correlation with each other, while Group B samples show slightly less coherent behaviour. Sample B-G-1, though it has the same concentration levels as Group B samples, correlates much better with Group A samples, when looking both at the REE patterns, and at the correlation coefficients in Tables E.1 to E.3 in the appendix on pages 144 to 145. The best correlation is present in the chondrite-normalised REE patterns. This evident correlation is very likely connected to the fact that B-G-1 resembles Group A samples more than Group B samples in both mineralogy and texture, except for the abundance of magnetite crystals.

Differences between applied normalisations Normalising the REE patterns to different values, chondrite, NASC, and PAAS, results in different $(\text{La}/\text{Yb})_N$ ratios, Ce/Ce^* , and Eu/Eu^* anomalies, as described earlier (Tables 3.2 and 3.3). The three used normalisations stem from various sources. Chondrite-normalised values after Boynton (1984) are taken from an average over CI chondritic meteorites, which are interpreted to represent the initial solar nebula composition best, being relatively unfractionated (Rollinson, 1993). NASC after Gromet et al. (1984) describes an average marine sediment, produced by recurrent erosion recycling, using North American shales for averaging (Rollinson, 1993). And PAAS, a different shale normalisation after McLennan (1989), has the same background, but the average is based on Australian shales deposited after the Archean. (Rollinson, 1993). The concentrations of REEs vary extensively between the normalisations. A visual representation of this is depicted in Figure 4.5. Both NASC and PAAS are roughly 100 x enriched in LREEs and approximately 10 x enriched in HREEs, compared to chondrite. PAAS is slightly more enriched in LREEs than NASC, whereas NASC contains more HREEs. Thus, $(\text{La}/\text{Yb})_N$ ratios are relatively high (6.74 and 9.13, respectively). Values for Ce/Ce^* are very

close to 1, so no obvious Ce anomaly exists for NASC and PAAS normalised to chondrite. Both normalisations show a strong negative Eu anomaly (0.67 for NASC, 0.65 for PAAS) compared to chondrite, thus they are both depleted in Eu. This has implications for the interpretation of REE patterns in Figure 4.6.

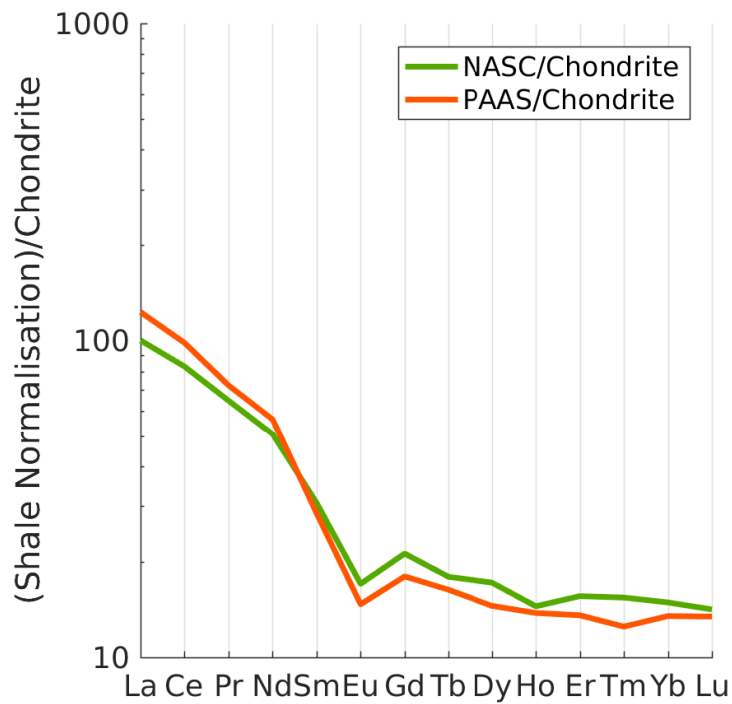
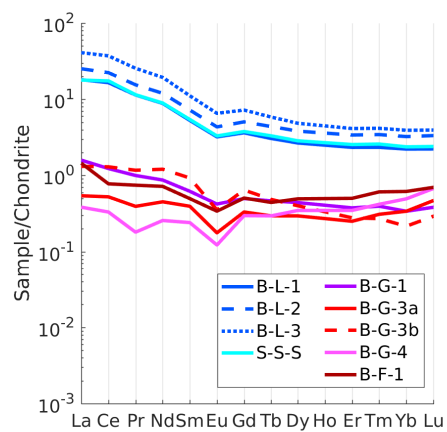
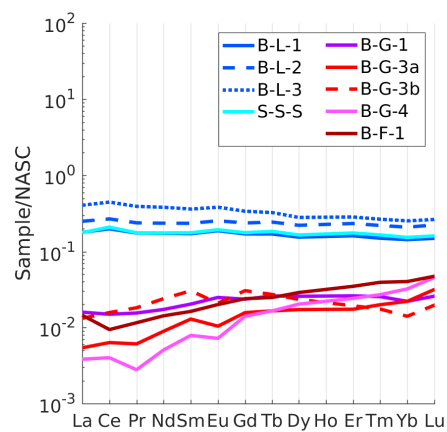


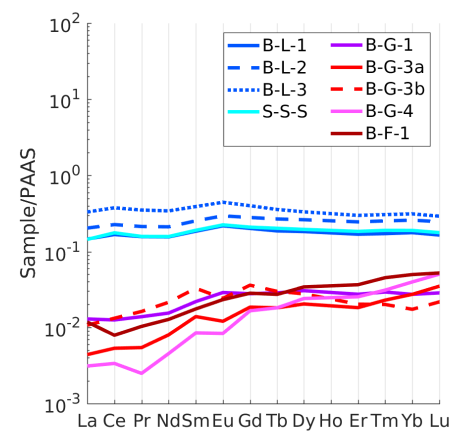
Figure 4.5: Normalisation of NASC and PAAS over chondrite



(a) Chondrite-normalisation



(b) NASC-normalisation



(c) PAAS-normalisation

Figure 4.6: Different REE-normalisations of Group A and Group B samples

Fe-oxyhydroxide particles as REE-scavengers According to German et al. (1990) and Sherrell et al. (1999), Fe-oxyhydroxides are excellent scavengers of REEs present in the fluid they formed in. Thus, they are able to mirror the REE pattern of their source fluid (Johannessen et al., 2017). The REE composition of Fe-oxyhydroxides is not believed to change during metamorphism, making them a useful tool when comparing different potential source fluids with the samples themselves (e.g. Grenne and Slack, 2003b). Figure 4.7 displays this comparison, with samples and fluids being normalised to chondrite. Reference high-temperature hydrothermal fluids exhibit a high $(\text{La}/\text{Yb})_N$ ratio, a slightly negative Ce anomaly, and a very distinct positive Eu anomaly. Whereas reference low-temperature hydrothermal fluids show a very low $(\text{La}/\text{Yb})_N$ ratio, also a slightly negative Ce anomaly, and a not insignificant negative Eu anomaly (Johannessen et al., 2017). Reference oxie deep sea water remotely resembles the low-temperature hydrothermal fluid REE pattern, with a very low $(\text{La}/\text{Yb})_N$ ratio, but a significantly stronger negative Ce anomaly and a slight negative Eu anomaly (Johannessen et al., 2017). As mentioned before, $(\text{La}/\text{Yb})_N$ ratios, Ce anomalies, and Eu anomalies are useful for analysis and are investigated in the following paragraphs for the samples, and in comparison with the potential source fluids.

$(\text{La}/\text{Yb})_N$ ratios The significant difference in $(\text{La}/\text{Yb})_N$ ratios between chondrite normalisation and shale normalisations mentioned earlier complicates comparisons to literature for LREE/HREE values for interpreting formation processes, which is why it is important to keep in mind which normalisation is used. The use of shale normalisations can potentially overprint crucial information that the normalisation to chondrite would emphasize. In this study, for chondrite-normalised values, Group A exhibits intermediate to high ratios, and Group B low ratios, but for shale-normalised values, very low ratios are observed for both groups. Comparing the chondrite-normalised

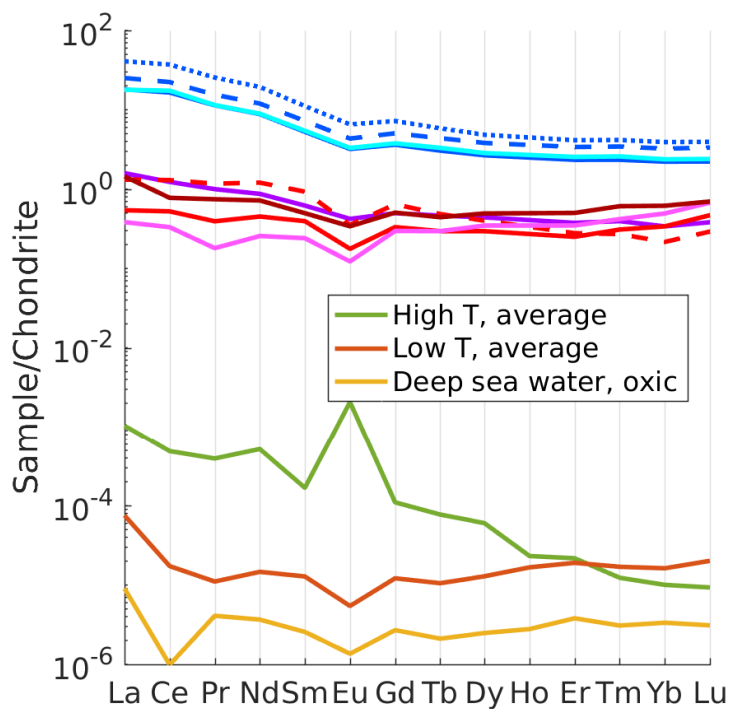


Figure 4.7: Comparison of REE patterns of samples and potential source fluids: high-temperature hydrothermal fluids, low-temperature hydrothermal fluids, and oxic deep sea water, sample colours are consistent with those used in Figure 4.6

REE patterns of the samples to the chondrite-normalised possible source fluids in Figure 4.7, shows that Group A samples match neither of the fluids REE patterns. Group B samples REE patterns, on the other hand, best match the low-temperature hydrothermal fluid REE pattern.

Investigation of the NASC-normalisation of Group A samples in Figure 4.6b shows an interesting trend. The REE patterns are very flat, and the REE concentrations normalised to NASC range around 0.2 and 0.4, indicating that their behaviour generally resembles NASC-REE behaviour, but

have lower concentrations. This is an indication for a terrigenous detrital component involved in the formation of Group A samples, which will be investigated further in Section 4.1.2. Comparing Fe oxide concentrations of Group A samples (Fe_2O_3 ca. 4 to 6 wt%) to the concentration of Fe oxides in NASC (FeO 5.66 wt%, Gromet et al., 1984), while keeping the REE depletion of Group A samples in mind, gives a surprising result: Group A samples are approximately 4x enriched compared to NASC. This significant enrichment in Fe cannot be explained by only detrital input resembling the NASC composition alone, there must be another source for the high Fe contents, which could potentially be hydrothermal. A different explanation could be Fe-rich terrigenous input, e.g. from volcanic material.

Ce anomalies Due to the fact that both shale normalisations compared to chondrite (Figure 4.5) do not exhibit strong positive or negative Ce anomalies, all normalisations are feasible for their investigation. The Ce anomalies for Group A and B samples are slightly positive to non-existent (B-F-1 being an exception with a moderately negative Ce anomaly), independent of the normalisation scheme used (Tables 3.2 and 3.3). Shale-normalised Ce anomalies are insignificantly lower than chondrite-normalised Ce anomalies. The comparison of Ce anomalies in samples to oxic seawater and hydrothermal fluids infers the following: Neither the high-temperature hydrothermal fluids, nor the low-temperature hydrothermal fluids exhibit positive Ce anomalies and thus cannot be the main REE-source fluid for the samples exhibiting slightly positive Ce anomalies. The pronounced negative Ce anomaly of oxygenated deep sea water is not representative of the Ce anomalies in the samples, and thus it cannot have been the source fluid either. Missing strongly negative Ce anomalies can be an indicator for reducing conditions in the source fluids. In oxic seawater, dissolved Ce(III) becomes oxidised to Ce(IV), which is insoluble and thus gets removed from the seawater (Elder-

field, 1988), resulting in the prominent negative Ce anomaly (Figure 4.7). This behaviour is only observed for Ce, the rest of the REEs are strictly trivalent (Eu being an exception) and cannot be oxidised (German and Elderfield, 1990). Suboxic seawater on the other hand, shows less negative to positive Ce anomalies, due to the fact that under low O₂ conditions, less Ce(III) oxidation to Ce(IV) can occur (German and Elderfield, 1990). Under anoxic conditions, Ce is reduced (German and Elderfield, 1990) and results in more positive Ce anomalies in seawater that are reflected in sediments deposited under such conditions (Wilde et al., 1996).

The very slight positive Ce anomalies within the samples of Group A can be inferred to have been caused by deposition under suboxic conditions, and thus obtaining of REEs from the suboxic seawater, besides from terrigenous input, investigated in 4.1.2. This assumption is based on the weakly positive Ce anomalies observed, and low Mn concentrations support this claim. Mn oxide particles have the ability to capture Ce on their surfaces along with other REEs, but only under conditions favourable for Mn oxidation (German et al., 1991), and the low concentrations of Mn within all samples argue against this mechanism to have caused the slightly positive Ce anomalies. Also, all samples containing hematite contradicts anoxic conditions during the deposition, as pyrite could have formed instead of hematite from precursor material, depending on the supply of H₂S (Slack et al., 2007). Thus, suboxic conditions are concluded to have been present during the formation of Group A samples.

For Group B samples, the hydrothermal component contributing to the deposition of the samples is interpreted to be much stronger than for Group A, as discussed before. Thus, when investigating the Ce anomaly of Group B samples, the assumption can be made that seawater, whether it is oxic, suboxic, or anoxic, is not the main source for the REEs, since a hydrogenous source has been ruled out for Group B samples by very low Co/Zn ratios.

The very slightly positive Ce anomalies, except for B-F-1 which exhibits a moderate negative Ce anomaly, can neither be explained only by high-, nor by low-temperature fluids supplying the REEs. B-G-1, resembling Group A samples best, might have formed very similarly to them, thus the small positive Ce anomaly can be explained by suboxic seawater being present during formation, along with hydrothermal fluids. B-F-1 differs from B-G-3a, -3b, and -4 in texture, as it contains copious amounts of filamentous structures indicating microbial participation in Fe-oxyhydroxide precipitation. With rapid microbially induced Fe-oxyhydroxide precipitation, the kinetically slow Ce(III)-oxidation (Bau and Dulski, 1996) from hydrothermal fluids is inhibited, resulting in a negative Ce anomaly. Abiogenic precipitation of Fe-oxyhydroxides is much slower than biological precipitation. The absence of filamentous structures in B-G-3a, -3b, and -4 indicates this process as the main process of Fe-oxyhydroxide formation in these samples. Thus, the slower precipitation of Fe-oxyhydroxides by abiogenic processes can lead to more Ce(III)-oxidation of Ce from hydrothermal fluids, resulting in slightly positive Ce anomalies. With seawater not substantially contributing REEs to Group B samples (except for B-G-1 to a slight extent), it is difficult to infer whether ambient seawater was oxic or suboxic. A certain level of O₂ within the seawater must have been present though, so that both Ce(III)- and Fe(II)-oxidation could have taken place. The O₂ concentrations might have potentially been lower than today, though.

The Ce anomaly does not contribute to solving the question of low- or high-temperature hydrothermal fluids having been involved, but the investigation of the Eu anomaly is a crucial means for this.

Eu anomalies Eu anomalies are used to get an approximation of the temperature of the hydrothermal source fluid, and thus information about depositional constraints (Michard et al., 1993). A very apparent discrepancy

can be seen for the Eu anomalies between the differently normalised REE patterns (Figure 4.6, Tables 3.2 and 3.3). Using a set of normalisation values already depleted in Eu leads to apparently higher values, potentially turning negative Eu anomalies into positive Eu anomalies. This is visible in the results of this study, as all samples normalised to chondrite exhibit negative Eu anomalies, whereas the normalisation to NASC and PAAS yields positive values for all Group A samples and two Group B samples (B-G-1 and B-F-1), indicating slightly positive Eu anomalies. Thus, to investigate Eu anomalies in hematitic chert cautiously, the normalisation to chondrite is the superior choice, as already stated by Johannessen et al. (2017). Suboxic seawater as main source fluid is inferred from the Ce anomaly for Group A samples, and hydrothermal fluids only played a minor role in their formation. Group B samples on the other hand are presumed to mainly stem from hydrothermal fluids. Figure 4.7 shows the strongly differing REE patterns for both. Eu(II) is considered unstable at temperatures below 250 – 200 °C in a reducing regime (Sverjensky, 1984, Wood, 1990), but Eu(III) is stable, though much more immobile (Michard et al., 1993). This leads to the hypothesis of Eu(III) being immobile at low temperatures and reducing conditions, so less Eu will be leached out of the subsurface the hydrothermal fluids circulate through (Johannessen et al., 2017). This is the cause of the prevalent negative Eu anomaly in low-temperature hydrothermal fluids. It also explains the strong positive Eu anomaly high-temperature hydrothermal fluids exhibit: high temperatures lead to the stabilisation of Eu(II) and subsequently more Eu is leached out of the subsurface and enters the fluid, causing the positive Eu anomaly within high-temperature hydrothermal fluids. Both Group A and Group B samples exhibit negative Eu anomalies, hinting towards low-temperature hydrothermal fluids being present during their deposition. The difference in magnitude of the Eu anomaly between Group A and Group B is evident, with Group B samples displaying stronger negative Eu anomalies

than Group A. Thus, the REEs in Group B are assumed to stem mainly from low-temperature hydrothermal fluids, whereas Group A samples must have undergone different processes. This difference can be explained by Group B-REEs having been mainly derived from hydrothermal fluids, whereas Group A-REEs are mainly derived from a different source than hydrothermal fluids. Slack et al. (2007) describe a similar setting of jaspers and ironstones believed to have formed from hydrothermal plume fallout under suboxic conditions and a large seawater-derived component, but their samples all exhibit positive Eu anomalies. Their samples were normalised to PAAS. The normalisation of Group A Eu anomalies to PAAS actually yields slightly positive values, due to the depletion of Eu in the PAAS material itself, visible when normalised to chondrite (Figure 4.5). As mentioned, shale normalisations depleted in Eu are problematic when investigating hydrothermal processes. Normalising the REE values of Slack et al. (2007) to chondrite instead of PAAS, 8 out of 10 Eu anomalies actually turn out to be negative (0.77 - 0.99, average 0.85). This affects their claim of high-temperature hydrothermal fluids having been involved in the formation of jasper and ironstones, the newly normalised Eu anomalies indicate low-temperature hydrothermal fluids as source instead. Thus, their findings are here interpreted to be problematic in regard to the source fluid. The chondrite-normalised Eu anomalies match the chondrite-normalised values for Group A much better, and this supports the hypothesis that low-temperature hydrothermal fluids could have played a minor role in the formation, next to suboxic sea water.

Summed up, what does this indicate?

A purely hydrothermal origin can be interpreted for Group B samples, Fe-oxyhydroxides produced by low-temperature hydrothermal fluids have scavenged REEs from these rather than from high-temperature fluids or ambient sea water. Strong evidence has been provided and the determination of the

depositional environment in the following section can help better understand the settings in which the formation of Group B occurred. An exception in Group B is sample B-G-1, showing a stronger correlation with Group A than the rest of Group B, while the REE concentrations more closely resemble Group B samples. This discrepancy will be investigated further.

Group A samples have a different and less straightforward formation history. Evidence from the Ce anomalies points towards formation under suboxic conditions and scavenging of REEs from suboxic seawater and/or terrigenous detritus REE contributions. Enriched Fe contents either hint towards a hydrothermal contribution, or towards reducing conditions, or a combination of both. If a contribution from a hydrothermal source took place, a low-temperature hydrothermal fluid is more likely than high-temperature hydrothermal fluids, based on the prevailing negative Eu anomalies. Determining the depositional environment Group A samples have formed in is crucial to shed light on the role of detrital input and for fully understanding the processes leading to their formation.

4.1.2 Depositional environment

Deposition of marine sediments occurs in several, very different environments. Continental margins are influenced by terrigenous input from landmasses and exhibit shallow depths, under this term back-arc basins, marginal seas, epicontinental seas, and open continental shelves are grouped together (e.g. Murray, 1994). The deep ocean bottom as depositional environment, on the other hand, is more dominated by pelagic clay deposition (e.g. Murray, 1994). Proximal to spreading ridges, marine sediments are generally dominated by higher Fe oxide concentrations due to hydrothermal activity and a lack in significant terrigenous input and pelagic deposition (e.g. Murray, 1994).

Understanding the diverse depositional environments the different types

of hematitic chert were deposited in is possible by investigating major and trace element relationships, as well as REE behaviour.

MnO/TiO₂ ratios One approach proposed by Sugisaki et al. (1982) is the use of MnO/TiO₂ ratios. High concentrations in MnO are generally related to pelagic sediments, whereas high concentrations in TiO₂ imply terrigenous components being present due to the immobility of Ti and presence in aluminosilicate phases (Murray, 1994). More than twice as much TiO₂ than MnO is typical in continental margin settings (ratio of < 0.5), whereas higher MnO and/or lower TiO₂ concentrations (ratio of > 0.5) are connected to more pelagic dominated sediment deposition on the deep ocean floor (Sugisaki et al., 1982). Group A samples exhibit low ratios with an average of 0.8, whereas Group B samples have much higher ratios with an average of 11.6 (B-F-1 only showing 1.72, see Table F.1 in the appendix on page 146). Strictly seen, this indicates a deep ocean floor deposition for all samples, but the average value for Group A samples is very close to the dividing value of 0.5. This can be interpreted to indicate a setting where deposition of terrigenous material and pelagic clay sediments overlaps, but the terrigenous input dominates. The very high ratios for Group B indicate a depositional environment far away from landmasses supplying terrigenous material rich in TiO₂, thus the deep ocean floor. Using this method can be problematic for Group B samples due to the hydrothermal origin resulting in elevated Mn input from hydrothermal fluids, though. These interpretations are consistent with what the Al-Ti correlations and respective concentrations indicate.

The use of MnO for depositional environment distinction is debated, Murray (1994) claims Mn is mobile during diagenetic processes affecting chert, and thus MnO concentrations in cherts potentially do not adequately represent the MnO concentrations present in the sediments during deposition. Several authors deem the diagenetically induced mobility of Mn as insignif-

icant due to consistency of their results with other measures of depositional environments (e.g. Shimizu et al., 2001, Udchachon et al., 2011). Nevertheless, the MnO/TiO₂ ratio interpretations should be taken with care and cannot be used as sole indicators for depositional environment discrimination, which is why other approaches are necessary.

Al-Ti correlation Al, Ti, Fe, and the REEs are elements considered to withstand diagenetic effects (Murray, 1994), which is why a focus on these elements is favoured to determine depositional environments. A different approach thus makes use of the relationship of Al and Ti. Al and Ti are both treated as immobile in seawater and hydrothermal fluids, and thus are taken as indicators for the presence of a detrital component (MacLean and Kranidiotis, 1987), because they are generally contained in aluminosilicate phases (Murray, 1994). Both are commonly associated with terrigenous material. Their strong correlation for Groups A and B (Figures 3.18a and 3.20a) supports the assumption of both elements being immobile. Generally significantly higher concentrations of Al and Ti in Group A than in Group B can be taken as a signal for Group A having been affected much stronger by terrigenous detrital input than Group B. The elevated values of both Al and Ti for B-G-1 in regard to the remaining Group B samples are remarkable, but still significantly lower than Group A samples (Figure D.1a in the appendix on page 143). This implies that Group A sample sediments formed in the vicinity of landmasses responsible for terrigenous material deposited within Group A samples. The small concentrations in Group B, yet correlated, suggest that terrigenous input is negligible, providing evidence for a depositional environment virtually unaffected by terrigenous material. B-G-1 is very likely to contain a small component of terrigenous material, due to the generally higher values than the rest of Group B.

$\text{Al}_2\text{O}_3/(\text{Al}_2\text{O}_3+\text{Fe}_2\text{O}_3)$ - $(\text{La}/\text{Ce})_N$ diagram Murray (1994) developed a diagram to determine the depositional environment of cherts based on an extensive database comprised of geochemical data of 49 chert sequences (early Paleozoic to Neogene). The three depositional zones “ridge-proximal”, “pelagic”, and “continental margin” were defined (Figure 4.8). The La/Ce ratio (normalised to NASC) is indicative by itself for these environments.

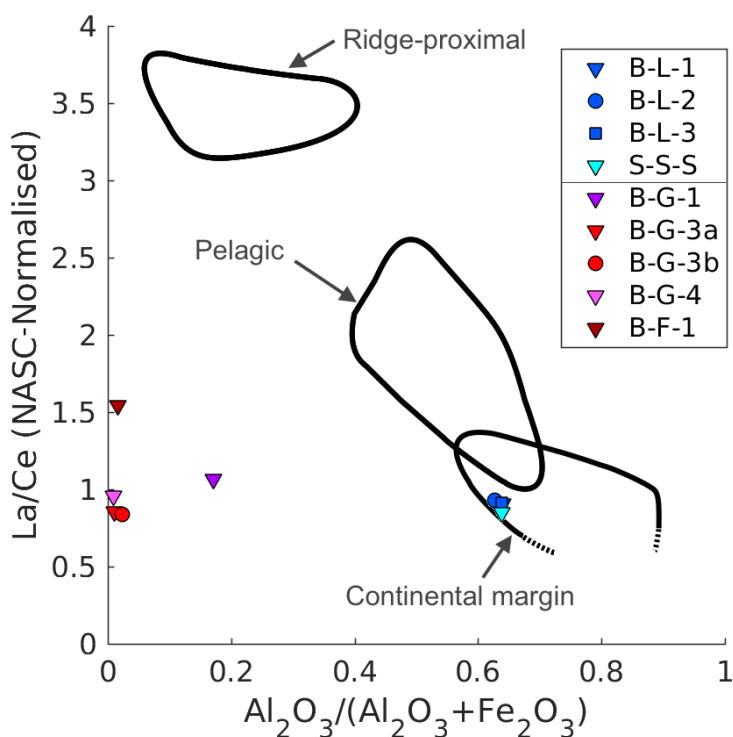


Figure 4.8: $\text{Al}_2\text{O}_3/(\text{Al}_2\text{O}_3+\text{Fe}_2\text{O}_3)$ - $(\text{La}/\text{Ce})_N$ diagram after Murray (1994)

Low (La/Ce) values (~ 1) are typical in cherts deposited along the continental margin due to the influence of terrigenous detritus, which itself is characterised by values ~ 1 . Adsorption of REEs in marginal, oxygen-poor waters not depleted in Ce can cause a similar La/Ce ratio in marine sediments (Murray et al., 1991, Murray, 1994). Intermediate values (1 - 2.5) are indica-

tive of deposition in a pelagic environment due to the increased incorporation of Ce to marine sediments unaffected by hydrothermal, metalliferous input, and terrigenous detritus (Murray et al., 1991, Murray, 1994). Higher values, around 3.5, hint towards a deposition close to ridges with high hydrothermal activity, where a pronounced depletion of Ce in oxic seawater occurs. The REE scavenging occurring in metalliferous plumes from the seawater is believed to be the main process responsible for REE patterns in ridge-proximal cherts, leading to high La/Ce ratios due to the present Ce depletion in seawater (Murray et al., 1991, Murray, 1994). $\text{Al}_2\text{O}_3/(\text{Al}_2\text{O}_3+\text{Fe}_2\text{O}_3)$ is taken as indicator for hydrothermal activity and terrigenous input. High values (0.6 - 0.9) are caused by minimal presence of Fe and high concentrations of Al, typical for deposition far away from hydrothermal activity, thus continental margins. Values between 0.4 and 0.7 are characteristic for pelagic deposition, pelagic sediments exhibit this range in composition. Low values (0.1 - 0.4) are typical for Al-poor and Fe-rich environments, thus proximal to ridges, where the hydrothermal activity produces Fe-rich deposits.

Group A samples plot very closely to each other within the continental margin field, due to relatively high $\text{Al}_2\text{O}_3/(\text{Al}_2\text{O}_3+\text{Fe}_2\text{O}_3)$ values and La/Ce ratios typical for terrigenous input (Figure 4.8). Group B samples exhibit a different behaviour. La/Ce ratios are ~ 1 (B-F-1 1.5), but their $\text{Al}_2\text{O}_3/(\text{Al}_2\text{O}_3+\text{Fe}_2\text{O}_3)$ ratios vary distinctly; they are much lower than in Group A samples. B-G-1 has the highest ratio of approximately 0.2, whereas the other samples are at 0.01 to 0.02, induced by their extremely low Al concentrations. A ridge-proximal deposition seems likely for Group B samples due to their high Fe contents and REE patterns, but the fact that they do not fall into the ridge-proximal field defined by Murray (1994) is intriguing. The La/Ce ratios are defined for cherts deposited from metalliferous plumes scavenging REEs from the ambient seawater (hydrogenetic formation, Murray, 1994), but the low ratios for Group B samples indicate that this process

does not define their deposition, supported by their Co/Zn ratios, indicating a strictly hydrothermal origin for Group B samples. Thus, the formation of plume-derived jaspers suggested by Grenne and Slack (2003*a,b*, 2005), Slack et al. (2007) as analogues for Group B samples is ruled out here. It is more likely that low-temperature hydrothermal fluids were the main source for the REEs in Group B, as discussed before. The location of Group B samples in Figure 4.8 can either be explained by the lack of a distinct negative Ce anomaly in the source fluid or, more likely, by uptake of Ce(III) oxides from hydrothermal fluids during abiogenic Fe-oxyhydroxide precipitation in B-G-3a, -3b, and -4. B-F-1 is the only sample with a defined negative Ce anomaly (less uptake of Ce(III) oxides due to microbially induced Fe-oxyhydroxide precipitation being faster than the abiogenic pathway) and thus exhibits a slightly higher La/Ce ratio than the rest of Group B.

In summation, the diagram introduced by Murray (1994) places Group A samples in a terrigenous-dominated continental margin depositional environment, while Group B does not fall into a predefined field. Group B nevertheless can be explained by not having formed from metalliferous plume fallout in a ridge-proximal environment, but more likely directly from low-temperature hydrothermal fluids without much seawater-interference, in an area of high hydrothermal activity.

High Field Strength Elements (HFSE) The immobile behaviour of Ti is caused by its high ionic charge and low ionic radius; a similar behaviour can be observed for other HFSE. They are generally unable to enter aqueous fluid phases, so hydrothermal fluids cannot become enriched in HFSE by leaching rocks containing them, leading to hydrothermal deposits not being enriched either. This means HFSE are stable in seafloor hydrothermal systems and even under low- to medium-grade metamorphic conditions (Rollinson, 1993). Thus, HFSE are a reliable tool to discriminate between marine sediments

affected and unaffected by detrital input containing significant amounts of HFSE.

Higher concentrations of HFSE are evident in Group A samples when compared to Group B samples. Except for Ti (around 1000 ppm), all HFSE in Group A are below 40 ppm, while Group B samples are lower than 2 ppm (Ti: <100 ppm, average <25 ppm). Strong correlations between Ti-Zr and Ti-Sc can be taken as analogous to how well Ti and other HFSE correlate. The positive correlations between Al, Ti, and additional HFSE and generally higher concentrations in Group A demonstrate a significantly higher amount of detrital input than in Group B. Thus, the effect of detrital input containing HFSE is negligible for Group B, while Group A is strongly affected. Sample B-G-1 is an exception, as HFSE concentrations are generally higher than the average, indicating a small influence on the chemistry of the sample from detrital sources. The insignificant detrital component in the rest of Group B implies that the REE patterns of Group B samples confidently illustrate the hydrothermal fluid composition without interference from detrital input.

Chalcophile elements The chalcophile elements Cu, Zn, and Pb only exhibit very low concentrations in all samples, with their average sum being below 40 ppm for Group A samples, and below 10 ppm for Group B samples. A high amount of chalcophile elements indicates a detrital component inferred from hydrothermal sulphide particle fallout. The fact that concentrations in all samples are very low argues against a significant input of detrital sulphidic material from high-temperature hydrothermal venting for all samples. This indicates either distal deposition from high-temperature hydrothermal venting or deposition from low-temperature hydrothermal venting.

V/100-Sc/10-Th diagram The relationship between concentrations in V, Sc, and Th can be used to infer knowledge about the geochemistry of

marine sedimentary deposits and their formation processes. V is enriched in seawater and contains nearly no Sc and Th, similar to Fe-oxyhydroxides. Fe-oxyhydroxides are generally a little lower in V and can exhibit a range of concentrations. Terrigenous sediment and pelagic clay, on the other hand, are most enriched in Th in comparison to V and Sc. Fields of ranges in concentration are depicted in Figure 4.9, along with Group A and B samples being plotted. The difference between both is very distinct. Samples of Group B plot in vicinity of the “Fe-oxyhydroxides”-field, with one exception, B-G-1. B-G-1 plots closer to Group A samples, which are located within the “terrigenous sediment and pelagic clay”-field.

This diagram strengthens the theory of Group A having strongly been affected by terrigenous sedimentary input, since all samples plot very closely to the average concentration of NASC. Group B samples on the other hand, with concentrations of Th, V, and Sc typical for Fe-oxyhydroxides, are yet again proven to not substantially been affected by detrital input. B-G-1 showing a closer resemblance in concentrations within Figure 4.9 indicates that terrigenous detritus affected the composition of it much more strongly than the rest of Group B.

Summed up, what does this indicate? Group A samples were strongly influenced by terrigenous detrital input; landmasses nearby must have been the source. This can be explained by several types of settings grouped together under the term continental margin (back-arc basin, marginal sea, epicontinental sea, open continental shelf, Murray, 1994). A minor hydrothermal component might have contributed to the formation of the samples, but this cannot be said with certainty.

Group B samples were not significantly influenced by detrital material, neither from terrigenous sources or pelagic sediments, nor from sulphide particle fallout from hydrothermal plumes, indicating that REE patterns are not

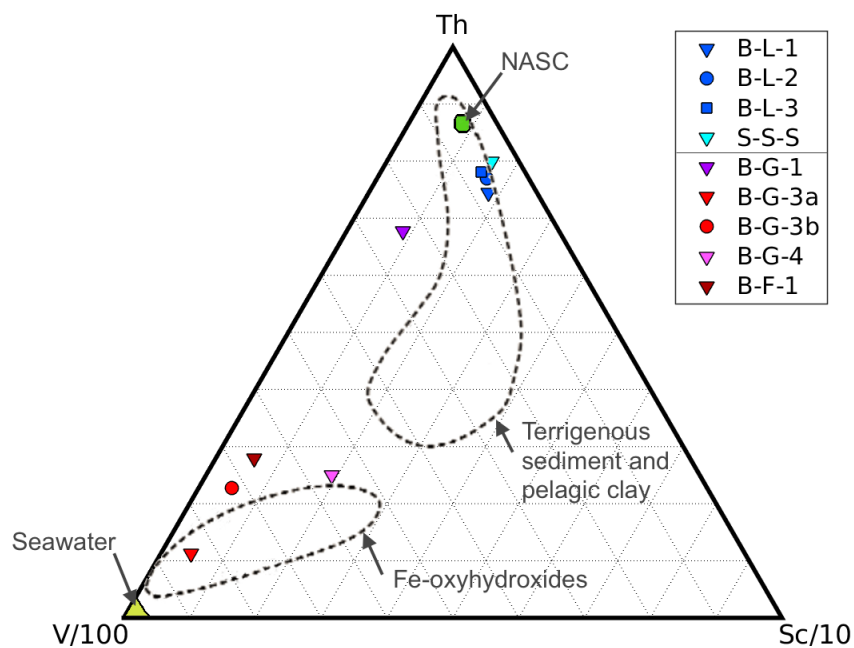


Figure 4.9: Th-V/100-Sc/10 diagram after Grenne and Slack (2005)

affected. The theory of low-temperature hydrothermal fluids acting as main REE-source is supported by negligible detritus. Once again, B-G-1 is an exception, as it shows signs for detrital terrigenous input, yet to a much lesser extent than Group A samples. Submarine deposition must have taken place distal to landmasses and not significantly influenced by high-temperature hydrothermal venting. The relationship between regional geology and interpreted depositional environments will be discussed in Section 4.4.

4.2 Mineralogy and texture contributions

4.2.1 Group-specific traits and their implications

Both groups show specific traits in mineralogy and textures not present in the other. These can be used to better understand and distinguish the differences in depositional processes and formation settings.

Group A - bedded radiolarian cherts

Presence of radiolarians A variety of radiolarian skeletons have been found in cherts of various ages (Jones and Murchey, 1986). The oldest evidence for fossilised radiolarians stems from the early Cambrian (Braun et al., 2007). Radiolarians are protozoa, marine organisms creating silica shells of sizes generally around 100 μm to 200 μm (Smalley, 1963), but their size can range from 30 μm to 2 mm (De Wever et al., 2001). Skeleton shapes vary: spherical and conical structures are known, while spines may or may not be present (Campbell, 1952). The shells, when produced, consist of biogenic opal ($\text{SiO}_2 \cdot n\text{H}_2\text{O}$), which is chemically unstable (Jones and Murchey, 1986). The dissolution and re-precipitation as opal-CT and finally as quartz leads to the preservation of the original shape within the marine host rock (Jones and Segnet, 1972, Kastner et al., 1977, Hein et al., 1978, Jones and Murchey, 1986). According to Jones and Murchey (1986), 98 % of the unstable biogenic opal shells are dissolved within the water column and on the seafloor before they can undergo burial. Thus, it is assumed that radiolarians in marine sedimentary rocks are only present in cases of mass-production and death of large groups of radiolarians, leading to formation of siliceous/radiolarian ooze on the seafloor, burial, and preservation, linked with silica diagenesis (Jones and Murchey, 1986).

The spherical structures, consisting of quartz crystals bigger than the mi-

microcrystalline matrix in Group A samples, are very likely radiolarian shell remnants. A striking similarity between radiolarian shell remnants found in Group A radiolarian cherts and radiolarian cherts described in the literature (e.g. Leistel et al., 1998) is present. Both size and shape, as well as the composition of larger xenomorphic quartz crystals than the surrounding microcrystalline quartz matrix, are indicative of this interpretation.

According to Jones and Murchey (1986), the presence of radiolarians can aid in understanding the depositional environment. Commonly, radiolarians are characteristic for great depths, near or below the calcite compensation depth, which has been shallower prior to the Mesozoic than it is today (Jones and Murchey, 1986). Nevertheless, Leistel et al. (1998) state that their presence cannot always be taken as an indicator for great depths due to the fact that they can also be abundant in shallow water enriched in silica, for example in outer shelf environments. Yet, their presence does pinpoint the formation of Group A samples within a marine environment enriched in silica.

The very high SiO_2 content in all Group A samples can be associated with the presence of radiolarian shell remnants, thus the precursor of quartz in the sample must have been biogenic opal, recrystallised to quartz over time. A small amount of the quartz can possibly be attributed to terrigenous detritus as well. Additionally, in the event that low-temperature hydrothermal fluids participated in the formation process, a fraction of the SiO_2 present could have formed hydrothermally from fluids rich in Si. Distinction of how much each of these possible sources contributed, is not possible due to recrystallisation. But it is a fair assumption that biogenic opal was the main contributor.

The anti-correlation of SiO_2 and the sum of REEs (Figure 4.3) in Group A and B-G-1 supports this assumption. Radiolarians and associated biogenic opal are the main source for SiO_2 , while terrigenous detritus and hydrothermal fluids as potential contributors are nearly insignificant. The main source

for SiO₂ thus does not carry significant amounts of REEs. They must stem from a different source. The REE pattern nearly perfectly matching shale (NASC and PAAS) hints towards terrigenous detritus as main source for the REEs instead of hydrothermal fluids.

Presence of mica “needles” Radiolarian ooze does not only contain radiolarian shells, but also significant amounts of pelagic clay minerals, and can contain terrigenous material, which can sometimes even be dominating (Fütterer, 2006). Clay minerals are hydrous aluminium phyllosilicates, and thus are a major carrier of Al within radiolarian ooze. The outcrops at all locations of Group A samples exhibited distinct layering of chert units and shale units, and even though only the chert units were sampled, the presence of clay minerals during deposition of the chert units is highly probable – albeit to a lesser extent. Clay minerals containing significant amounts of Al and other elements being present during the formation definitely influences the geochemistry of Group A samples significantly. The relatively high concentration of mica crystals in Group A samples can be linked to clay minerals having been present during deposition.

Hematite crystals and related layering Group A samples all exhibit, more or less distinct, parallel layering of hematite, with both gradual and abrupt changes in concentration. The presence of hematite indicates the presence of a Fe-rich component during deposition. The variation in hematite concentration within the layering can be caused either by changes in input concentration containing Fe, or by diagenetic processes. A definite answer has not been found for the samples thus far.

Group B - jasper

Presence of magnetite Magnetite is inferred to not have formed shortly after deposition of Fe-oxyhydroxides, but during a later process. Hematite is interpreted to be the primary Fe component in Group B, having crystallised from the Fe-oxyhydroxides. The magnetite crystals, mostly exhibiting idiomorphic crystal habits, likely formed during low-grade metamorphism, similar to early Cambrian exhalative ironstones investigated by Duhig, Stolz, Davidson and Large (1992). This assumption is based on the distribution of hematite and magnetite: where one component is dominating, the other is in the minority. Thus, reduction of hematite to magnetite took place, and magnetite formed at the expense of hematite. This reaction could have either been buffered by organic carbon as a reducing agent (Duhig, Stolz, Davidson and Large, 1992), or potentially even without a reducing agent present (Frost, 1979). Calcite veins, particularly described for B-G-1 (Figure 3.17d, page 56), associated with bigger magnetite crystal sizes, could potentially provide a reducing agent. Magnetite being present in all Group B samples can thus be taken as an indicator of low-grade metamorphism having affected the samples.

Clusters of “polygonal patches” The polygonal patches of hematite microspherules forming clusters, present in B-G-3a, -3b, and -4 (considerably less abundant in B-F-1), have been described before (e.g. Duhig, Davidson and Stolz, 1992, Duhig, Stolz, Davidson and Large, 1992, Rasmussen et al., 2014). Duhig, Davidson and Stolz (1992) found them in massive ferruginous chert, nearly pure chemical sediment, belonging to the Cambrian-Ordovician Mount Windsor volcanic belt (N Australia). Their formation is interpreted to be related to Si-Fe-oxyhydroxide gel deposition from hydrothermal fluids. These gels subsequently matured and crystallised, and along with this, the gel experienced syneresis, drying out and shrinking (Duhig, Davidson and

Stolz, 1992). This drying and shrinking is believed to be the cause for the clusters of polygonal patches; syneresis cracks silicified during diagenesis and left behind distinct textures (Figures 3.11c and 3.11d, page 48).

Duhig, Stolz, Davidson and Large (1992), investigating the same samples as Duhig, Davidson and Stolz (1992), found another possible explanation for the formation of these textures. Low-grade metamorphism could have led to recrystallisation of both silica and hematite, producing the clusters of polygonal patches. A connection is drawn between the formation of idiomorphic magnetite crystals and these patches: with increasing metamorphic grade, the magnetite crystals increase in size (Duhig, Stolz, Davidson and Large, 1992). Also, the absence of filamentous textures is explained by increasing metamorphic grade leading to the destruction of these textures, and recrystallisation of small hematite crystals present in the polygonal patches (Duhig, Stolz, Davidson and Large, 1992).

This explanation is incoherent with the findings of this study. B-F-1 is the only sample containing copious amounts of filamentous structures and also exhibits the largest idiomorphic magnetite crystals. Thus, low-grade metamorphism leading to magnetite formation is not believed to cause hematite filament destruction. According to this, filaments were not likely present in the samples exhibiting extensive abundances of clusters of polygonal patches. These textures can potentially better be explained as having formed from the syneresis of a gel precursor.

4.2.2 Group-overlapping traits and their implications

Presence of carbonate minerals The fact that idiomorphic to xenomorphic calcite crystals are present within all samples indicates that both Group A and Group B have been deposited above the carbonate compensation depth. This is in accordance with Group A samples having been deposited

in a widening back-arc basin setting, indicating that it was relatively shallow at the time of deposition. It also agrees with Group B having formed in a hydrothermal setting related to the formation of an immature island arc.

Filamentous structures In total, two samples contain filamentous structures: B-L-3, a radiolarian chert from Group A, and B-F-1, a jasper from Group B. The amount of filaments vary between both the samples, along with the size. B-L-3 only exhibits one small zone containing very few filamentous structures of lengths up to 350 μm and widths of 5 - 20 μm . B-F-1 has uncountable filament structures abundant in the hematite-rich zones, of average lengths of 30 - 100 μm and widths of 5 - 10 μm , though some are smaller (10 - 20 μm length, 2 - 4 μm width). Average lengths and widths of filaments produced by Fe(II)-oxidising bacteria described in literature are 10 - 100 μm and 1 - 5 μm , respectively (Little et al., 2004, and references therein). Slightly thicker filaments can be caused by subsequent precipitation of Fe oxides on the filaments, as described for modern hydrothermal deposits (Krepski et al., 2013, Chan et al., 2016, Lyngtveit, 2017).

Filamentous structures in B-L-3 are significantly longer than bacterial-derived filaments detected to date. This fact, the scarce abundance within the sample, and the fact that they have only been found in one out of five Group A samples, leads to the assumption that they might either potentially not be of biogenic origin, or bacterial activity was extremely restricted and scarce during formation. Nevertheless, there is still a possibility that filamentous textures have not been preserved through deformation and metamorphic alteration.

B-F-1 shows more similarities with filaments described for both modern hydrothermal deposits and ancient analogues. The crystallisation from Fe-oxyhydroxides to more crystalline phases and finally hematite, potentially overprinted by subsequent recrystallisation of hematite, causes issues in

recognising potential branching or other distinct features like twisted stalks that could be taken as a sound indicator for bacterial mediation. Nevertheless, the filamentous structures may have formed by Fe(II)-oxidising bacteria.

4.3 Formation models

Based on the geochemical and textural results and interpretations, the following models are assumed to represent the deposition of four different sample types:

- Bedded radiolarian chert (Group A)
- Radiolarian chert band (B-G-1, Group B)
- Abiogenic jasper (B-G-3a, -3b, and -4, Group B)
- Microbially induced jasper (B-F-1, Group B).

4.3.1 Bedded radiolarian chert (Group A)

The depositional regime of the radiolarian cherts comprising Group A inferred from geochemistry is interpreted to be a suboxic marginal back-arc basin, where terrigenous input was deposited among vast amounts of radiolarian shell remnants, with a small component providing pelagic clay mineral deposition (Figure 4.10). Rhythmic sediment input variations are potentially responsible for the macroscopically observed layering between formerly clay-rich units and chert-rich units in the outcrops. They can also be the cause for the gradual and abrupt changes in hematite concentrations within the chert layers. The terrigenous input provided stems from a landmass in vicinity to the basin, likely volcanic, explaining high Fe contents in the sediments. This terrigenous source is also the main contributor of REEs, due to the positive correlation of Fe and REEs (Figure 4.4, page 78). The main source for silica are radiolarian shell remnants, originally having consisted of biogenic

opal, which crystallised over time to SiO_2 . Pelagic clay might have played a minor role in the formation process, but it cannot be said with certainty. Positive Ce anomalies are the result of a minor uptake of REEs from the seawater, which is interpreted as suboxic. Whether a hydrothermal component provided to the formation of the radiolarian cherts is unclear, but if it did, the effect might have been negligibly small. Significant recrystallisation must have taken place, since no clear textural evidence can be found for terrigenous detritus, except for one quartz grain found in B-L-1 (Figure 3.7, page 42). Additionally the REE patterns, Al, Ti, and a range of other elements support the theory of terrigenous detritus being present. Next to the radiolarian shell remnants having been affected by thermal maturation, hematite crystals are assumed to have formed during recrystallisation. The samples have not been exposed to high-grade metamorphism and the layering is believed to stem from varying sediment input rates.

The bedded radiolarian cherts cannot be taken as a good analogue for modern submarine hydrothermal Fe-Si-deposits, due to the uncertainty regarding a hydrothermal component.

4.3.2 Radiolarian chert band (B-G-1, Group B)

Strong similarities in mineralogy, geochemistry, and texture shared with Group A (bedded radiolarian cherts) indicates that B-G-1 has a similar formation history with minimal differences (Figure 4.11). Terrigenous input, likely volcanic, is derived from a nearby landmass, and provides mainly Fe and REEs to the system, while the silica is mainly derived from radiolarian shell remnants and their biogenic opal. A minimal input of pelagic clay minerals is possible. Low-temperature hydrothermal fluids contributing to Fe, Si, and REE input are possible, but this cannot be said with certainty. Oxygen concentrations are interpreted to have been low during deposition,

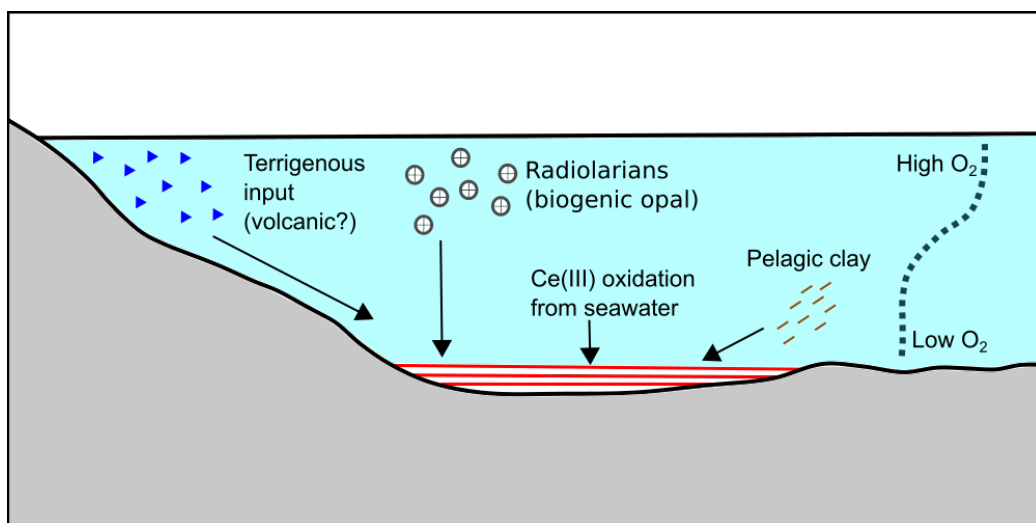


Figure 4.10: Formation model for bedded radiolarian cherts (Group A)

leading to minimal Ce(III) oxidation. An additional source of Fe is likely, as compared to Group A radiolarian cherts, which only show one main Fe source. Low-grade metamorphism is believed to have caused reduction of hematite to magnetite, while keeping the layering within the sample intact. Only one thin layer of hematitic chert developed, unlike the radiolarian cherts of Group A, which are pervasively bedded.

The uncertainty about a hydrothermal component contributing to the formation of the radiolarian chert band complicates the samples' ability to serve as analogues to modern submarine hydrothermal Fe-Si-deposits.

4.3.3 Abiogenic jasper (B-G-3a, -3b, and -4, Group B)

B-G-3a, -3b, and B-G-4 all have very similar textural traits, most notably the polygonal patches interpreted to be syneresis cracks indicating a gel precursor. A possible explanation for their formation is low-temperature hydrothermal fluids, having formed due to conductive heating of downwards percolating seawater below the seafloor surface, leading to their production

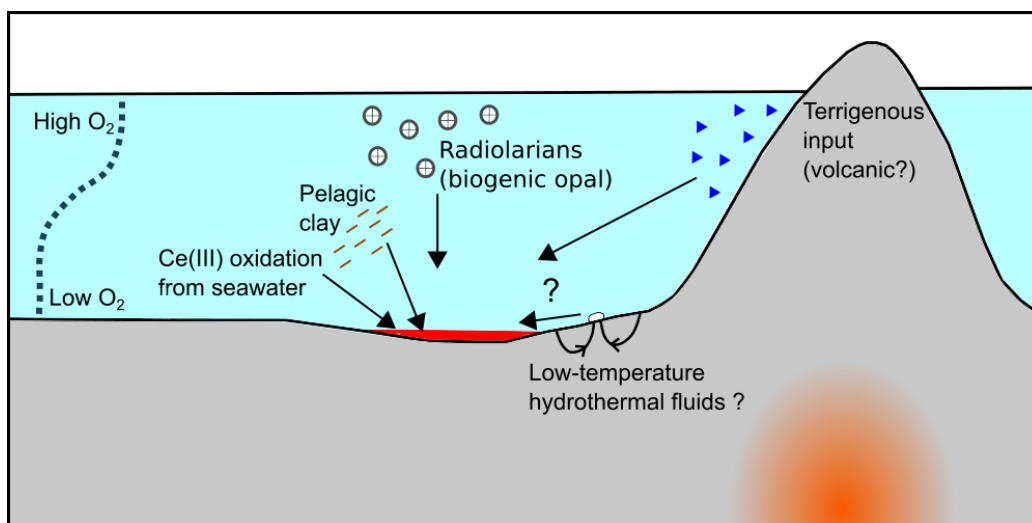


Figure 4.11: Formation model for radiolarian chert band (B-G-1)

(Cooper et al., 2000). Buoyancy led to their emanation from the seafloor, where they subsequently only slowly mixed with seawater (Figure 4.12). Hydrothermal fluids are denser than seawater (Sato, 1972), and thus, if emanating diffusely from the seafloor, they do not spread far, but likely form a Fe-Si-oxyhydroxide gel layer on the seafloor. Vast subsurface formation is unlikely due to the O_2 concentration rapidly decreasing with increasing depth. The absence of biomarkers such as microbial filamentous structures seen in B-F-1 indicates either their later destruction by metamorphism or the absence of bacteria during the formation process. Idiomorphic magnetite signals metamorphism having affected the samples, but B-F-1 contains both idiomorphic magnetite and filamentous structures. This leads to the assumption that B-G-3a, -3b, and -4 likely did not contain microbial filaments in the first place. The absence of bacteria producing filamentous structures might be explained with temperatures of the low-temperature hydrothermal fluids having been too high to host Fe(II)-oxidising bacteria. For *Mariprofundus ferrooxydans*, experimentally determined optimal growth temperatures range

between 10 - 30 °C (Emerson et al., 2007), while low-temperature hydrothermal fluid temperatures reach temperatures up to 100 °C (e.g. Bemis et al., 2012). Other Fe(II)-oxidisers likely have similar growth temperature ranges. This supports the theory of temperatures having been too high for microbial activity to contribute to the formation of the abiogenic jasper. Slightly positive Ce anomalies and negative Eu anomalies (chondrite-normalised) indicate uptake of REEs mainly from low-temperature hydrothermal fluids by Fe-oxyhydroxides having precipitated abiogenically and not mediated by bacterial activity. During thermal maturation of the gel, syneresis cracks formed, creating the characteristic clusters of polygonal patches. Later on, silica filled these cracks. Magnetite formed from hematite during low-grade metamorphism.

Abiogenic jasper can potentially serve as an analogue to modern submarine hydrothermal Fe-Si-deposits, but no comparable samples within modern seafloor hydrothermal systems have yet been described.

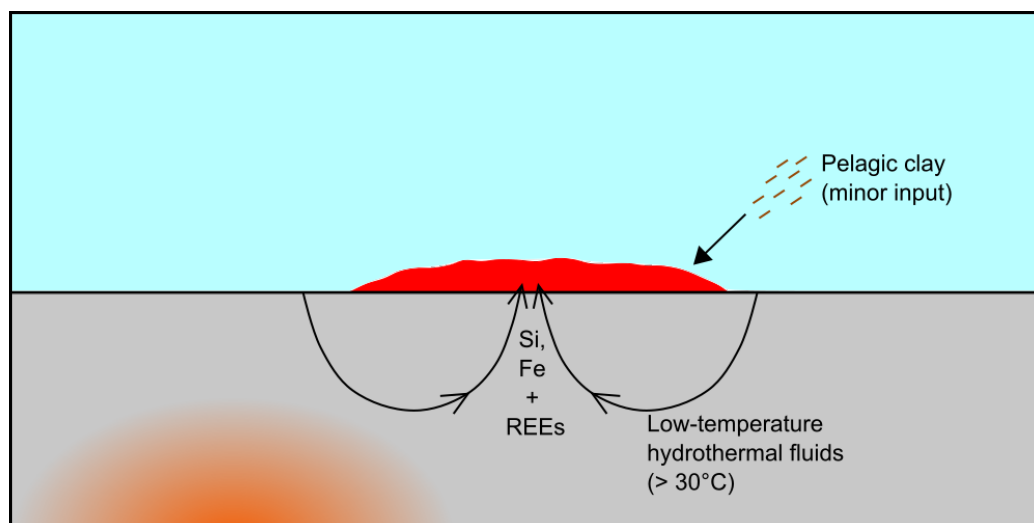


Figure 4.12: Formation model for abiogenic jasper (B-G-3a, -3b, -4)

4.3.4 Microbially induced jasper (B-F-1, Group B)

B-F-1 differs in texture from the rest of Group B, and thus must have a different formation (Figure 4.13). The sample exhibits a high amount of filaments, leading to the assumption that microbial activity is the driving force for the precipitation of Fe-oxyhydroxides, the hematite precursor. The combination of negative Ce and Eu anomalies (normalised to chondrite) is only found within this one sample. This is typical for modern Fe-oxyhydroxide deposits found within the Jan Mayen hydrothermal vent field (Johannessen et al., 2017, Haukelidsæter, 2017, Lyngtveit, 2017), which are attributed to diffuse low-temperature hydrothermal venting. These deposits are dominated by filaments produced by bacteria, texturally resembling the filaments found in B-F-1. The similarities in geochemistry and texture indicate that these modern hydrothermal deposits can be seen as an analogue to sample B-F-1. Seawater is interpreted to have percolated seafloor sediments only shallowly and was conductively heated by a heat source below, leading to low-temperature hydrothermal fluids (Johannessen et al., 2017). These fluids were then driven upwards and when diffusely venting from the seafloor sediments, Fe-oxidising bacteria were able to use the redox-potential for their metabolism. This can be inferred to have led to the formation of filaments comprised of Fe-oxyhydroxides, in a similar manner as in modern Fe-oxyhydroxide deposits from the Jan Mayen Vent Field, forming mounds and creating Fe and O₂ gradients between inside and outside (Johannessen et al., 2017). Silica also precipitated from the hydrothermal fluids. Layering can be observed in the thin section scan of B-F-1 (Figure 3.9e, page 45), potentially created by cycles of high hydrothermal fluid input vs. low input, resulting in phases of intense microbially induced Fe-oxyhydroxide precipitation and quiescent phases. The fact that not all hematite crystals present today exhibit filamentous structures can be explained by additional abiogenic precipitation of

Fe-oxyhydroxides. The unstable Fe-oxyhydroxides crystallised to hematite during diagenesis, while their original shape was mostly maintained. During low-grade metamorphism, magnetite formed from hematite.

Microbially induced jasper formed as interpreted here (Figure 4.13) can likely serve as ancient analogue to findings in the modern Fe-deposits from the low-temperature dominated Jan Mayen Vent field described by Johannessen et al. (2017), Haukelidsæter (2017), and Lyngtveit (2017).

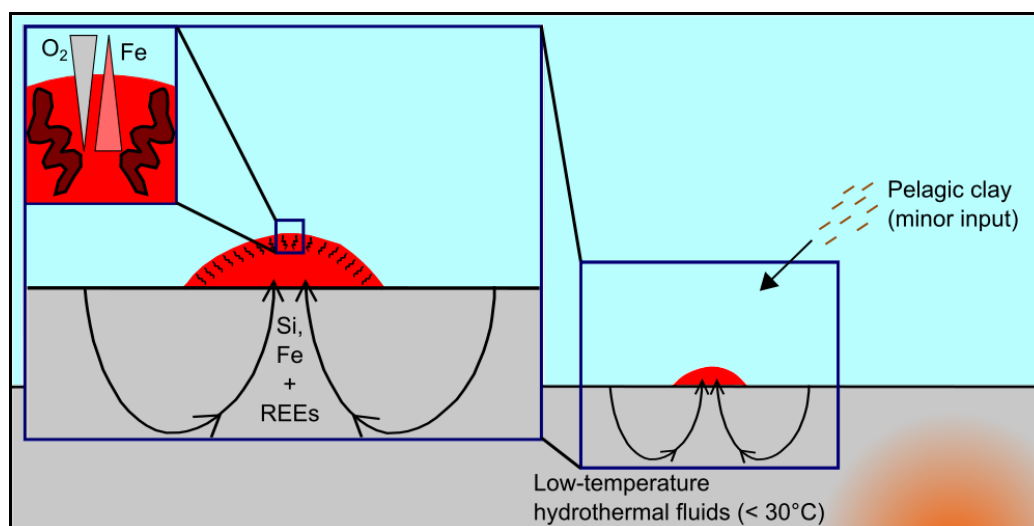


Figure 4.13: Formation model for microbially induced jasper (B-F-1)

4.4 Contributions of findings to the regional geology

Group B samples belonging to the Geitung Unit

The geochemistry of abiogenic and microbially induced jasper indicates an origin in a seafloor hydrothermal system hosting low-temperature hydrothermal fluids. No evidence can be found for terrigenous detritus affecting the

jaspers, thus they are interpreted to have formed in a marine setting distal to continental margins. Their presence as clasts within volcanic basement rock breccia (on Geitung) and basal conglomerate consisting of volcanic rocks (by Finnås) indicates rearrangement of the initially horizontally deposited jaspers. This rearrangement caused the formation of talus deposits from debris flows of fault scarps along the seafloor.

The radiolarian chert band deposited within metasandstone (on Geitung) can be interpreted to have formed during a quiescent phase unaffected by debris flows on the seafloor. Radiolarian shell remnants deposited within this chert band support this assumption. Volcaniclastic material is interpreted to vastly have contributed to the samples' REE and Fe composition. Presence of hydrothermal activity is uncertain but cannot be excluded as additional factor.

The Geitung Unit is interpreted as an immature island arc having formed during the late Cambrian, ca. 494 Ma (Brekke et al., 1984, Pedersen and Dunning, 1997). Mineral deposits within the Geitung Unit (e.g. sulphides and copper, R.B. Pedersen, personal communication, November 2017) indicate hydrothermal activity, and the presence of jaspers exhibiting geochemical traits typical for low-temperature hydrothermal deposits is in accordance with this. Detrital zircons from a sedimentary sequence (Viken, 2017) exhibit the same age as basaltic-andesites investigated by Pedersen and Dunning (1997), indicating no terrigenous sources contributing detrital material, only adjacent, coeval volcanics. Thus, the Geitung Unit developed far away from continental margins (Viken, 2017). Both the lack of terrigenous detritus affecting the geochemistry of the jaspers, and only volcaniclastic material contributing to the geochemistry of the radiolarian chert band can be taken as sound indicators for the immature island arc having developed unaffected by sediments from continental margins.

Group A samples belonging to the Langevåg Group

The bedded radiolarian cherts do not display geochemical or textural traits typical for hydrothermal deposits. Texturally, the presence of radiolarian shell remnants indicate the main silica source originally having been biogenic opal. The cherts' geochemistry exhibits remarkable similarities with terrigenous material rich in Fe, thus leading to the assumption that volcanoclastic material contributed strongly to the formation. Recrystallisation hid potential textural traces of the volcanoclastic material, but the geochemical evidence is distinct. Suboxic conditions are inferred to have been present in the depositional environment.

The Langevåg Group has been indirectly dated at ca. 470 Myr (Pedersen and Dunning, 1997), and it has been interpreted that the sediments were deposited within a widening and subsequently deepening marginal back-arc basin (Brekke et al., 1984, Sivertsen, 1992, Pedersen et al., 1992, Pedersen and Dunning, 1997). The inferred suboxic conditions present during bedded radiolarian chert formation are in accordance with this interpretation. Sivertsen (1992) presents evidence for volcanoclastic material deposited within this basin to originate from the Siggjo Complex, a mature island arc which evolved from the Geitung Unit immature island arc complex and was dated at ca. 743 Myr (Pedersen and Dunning, 1997). The geochemical evidence of volcanoclastic material contributing to the formation of the bedded radiolarian cherts is in agreement with interpretations of Sivertsen (1992).

5 Conclusions & Outlook

After thorough investigation of the hematitic chert samples from Bømlo and Stord, the aims of the study have been addressed in a detailed manner and conclusions can be made.

Conditions and processes leading to different hematitic chert types

Using the geochemical, mineralogical, and textural evidence presented and discussed in this study, four different types of hematitic chert from Bømlo and Stord (SW Norway) have been defined. These are interpreted to have formed in four different processes under varying conditions.

Bedded radiolarian chert All samples from Stord and from Langevag (Bømlo) exhibit the same traits and are interpreted to have formed in a widening back-arc basin populated by radiolarians, with adjacent (likely volcanic) landmasses. Radiolarian shell remnants provide biogenic opal, whereas terrigenous detritus is the main source for REEs and most of the remaining elements. Suboxic seawater contributes, to a minor extent, to the REE concentrations. Pelagic clay plays a minor role, and a low-temperature hydrothermal component is possible, but cannot be defined with certainty. Thermally induced crystallisation of biogenic opal to quartz goes along with recrystallisation of detrital input, and variable concentrations of different input sources lead to the observed layering. The same processes occurring over a long period of time are interpreted to have formed the extensive bedded chert units.

Radiolarian chert band One sample from Geitung (Bømlo, B-G-1) shows remarkable resemblance with the bedded radiolarian cherts, but exhibits much lower concentrations in REEs. Additionally, it comprises a band only a few cm thick, not a several dozens of metres thick bedded chert unit. Processes leading to its formation are believed to be similar, with the exception that they are interpreted to have occurred in a slightly different setting. A setting such as that found at the base of a volcanic landmass, with low-temperature hydrothermal fluids potentially providing additional input, is assumed. The occurrence as a thin radiolarian chert band can be interpreted to having been caused by processes not stable for a long time, as for the bedded radiolarian cherts.

Abiogenic jasper Three samples from Geitung (Bømlo; B-G-3a, -3b, -4) look very much alike. They are interpreted to have formed on the seafloor, distal to landmasses and thus virtually unaffected by terrigenous detritus. Low-temperature hydrothermal fluids diffusely emanating from the seafloor likely formed a gel precursor, with temperatures too high to sustain Fe(II)-oxidising bacteria due to the absence of textures indicating microbial participation. Here, it is interpreted that abiogenic Fe-Si-oxyhydroxide formation took place without major oxic to suboxic seawater contributions. Later re-arrangement of the sediments led to the formation of clasts found today in volcanic breccia.

Microbially induced jasper The sample from Finnås (Bømlo, B-F-1) shows macroscopic resemblance with the abiogenic jasper from Geitung, but differs texturally and geochemically. A similar formation environment is interpreted: low-temperature hydrothermal fluids diffusely emanated from the seafloor, and dome-shaped structures were formed, surrounded by oxic to suboxic seawater. Temperatures here are interpreted to have been more appropriate for Fe(II)-oxidisers. Microbially induced growth of filaments (becoming encrusted in Fe-Si-oxyhydroxides within the dome-shaped structures

due to O₂- and Fe(II)-gradients favourable for Fe(II)-oxidisers) is assumed to be responsible for the formation of this type of jasper. Similar to the abiogenic jasper clasts, the microbially induced jasper must have been fragmented and redeposited after formation, leading to its' presence as clasts within basal conglomerate.

Ancient analogue to modern Fe-deposits in hydrothermal systems?

The radiolarian cherts (Group A, and B-G-1 from Group B) are not ancient analogues to modern Fe-deposits in seafloor hydrothermal systems. Abiogenic jasper (B-G-3a, -3b, and -4, Group B) can theoretically serve as an analogue, but no comparable modern seafloor hydrothermal Fe-deposits have been detected to date. Microbially induced jasper (B-F-1, Group B), on the other hand, can likely serve as ancient analogue to modern Fe-deposits formed in low-temperature hydrothermal vent settings as within the Jan Mayen vent fields (Johannessen et al., 2017, Haukelidsæter, 2017, Lyngtveit, 2017).

Contributions to a better understanding of the regional geology

The Geitung Unit jasper proves the existence of seafloor hydrothermal systems present during the formation of a late Cambrian immature island arc. Geochemical evidence supports the findings of Viken (2017), implying the arc formation occurred distal to continental margins. The Langevåg Group bedded radiolarian cherts exhibit geochemical evidence for volcanoclastic material substantially having contributed to their formation. According to Sivertsen (1992), volcanoclastic material deposited in the widening back-arc basin (Lower/Middle Ordovician) originated from the adjacent Siggjo Complex volcanics. While no supplemental evidence can be added to this theory, a volcanoclastic source for the terrigenous material is highly likely. Thus, the results of this study are in accordance with the findings of Sivertsen (1992).

Outlook

Several questions arose during research, to which detailed answers could not be found within the scope of this thesis. The role hydrothermal fluids played in the formation of the late Cambrian radiolarian chert band was not unanimously resolved. Further research to determine a hydrothermal contribution is necessary to provide a more profound understanding of marine sediments deposited during the Geitung Unit immature island arc formation. Modern abiogenic Fe-deposits can be investigated, with regard to the suggested formation model for the jasper interpreted to have formed via abiogenic precipitation. Other processes leading to this type of jasper can potentially be detected in future studies. Additionally, following the suggestion by Johannessen et al. (2017) to implement chondrite-normalised values for jasper REE analyses, it became obvious during this study that using shale normalisations can yield positive Eu anomalies in some cases, while chondrite-normalised Eu anomalies are negative. The shale-normalised positive Eu anomalies easily lead to questionable assumptions regarding the temperature of hydrothermal source fluids. For future work conducted on jasper samples, chondrite normalisation for evaluating hydrothermal processes is recommended, and previous geochemical analyses could potentially be re-evaluated with respect to this. The “depositional environment”-classification diagram for cherts (Figure 4.8) developed by Murray (1994) can probably be enhanced by adding a new field for jaspers having formed from low-temperature hydrothermal fluids in seafloor hydrothermal systems distal to continental margins. Further research and evaluation of more jaspers is necessary to reinforce the enhancement of the classification diagram.

Bibliography

- Adachi, M., Yamamoto, K. and Sugisaki, R. (1986), 'Hydrothermal chert and associated siliceous rocks from the Northern Pacific: their geological significance as indication of ocean ridge activity', *Sedimentary Geology* **47**, 125–148.
- Alt, J. (1988), 'Hydrothermal oxide nontronite deposits in the eastern Pacific', *Marine Geology* **81**, 221–239.
- Alt, J. (1995), Subseafloor processes in mid-ocean ridge hydrothermal systems, *in* S. E. Humphris, R. A. Zierenberg, L. S. Mullineaux and R. E. Thomson, eds, 'Seafloor Hydrothermal Systems: Physical, Chemical, Biological, and Geological Interactions', Vol. 91 of *AGU Monograph Series*, American Geophysical Union, pp. 85–114.
- Andersen, T. B. and Andresen, A. (1994), 'Stratigraphy, tectonostratigraphy and the accretion of outboard terranes in the Caledonides of Sunnhordland, W. Norway', *Tectonophysics* **231**, 71–84.
- Andersen, T. B. and Jansen, Ø. J. (1987), 'The Sunnhordland Batholith, W. Norway: Regional setting and internal structure, with emphasis on the granitoid plutons', *Norsk Geologisk Tidsskrift* **67**, 159–183.
- Banfield, J. F., Welch, S. A., Zhang, H., Ebert, T. T. and Penn, R. L. (2000),

- ‘Aggregation-based crystal growth and microstructure development in natural iron oxyhydroxides biomineralization products’, *Science* **289**, 751–754.
- Bau, M. and Dulski, P. (1996), ‘Distribution of yttrium and rare-earth elements in the Penge and Kuruman iron-formations, Transvaal Supergroup, South Africa’, *Precambrian Research* **79**, 37–55.
- Bekker, A., Slack, J. F., Planavsky, N., Krapež, B., Hofmann, A., Konhauser, K. O. and Rouxel, O. J. (2010), ‘Iron Formation: The Sedimentary Product of a Complex Interplay among Mantle, Tectonic, Oceanic, and Biospheric Processes’, *Economic Geology* **105**, 467–508.
- Bemis, K., Lowell, R. P. and Farough, A. (2012), ‘Diffuse flow on and around hydrothermal vents at mid-ocean ridges’, *Oceanography* **25**(1), 182–191.
- Bingen, B. and Solli, A. (2009), ‘Geochronology of magmatism in the Caledonian and Sveconorwegian belts of Baltica: synopsis for detrital zircon provenance studies’, *Norwegian Journal of Geology* **89**, 267–290.
- Bolhar, R., Van Kranendonk, M. J. and Kamber, B. S. (2005), ‘A trace element study of siderite-jasper banded iron formation in the 3.45 Ga Warrawoona Group, Pilbara Craton - Formation from hydrothermal fluids and shallow seawater’, *Precambrian Research* **137**, 93–114.
- Bonatti, E., Kraemer, T. and Rydell, H. (1972), Classification and genesis of submarine iron-manganese deposits, in D. R. Horn, ed., ‘Ferromanganese Deposits on the Ocean Floor’, Aren House, Harriman, pp. 149–166.
- Boström, K. and Pederson, M. N. A. (1969), ‘The origin of aluminum-poor ferromanganoan sediments in areas of high heat-flow on the East Pacific Rise’, *Marine Geology* **7**, 427–447.

- Boyd, T. D. and Scott, S. D. (2001), 'Microbial and hydrothermal aspects of ferric oxyhydroxides and ferrosic hydroxides: the example of Franklin Seamount, Western Woodlark Basin, Papua New Guinea', *Geochemical Transactions* **2**, 45–56.
- Boynton, W. V. (1984), Cosmochemistry of the rare earth elements: meteorite studies, in P. Henderson, ed., 'Rare Earth Element Geochemistry', Elsevier, Amsterdam, pp. 63–114.
- Braun, A., Chen, J., Waloszek, D. and Maas, A. (2007), 'First Early Cambrian Radiolaria', *Geological Society, London, Special Publications* **286**, 143–149.
- Brekke, H., Furnes, H., Nordås, J. and Hertogen, J. (1984), 'Lower Palaeozoic convergent plate margin volcanism on Bømlo, SW Norway, and its bearing on the tectonic environments of the Norwegian Caledonides', *Journal of the Geological Society* **141**(6), 1015–1032.
- Campbell, A. S. (1952), 'An Introduction to the Study of the Radiolaria', *The Micropaleontologist* **6**(2), 29–44.
- Chan, C. S., Fakra, S. C., Emerson, D., Fleming, E. J. and Edwards, K. J. (2011), 'Lithotrophic iron-oxidizing bacteria produce organic stalks to control mineral growth: implications for biosignature formation', *The International Society for Microbial Ecology Journal* **5**, 717–727.
- Chan, C. S., McAllister, S. M., Leavitt, A. H., Glazer, B. T., Krepski, S. T. and Emerson, D. (2016), 'The architecture of iron microbial mats reflects the adaptation of chemolithotrophic iron oxidation in freshwater and marine environments', *Frontiers in Microbiology* **7**, 1–18.
- Cooper, M. J., Elderfield, H. and Schultz, A. (2000), 'Diffuse hydrothermal fluids from Lucky Strike hydrothermal vent field: Evidence for a

- shallow conductively heated system', *Journal of Geophysical Research* **105**(B8), 19369–19375.
- Corfu, F., Andersen, T. B. and Gasser, D. (2014), 'The Scandinavian Caledonides: main features, conceptual advances and critical questions', *Geological Society, London, Special Publications* **390**, 9–43.
- Corfu, F., Roberts, R. J., Torsvik, T. H., Ashwal, L. D. and Ramsay, D. M. (2007), 'Peri-Gondwanan elements in the Caledonian nappes of Finnmark, Northern Norway: Implications for the paleogeographic framework of the Scandinavian Caledonides', *American Journal of Science* **307**, 434–458.
- Corliss, J. B. (1971), 'The origin of metal-bearing submarine hydrothermal solutions', *Journal of Geophysical Research* **76**, 8128–8138.
- Corliss, J. B. (1979), 'Submarine thermal springs on the Galápagos Rift', *Science* **203**, 1073–1083.
- CYAMEX Scientific Team (1979), 'Massive deep-sea sulfide ore deposits discovered on the East Pacific Rise', *Nature* **277**, 523–528.
- Davidson, G. J., Stolz, A. J. and Eggins, S. M. (2001), 'Geochemical Anatomy of Silica Iron Exhalites: Evidence for Hydrothermal Oxyanion Cycling in Response to Vent Fluid Redox and Thermal Evolution (Mt. Windsor Subprovince, Australia)', *Economic Geology* **96**, 1201–1226.
- De Wever, P., Dumitrica, P., Caulet, J. P., Nigrini, C. and Caridroit, M. (2001), *Radiolarians in the Sedimentary Record*, 1 edn, Gordon and Breach Science Publishers.
- Dick, G. J., Anantharaman, K., Baker, B. J., Li, M., Reed, D. C. and Sheik, C. S. (2013), 'The microbiology of deep-sea hydrothermal vent plumes: ecological and biogeographic linkages to seafloor and water column habitats', *Frontiers in Microbiology* **4**, 1–16.

- Dodd, M. S., Papineau, D., Grenne, T., Slack, J. F., Rittner, M., Pirajno, F., O'Neil, J. and Little, C. T. S. (2017), 'Evidence for early life in Earth's oldest hydrothermal vent precipitates', *Nature* **543**, 60–64.
- Duhig, N. C., Davidson, G. J. and Stolz, J. (1992), 'Microbial involvement in the formation of Cambrian sea-floor silica-iron oxide deposits, Australia', *Geology* **20**, 511–514.
- Duhig, N. C., Stolz, J., Davidson, G. J. and Large, R. R. (1992), 'Cambrian microbial and silica gel textures in silica iron exhalites from the Mount Windsor Volcanic Belt, Australia: their petrography, chemistry, and origin', *Economic Geology* **87**, 764–784.
- Elderfield, H. (1988), 'The oceanic chemistry of the rare earth elements', *Philosophical Transactions of the Royal Society of London, Series A* **325**, 105–126.
- Emerson, D. and Moyer, C. L. (2002), 'Neutrophilic Fe-Oxidizing Bacteria Are Abundant at the Loihi Seamount Hydrothermal Vents and Play a Major Role in Fe Oxide Deposition', *Applied and Environmental Microbiology* **68**(6), 3085–3093.
- Emerson, D., Rentz, J. A., Lilburn, T. G., Davis, R. E., Aldrich, H., Chan, C. S. and Moyer, C. L. (2007), 'A Novel Lineage of Proteobacteria Involved in Formation of Marine Fe-Oxidising Microbial Mat Communities', *PLOS ONE* **2**, e667.
- Emerson, D. and Revsbech, N. P. (1994), 'Investigation of an Iron-Oxidising Microbial Mat Community Located near Aarhus, Denmark: Laboratory Studies', *Applied and Environmental Microbiology* **60**(11), 4032–4038.

- Færseth, R. B. (1982), 'Geology of southern Stord and adjacent islands, southwest Norwegian Caledonides', *Norges Geologiske Undersøkelse* **371**, 57–112.
- Falkowski, P. G. (2012), The Global Carbon Cycle: Biological Processes, *in* A. H. Knoll, D. E. Canfield and K. O. Konhauser, eds, 'Fundamentals of Geobiology', Blackwell Publishing Ltd, chapter 2, pp. 5–19.
- Fisher, A. T. (1998), 'Permeability within basaltic oceanic crust', *Reviews of Geophysics* **36**(2), 143–182.
- Fossen, H. (1992), 'The role of extensional tectonics in the Caledonides of south Norway', *Journal of Structural Geology* **14**(8-9), 1033–1046.
- Fossen, H. (2010), Extensional tectonics in the North Atlantic Caledonides: a regional view, *in* R. D. Law, R. W. H. Butler, R. E. Holdsworth, M. Krabbendam and R. A. Strachan, eds, 'Continental Tectonics and Mountain Building: The Legacy of Peach and Horne', Vol. 335, Geological Society London, pp. 767–793.
- Fossen, H. and Hurich, C. A. (2005), 'The Hardangerfjord Shear Zone in SW Norway and the North Sea: a large scale shear zone in the Baltic crust', *Journal of the Geological Society, London* **162**, 675–687.
- Frost, R. B. (1979), 'Metamorphism of iron-formation: Parageneses in the system Fe-Si-C-O-H', *Economic Geology* **74**, 775–785.
- Furnes, H., Austrheim, H., Amalixsen, K. G. and Nordås, J. (1983), 'Evidence for an incipient early Caledonian (Cambrian) orogenic phase in southwestern Norway', *Geological Magazine* **120**, 607–612.
- Furnes, H., Brekke, H., Nordås, J. and Hertogen, J. (1986), 'Lower Palaeozoic convergent plate margin volcanism on Bømlo, southwest Norwe-

- gian Caledonides: geochemistry and petrogenesis', *Geological Magazine* **123**(2), 123–142.
- Fütterer, D. K. (2006), The Solid Phase of Marine Sediments, *in* H. D. Schulz and M. Zabel, eds, 'Marine Geochemistry', 2 edn, Springer Verlag, chapter 1, pp. 1–25.
- Gee, D. G. (1975), 'A tectonic model for the central part of the Scandinavian Caledonides', *American Journal of Science* **275**, 468–515.
- German, C. R. and Elderfield, H. (1990), 'Application of the Ce anomaly as a paleoredox indicator: the ground rules', *Paleoceanography* **5**, 823–833.
- German, C. R., Holliday, B. P. and Elderfield, H. (1991), 'Redox cycling of rare earth elements in the suboxic zone of the Black Sea', *Geochimica et Cosmochimica Acta* **55**, 3553–3558.
- German, C. R., Klinkhammer, G., Edmond, J. M., Mitra, A. and Elderfield, H. (1990), 'Hydrothermal scavenging of rare-earth elements in the ocean', *Nature* **346**, 516–518.
- Grenne, T. and Slack, J. F. (2003a), 'Bedded jaspers of the Ordovician Løkken ophiolite, Norway: seafloor deposition and diagenetic maturation of hydrothermal plume-derived silica-iron gels', *Mineralium Deposita* **38**, 625–639.
- Grenne, T. and Slack, J. F. (2003b), 'Paleozoic and Mesozoic silica-rich seawater: Evidence from hematitic chert (jasper) deposits', *Geology* **31**(4), 319–322.
- Grenne, T. and Slack, J. F. (2005), 'Geochemistry of Jasper Beds from the Ordovician Løkken ophiolite, Norway: Origin of Proximal and Distal Siliceous Exhalites', *Economic Geology* **100**(8), 1511–1527.

- Gromet, L. P., Dymek, R. F., Haskin, L. A. and Korotev, R. L. (1984), 'The "North American shale composite": Its compilation, major, and trace element characteristics', *Geochimica et Cosmochimica Acta* **48**, 2469–2482.
- Hacker, B. R. and Gans, P. B. (2005), 'Continental collisions and the creation of ultrahigh-pressure terranes: Petrology and thermochronology of nappes in the central Scandinavian Caledonides', *GSA Bulletin* **117**(1/2), 117–134.
- Hallbeck, L. and Pedersen, K. (1991), 'Autotrophic and mixotrophic growth of *Gallionella ferruginea*', *Journal of General Microbiology* **137**, 2657–2661.
- Haukelidsæter, S. (2017), Textural and geochemical characteristics of iron deposits at the Jan Mayen vent fields: implications for formation mechanisms, Master's thesis, University of Bergen.
- Hein, J. R., Scholl, D. W., Barron, J. A., Jones, M. G. and Miller, J. (1978), 'Diagenesis of late Cenozoic diatomaceous deposits and formation of the bottom simulation reflector in the southern Bering Sea', *Sedimentology* **25**, 155–181.
- Hein, J. R., Schulz, M. S. and Gein, L. M. (1992), Central Pacific cobalt-rich ferromanganese crusts: Historical perspective and regional variability, in B. H. Keating and B. R. Bolton, eds, 'Geology and Offshore Mineral Resources of the Central Pacific Basin', Springer Verlag, pp. 261–283.
- Hein, J. R., Yeh, H.-W., Gunn, S. H., Gibbs, A. E. and Wang, C.-H. (1994), 'Composition and origin of hydrothermal ironstones from Central Pacific seamounts', *Geochimica et Cosmochimica Acta* **58**, 179–189.
- Hekinian, R., Hoffert, M., Larqué, P., Cheminée, J. L., Stoffers, P. and Bideau, D. (1993), 'Hydrothermal Fe and Si Oxyhydroxide Deposits from

- South Pacific Intraplate Volcanoes and East Pacific Rise Axial and Off-Axial Regions', *Economic Geology* **88**, 2099–2121.
- Hofmann, B. A. and Farmer, J. D. (2000), 'Filamentous fabrics in low-temperature mineral assemblages: are they fossil biomarkers? Implications for the search for a subsurface fossil record on the early Earth and Mars', *Planetary and Space Science* **48**, 1077–1086.
- InterRidge (2017), 'InterRidge Vents Database Ver. 3.4'.
URL: <http://vents-data.interridge.org/> [Accessed: 16.11.17]
- Johannessen, K. C., Vander Roost, J., Dahle, H., Dundas, S. H., Pedersen, R. B. and Thorseth, I. H. (2017), 'Environmental controls on biomineralization and Fe-mound formation in a low-temperature hydrothermal system at the Jan Mayen Vent Fields', *Geochimica et Cosmochimica Acta* **202**, 101–123.
- Jones, D. L. and Murchey, B. (1986), 'Geologic significance of Paleozoic and Mesozoic radiolarian chert', *Annual Review of Earth and Planetary Sciences* **14**, 455–492.
- Jones, D. L. and Segnet, E. R. (1972), 'Genesis of cristobalite and tridymite at low temperatures', *Journal of the Geological Society of Australia* **18**, 419–422.
- Juniper, S. K. and Fouquet, Y. (1988), 'Filamentous iron-silica deposits from modern and ancient hydrothermal sites', *Canadian Mineralogist* **26**, 859–869.
- Karl, D. M., McMurty, G. M., Malahoff, A. and Garcia, M. O. (1988), 'Loihi Seamount, Hawaii: a mid-plate volcano with a distinctive hydrothermal system', *Nature* **335**, 532–535.

- Kastner, M., Keene, J. B. and Gieskes, J. M. (1977), 'Chemical controls on the rate of opal-A to opal-CT transformation – experimental study. Part 1 of Diagenesis of siliceous oozes', *Geochimica et Cosmochimica Acta* **41**, 1041–1059.
- Konhauser, K. O. (2007a), *Introduction to Geomicrobiology*, Blackwell Science Ltd, chapter 2: Microbial metabolism.
- Konhauser, K. O. (2007b), *Introduction to Geomicrobiology*, Blackwell Science Ltd, chapter 4: Biomineralization.
- Krepeski, S. T., Emerson, D., Hredzak-Showalter, P. L., Luther III, G. W. and Chan, C. S. (2013), 'Morphology of biogenic iron oxides records microbial physiology and environmental conditions: toward interpreting iron microfossils', *Geobiology* **11**, 457–471.
- Langmuir, C., Humphris, S., Fornari, D., Van Dover, C., Von Damm, K., Tivey, M. K., Colodner, D., Charlou, J.-L., Desonie, D., Wilson, D., Fouquet, Y., Klinkhammer, G. and Bougault, H. (1997), 'Hydrothermal vents near a mantle hot spot: The Lucky Strike vent field at 37°N on the Mid-Atlantic Ridge', *Earth and Planetary Science Letters* **148**, 68–91.
- Leistel, J. M., Marcoux, E. and Deschamps, Y. (1998), 'Chert in the Iberian Pyrite Belt', *Mineralium Deposita* **33**, 59–81.
- Li, J., Zhou, H., Peng, X., Wu, Z., Chen, S. and Fang, J. (2012), 'Microbial diversity and biomineralization in low-temperature hydrothermal iron-rich precipitates of the Lau Basin hydrothermal field', *FEMS Microbiology Ecology* **81**(1), 205–216.
- Little, C. T. S., Glynn, S. E. J. and Mills, R. A. (2004), 'Four-Hundred-and-Ninety-Million-Year Record of Bacteriogenic Iron Oxide Precipitation at Sea-Floor Hydrothermal Vents', *Geomicrobiology Journal* **21**(6), 415–429.

- Little, C. T. S. and Thorseth, I. H. (2002), 'Hydrothermal vent microbial communities: a fossil perspective', *Cahiers De Biologie Marine* **43**, 317–319.
- Lowell, R. P., Rona, P. A. and Von Herzen, R. P. (1995), 'Seafloor hydrothermal systems', *Journal of Geophysical Research* **100**(B1), 327–352.
- Lyngtveit, T. J. (2017), Geochemical and microtextural characteristics reflect the formation mechanics of laminated iron deposits at the Perle & Bruse and Troll Wall vent fields, Master's thesis, University of Bergen.
- Macdonald, K. C., Becker, K. P., Spiess, F. N. and Ballard, R. D. (1980), 'Hydrothermal heat flux on the "black smoker" vents on the East Pacific Rise', *Earth and Planetary Science Letters* **48**(1), 1–7.
- MacLean, W. H. and Kranidiotis, P. (1987), 'Immobile elements as monitors of mass transfer in hydrothermal alteration; Phelps Dodge massive sulfide deposit, Matagami, Quebec', *Economic Geology* **82**, 951–962.
- McKerrow, W. S., Dewey, J. F. and Scotese, C. R. (1991), 'The Ordovician and Silurian development of the Iapetus ocean', *Special Papers in Paleontology* **44**, 165–178.
- McLennan, S. M. (1989), Rare earth elements in sedimentary rocks: influence of provenance and sedimentary processes, in B. R. Lipin and G. A. McKay, eds, 'Geochemistry and Mineralogy of Rare Earth Elements', Vol. 21, Reviews in Mineralogy, pp. 169–200.
- Michard, A., Michard, G., Stüben, D., Stoffers, P., Cheminée, J. L. and Binard, N. (1993), 'Submarine thermal springs associated with young volcanoes: the Teahitia vents, Society Islands, Pacific Ocean', *Geochimica et Cosmochimica Acta* **57**, 4977–4986.

- Murray, R. W. (1994), 'Chemical criteria to identify the depositional environment of chert: general principles and applications', *Sedimentary Geology* **90**, 213–232.
- Murray, R. W., Buchholtz Ten Brink, M. R., Gerlach, D. C., Price Russ III, G. and Jones, D. L. (1991), 'Rare earth, major, and trace elements in chert from the Franciscan Complex and Monterey Group, California: Assessing REE sources to fine-grained marine sediments', *Geochimica et Cosmochimica Acta* **55**, 1875–1895.
- Nordås, J., Amalixsen, K. G., Brekke, H., Suthren, R. J., Furnes, H., Sturt, B. A. and Robins, B. (1985), Lithostratigraphy and petrochemistry of Caledonian rocks on Bømlo, SW Norway, *in* D. G. Gee and B. A. Sturt, eds, 'The Caledonide Orogen - Scandinavia and Related Arcs', John Wiley & Sons Ltd, pp. 679–692.
- Norges Geologiske Undersøkelse (2017), 'Bedrock Map of Norway'.
URL: <http://geo.ngu.no/kart/berggrunn/> [Accessed: 16.11.17]
- Pedersen, R. B., Bruton, D. L. and Furnes, H. (1992), 'Ordovician faunas, island arcs, and ophiolites in the Scandinavian Caledonides', *Terra Nova* **4**(2), 217–222.
- Pedersen, R. B. and Dunning, G. R. (1997), 'Evolution of arc crust and relations between contrasting sources: U-Pb (age), Nd and Sr isotope systematics of the ophiolitic terrain of SW Norway', *Contributions to Mineralogy and Petrology* **128**(1), 1–15.
- Picard, A., Kappler, A., Schmid, G., Quaroni, L. and Obst, M. (2015), 'Experimental diagenesis of organo-mineral structures formed by microaerophilic Fe(II)-oxidising bacteria', *Nature Communications* **6**(6277).

- Rasmussen, B., Krapež, B. and Muhling, J. R. (2014), 'Hematite replacement of iron-bearing precursor sediments in the 3.46-b.y.-old Marble Bar Chert, Pilbara craton, Australia', *GSA Bulletin* **126**(9/10), 1245–1258.
- Roberts, D. (2003), 'The Scandinavian Caledonides: event chronology, paleogeographic settings and likely modern analogues', *Tectonophysics* **365**(1), 283–299.
- Roberts, D. and Gee, D. G. (1985), An introduction to the structure of the Scandinavian Caledonides, *in* D. G. Gee and B. A. Sturt, eds, 'The Caledonide Orogen - Scandinavia and Related Arcs', John Wiley & Sons Ltd, pp. 55–68.
- Roberts, D., Sturt, B. A. and Furnes, H. (1985), Volcanite assemblages and environments in the Scandinavian Caledonides and the sequential development history of the mountain belt, *in* D. G. Gee and B. A. Sturt, eds, 'The Caledonide Orogen - Scandinavia and Related Arcs', John Wiley & Sons Ltd, pp. 919–930.
- Rollinson, H. R. (1993), *Using geochemical data: evaluation, presentation, interpretation*, Harlow, Essex, England: Longman Scientific & Technical.
- Sato, T. (1972), 'Behaviours of Ore-forming Solutions in Seawater', *Mining Geology* **22**, 31–42.
- Schwertmann, U. and Fitzpatrick, R. W. (1992), Iron minerals in surface environments, *in* H. C. W. Skinner and R. W. Fitzpatrick, eds, 'Biomineralization. Process of iron and manganese', Catena Verlag, Germany, pp. 7–30.
- Scotese, C. R. and McKerrow, W. S. (1991), Ordovician plate tectonic reconstructions, *in* C. R. Barnes and S. H. Williams, eds, 'Advances in Ordovi-

- cian Geology', Vol. 90-9, Fifth International Symposium on the Ordovician, Geological Survey of Canada, pp. 271–282.
- Sherrell, R. M., Field, M. P. and Ravizza, G. (1999), 'Uptake and fractionation of rare earth elements on hydrothermal plume particles at 9°45'N, East Pacific Rise', *Geochimica et Cosmochimica Acta* **63**, 1709–1722.
- Shimizu, H., Kunimaru, T., Yoneda, S. and Adachi, M. (2001), 'Sources and Depositional Environments of Some Permian and Triassic Cherts: Significance of Rb-Sr and Sm-Nd Isotopic and REE Abundance Data', *The Journal of Geology* **109**, 105–125.
- Singer, E., Emerson, D., Webb, E. A., Barco, R. A., Kuenen, J. G., Nelson, W. C., Chan, C. S., Comolli, L. R., Ferriera, S., Johnson, J., Heidelberg, J. F. and Edwards, K. J. (2011), '*Mariprofundus ferrooxydans* PV-1 the First Genome of a Marine Fe(II) Oxidizing *Zetaproteobacterium*', *PLOS ONE* **6**(9), e25386.
- Sivertsen, J. E. (1992), 'Stratigraphy and geochemistry of the extrusives of the Torvastad Group; marginal basin deposits associated with the Karmøy Ophiolite Complex, SW Norway', Cand.Scient.Thesis, University of Bergen.
- Slack, J. F., Grenne, T., Bekker, A., Rouxel, O. J. and Lindberg, P. A. (2007), 'Suboxic deep seawater in the late Paleoproterozoic: Evidence from hematitic chert and iron formation related to seafloor-hydrothermal sulfide deposits, central Arizona, USA', *Earth and Planetary Science Letters* **255**, 243–256.
- Smalley, I. J. (1963), 'Radiolarians: Construction of Spherical Skeleton', *Science* **140**(3565), 396–397.

- Søgaard, E. G., Medenwaldt, R. and Abraham-Peskir, J. V. (2000), 'Conditions and rates of biotic and abiotic iron precipitation in selected Danish freshwater plants and microscopic analysis of precipitate morphology', *Water Research* **34**, 2765–2682.
- Spiess, F. N., Macdonald, K. C., Atwater, T., Ballard, R. D., Carranza, A., Cordoba, D., Cox, C., Garcia, V. M., Francheteau, J., Guerrero, J., Hawkins, J., Haymon, R., Hessler, R., Juteau, T., Kastner, M., Larson, R., Luyendyk, B., Macdougall, J. D., Miller, S., Normark, W., Orcutt, J. and Rangin, C. (1980), 'East Pacific Rise: Hot springs and geophysical experiments', *Science* **207**, 1421–1433.
- Stephens, M. B. and Gee, D. G. (1985), A tectonic model for the evolution of the eugeoclinal terranes in the central Scandinavian Caledonides, *in* D. G. Gee and B. A. Sturt, eds, 'The Caledonide Orogen - Scandinavia and Related Arcs', John Wiley & Sons Ltd, pp. 953–978.
- Stephens, M. B. and Gee, D. G. (1989), Terranes and polyphase accretionary history in the Scandinavian Caledonides, *in* R. D. Dallmeyer, ed., 'Terranes in the Circum-Atlantic Paleozoic Orogens', Vol. 230, Geological Society of America, pp. 17–30.
- Stubseid, H. H. (2017), Geological evolution and stratigraphic relationships of the ophiolitic terrane in the outer Hardangerfjord area: evidence from geochronology and geochemistry, Master's thesis, University of Bergen.
- Sugisaki, R., Yamamoto, K. and Adachi, M. (1982), 'Triassic bedded cherts in central Japan are not pelagic', *Nature* **298**, 644–647.
- Sun, Z., Li, J., Huang, W., Dong, H., Little, C. T. S. and Li, J. (2015), 'Generation of hydrothermal Fe-Si oxyhydroxide deposit on the Southwest

- Indian Ridge and its implications for the origin of ancient banded iron formations', *Journal of Geophysical Research* **120**(1), 187–203.
- Sun, Z., Zhou, H., Glasby, G. P., Yang, Q., Yin, X., Li, J. and Chen, Z. (2012), 'Formation of Fe-Mn-Si oxide and nontronite deposits in hydrothermal fields on the Valu Fa Ridge, Lau Basin', *Journal of Asian Earth Sciences* **43**(1), 64–76.
- Sverjensky, D. A. (1984), 'Europium redox equilibria in aqueous solution', *Earth and Planetary Science Letters* **67**, 70–78.
- Sylvan, J. B., Pyenson, B. C., Rouxel, O. J., German, C. R. and Edwards, K. J. (2012), 'Time-series analysis of two hydrothermal plumes at 9°50'N East Pacific Rise reveals distinct, heterogeneous bacterial populations', *Geobiology* **10**, 178–192.
- Taylor, S. R. and McLennan, S. M. (1985), *The Continental Crust: Its Composition and Evolution*, Blackwell Scientific Publications, Oxford.
- Tivey, M. K. (2007), 'Generation of Seafloor Hydrothermal Vent fluids and Associated Mineral Deposits', *Oceanography* **20**(1), 50–65.
- Törnebohm, A. E. (1888), 'Om fjällproblemet', *Geologiska Föreningen i Stockholm Förhandlingar* **10**, 328–336.
- Toth, J. R. (1980), 'Deposition of submarine crusts rich in manganese and iron', *Geological Society of America Bulletin* **91**, 44–54.
- Udchachon, M., Thassanapak, H., Feng, Q. and Chonglakmani, C. (2011), 'Geochemical constraints on the depositional environment of Upper Devonian radiolarian cherts from Loei, north-eastern Thailand', *Frontiers of Earth Science* **5**(2), 178–190.

- Viken, A. L. (2017), Accretionary history of Lower Ordovician island arc complexes on Bømlo: evidence from detrital zircon dating and geochemical data, Master's thesis, University of Bergen.
- Wallmann, K. and Aloisi, G. (2012), The Global Carbon Cycle: Geological Processes, *in* A. H. Knoll, D. E. Canfield and K. O. Konhauser, eds, 'Fundamentals of Geobiology', Blackwell Publishing Ltd, chapter 3, pp. 20–35.
- Weiss, R. F., Lonsdale, P., Lupton, J. E., Brainbridge, A. E. and Craig, H. (1977), 'Hydrothermal plumes in the Galapagos rift', *Nature* **267**, 600–603.
- Wilde, P., Quinby-Hunt, M. S. and Erdtmann, B.-D. (1996), 'The whole-rock cerium anomaly: a potential indicator of eustatic sea-level changes in shales of the anoxic facies', *Sedimentary Geology* **101**, 43–53.
- Wolery, T. J. and Sleep, N. H. (1976), 'Hydrothermal circulation and geochemical flux at mid-ocean ridges', *Journal of Geology* **84**, 249–275.
- Wood, S. A. (1990), 'The aqueous geochemistry of the rare-earth elements and yttrium: 2. Theoretical predictions of speciation in hydrothermal solutions to 350 °C at saturation water vapour pressure', *Chemical Geology* **88**, 99–125.
- Yamamoto, K. (1983), 'Geochemical study of Triassic bedded cherts from Kamiaso, Gifu Prefecture', *The Journal of the Geological Society of Japan* **89**, 143–162.
- Yamamoto, K. (1987), 'Geochemical characteristics and depositional environments of cherts and associated rocks in the Franciscan and Shimanto Terranes', *Sedimentary Geology* **52**, 65–108.
- Zagorevski, A., Rogers, N., van Staal, C. R., McNicoli, V., Lissenberg, C. J. and Valverde-Vaquero, P. (2006), 'Lower to Middle Ordovician evolution

of peri-Laurentian arc and backarc complexes in Iapetus: Constraints from the Annieopsquotch accretionary tract, central Newfoundland', *GSA Bulletin* **118**(3-4), 324-342.

Appendices

Appendix A

GPS coordinates for sampling locations

Table A.1: GPS coordinates for sampling locations

Location	Sample ID	Rock type	GPS coordinates
1: Langevåg, Bømlo	B-L-1	Bedded radiolarian chert	59°36'26.9"N 5°13'28.7"E
1: Langevåg, Bømlo	B-L-2	Bedded radiolarian chert	59°36'27.1"N 5°13'29.2"E
1: Langevåg, Bømlo	B-L-3	Bedded radiolarian chert	59°36'26.6"N 5°13'27.8"E
2: Geitung, Bømlo	B-G-1	Hematitic chert band in metasandstone	59°41'35.7"N 5°07'29.9"E
2: Geitung, Bømlo	B-G-2	Jasper clast in volcanic breccia	59°41'35.2"N 5°07'31.3"E
2: Geitung, Bømlo	B-G-3a	Jasper clast in volcanic breccia	59°41'35.2"N 5°07'31.5"E
2: Geitung, Bømlo	B-G-3b	Jasper clast in volcanic breccia	59°41'35.2"N 5°07'31.5"E
2: Geitung, Bømlo	B-G-4	Jasper clast in volcanic breccia	59°41'35.1"N 5°07'31.6"E
3: Finnås, Bømlo	B-F-1	Jasper clast within basal conglomerate	59°44'34.7"N 5°15'26.2"E
4: Sagvåg gruve, Stord	S-S-G	Hematitic chert	59°47'19.5"N 5°25'05.5"E
5: Sagvåg coast, Stord	S-S-S	Hematitic chert	59°45'57.4"N 5°23'20.1"E

Appendix B

Additional sampling location photographs



Figure B.1: Location 1: Langevåg, Overview of the outcrop for B-L-1 to B-L-3



Figure B.2: Location 1: Langevåg, Close-up of bedded radiolarian chert, B-L-3



Figure B.3: Location 2: Geitung, Close-up of hematitic radiolarian chert band, B-G-1



Figure B.4: Location 2: Geitung, Jasper clast, B-G-4



Figure B.5: Location 5: Sagvåg, on the coast of Stord, hematitic chert, S-S-S, photo courtesy of Ingunn H. Thorseth

Appendix C

Overview of samples and analytical methods

Table C.1: Sample list and used analytical methods

Sample ID	Thin section	Amount milled	ICP-OES & ICP-MS
B-L-1	✓	2.5 g	✓
B-L-2	✓	3.9 g	✓
B-L-3	✓	3.0 g	✓
B-G-1	✓	2.2 g	✓
B-G-2	No*	-	No*
B-G-3a	✓	1.8 g	✓
B-G-3b	✓	1.1 g	✓
B-G-4	✓	1.2 g	✓
B-F-1	✓	1.8 g	✓
S-S-G	✓	-	No*
S-S-S	✓	3.5 g	✓

* Omitted from analysis

Appendix D

Correlations of major and trace elements

Groups A and B

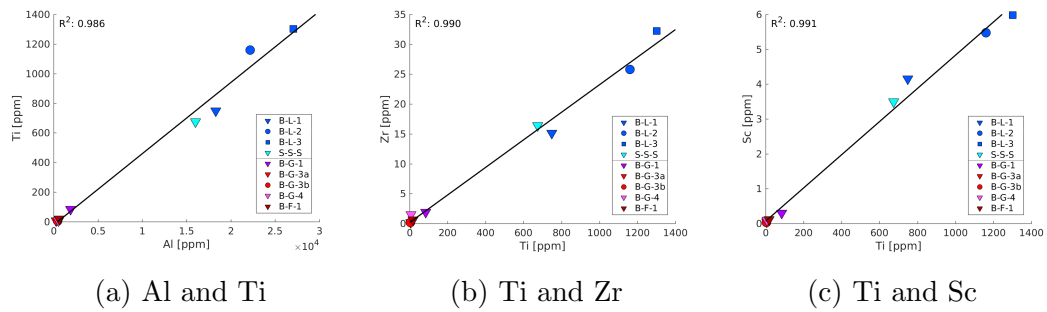


Figure D.1: Correlations between various major and trace elements, Groups A and B

Appendix E

Correlation tables of REE patterns between samples

Table E.1: Correlations of REE patterns between samples, Chondrite normalisation

Sample ID	B-L-1	B-L-2	B-L-3	S-S-S	B-G-1	B-G-3a	B-G-3b	B-G-4	B-F-1
B-L-1	1								
B-L-2	0.999 68	1							
B-L-3	0.999 96	0.999 61	1						
S-S-S	0.999 17	0.998 29	0.998 93	1					
B-G-1	0.989 84	0.991 68	0.989 97	0.9841	1				
B-G-3a	0.643 03	0.649 63	0.6415	0.6443	0.9841	1			
B-G-3b	0.911 71	0.906 02	0.912 22	0.909 24	0.9841	0.6443	1		
B-G-4	-0.281 22	-0.266 75	-0.283 67	-0.278 22	-0.291 58	0.452 29	-0.452 78	1	
B-F-1	0.779 35	0.793 55	0.778 91	0.763 64	0.820 86	0.748 39	0.600 46	0.193 79	1

Table E.2: Correlations of REE patterns between samples, NASC normalisation

Sample ID	B-L-1	B-L-2	B-L-3	S-S-S	B-G-1	B-G-3a	B-G-3b	B-G-4	B-F-1
B-L-1	1								
B-L-2	0.952 62	1							
B-L-3	0.9589	0.875 11	1						
S-S-S	0.943 38	0.956 59	0.830 32	1					
B-G-1	-0.612 47	-0.498 58	-0.794 82	-0.419 76	1				
B-G-3a	-0.8044	-0.636 94	-0.849 52	-0.662 31	0.684 55	1			
B-G-3b	0.092 41	0.008 75	0.026 05	0.101 03	0.283 82	-0.042 64	1		
B-G-4	-0.808 98	-0.627 77	-0.842 64	-0.668 59	0.623 81	0.9845	-0.206 76	1	
B-F-1	-0.882 18	-0.730 33	-0.936 48	-0.735 63	0.747 75	0.942 72	-0.193 43	0.955 66	1

Table E.3: Correlations of REE patterns between samples, PAAS normalisation

Sample ID	B-L-1	B-L-2	B-L-3	S-S-S	B-G-1	B-G-3a	B-G-3b	B-G-4	B-F-1
B-L-1	1								
B-L-2	0.933 81	1							
B-L-3	0.704 47	0.416 19	1						
S-S-S	0.9628	0.980 95	0.513 09	1					
B-G-1	0.611 63	0.838 83	-0.116 09	0.761 92	1				
B-G-3a	0.064 36	0.395 59	-0.5708	0.258 39	0.719 08	1			
B-G-3b	0.702 42	0.694 85	0.430 98	0.688 61	0.565 77	0.186 38	1		
B-G-4	-0.088 21	0.2543	-0.686 16	0.116 42	0.620 54	0.980 01	-0.004 28	1	
B-F-1	0.087 76	0.423 44	-0.611 39	0.294 72	0.782 34	0.950 34	0.100 42	0.947 49	1

Appendix F

Element and oxide ratios

Table F.1: Element and oxide ratios

Sample ID	Co/Zn	Al/(Al+Fe+Mn)	Mn/Fe	MnO/TiO ₂
B-L-1	0.33	0.55	0.082	1.15
B-L-2	0.38	0.55	0.054	0.63
B-L-3	0.44	0.56	0.039	0.47
S-S-S	0.35	0.56	0.061	0.84
B-G-1	0.12	0.13	0.088	9.85
B-G-3a	0.07	0.01	0.005	21.15
B-G-3b	0.04	0.02	0.003	11.05
B-G-4	0.09	0.01	0.001	14.05
B-F-1	0.27	0.01	0.001	1.72